Solar Panel Effect on Low-Speed Airfoil Aerodynamic Performance

Mostafa El-Salamony (elsalamony.mostafa@pku.edu.cn)
Peking University
Mohamed Aziz
Suez University

Research

Keywords: solar panel, airfoil, UAV, AG 34, aerodynamic performance

Posted Date: April 21st, 2020

DOI: https://doi.org/10.21203/rs.3.rs-21225/v1

Version of Record: A version of this preprint was published at Unmanned Systems on March 4th, 2021.
See the published version at https://doi.org/10.1142/S2301385021500175.

Solar Panel Effect on Low-Speed Airfoil Aerodynamic Performance

Mostafa E. El-Salamony [a], Mohamed A. Aziz [b]

[a] *College of Engineering, Peking University Beijing, China*
E-mail: elsalamony.mostafa@pku.edu.cn

[b] *College of Engineering, Suez University, Suez, Egypt*
E-mail: mohamed.aziz@suezuni.edu.eg

Although the solar panel is thin, its thickness is considerable compared to the airfoil thickness. This paper aims to evaluate the impact of adding the solar panel over an airfoil of a UAV of type AG 34, which is low camber airfoil suitable for low-Reynolds number flights. Three configurations are examined to stand on the most suitable configuration. The analysis is based on the airfoil characteristics (lift, drag, and moment) and the pressure distribution over the airfoil surface. A parametric study is conducted to study the effect of the solar panel size and position on the aerodynamic performance.

1. Introduction

Because of the limited capacity of fuel tanks, Extreme endurance of months is impossible without aerial refueling. On the other hand, a solar powered aircraft van be capable of flying for several weeks or month. If an aircraft is able to store enough solar energy during the daytime, this stored energy can be used to sustain flying at night. Then the cycle will be repeated on the following day. Theoretically speaking, such an aircraft will not need to land as long as it collects enough solar energy daily for the night flight. Only a limited number of aircraft have demonstrated the ability of continuous (perpetual) flight and most of these flights only occurred in the recent years. Continuous flight is most feasible during summer season, as the day hours are more than the night hours [1]. These aircraft use to fly slowly to reduce power consumption, but too slow that a strong headwind could prevent them from flying ahead. [2, 3]

First SPUAV was Sunrise I which was created by Robert Boucher and Roland Boucher in 1974 [4, 5] then this research trend began to flourish and many remarkable aircraft are designed and manufactured as Solong [6], Helios [7], Photon [8], the AtlantikSolar, and Solar Impulse [9].

Research in this field opened several applications [10], as investigation to increase the efficiency of SPUAVs as, optimal flight path planning and control [11, 12], trajectory control for maximum power accumulation [13], optimizing cruise speed and sizing [14], power optimization [15], weight estimation [16], optimal turning planning to increase flight endurance of solar powered UAVs [18], maximizing net power in circular turns [19]. Also wing morphing technique has a promising potential in this field [20 - 22].

Since the solar panels are to be mounted over the wing, the airfoil shape will be deformed. This deformation eventually leads to variation in lift and drag. since the panel thickness is small compared to the airfoil boundary layer, the laminar turbulent transition is not likely to happen or has a limited effect [22]. On the other hand, the panel contributes in deforming the streamlines over the airfoil and can change its performance. Thus, this work aims to investigate the change in the airfoil behavior due to installing the solar panels over the wing, by quantifying the lift, drag, and moment coefficients for several possible configurations. Pressure and velocity contours are also used to have better insight on the flow behavior. Then, a parametric study is conducted to investigate the importance of three main parameters, namely solar panel position, size, and thickness.

In Section 2 the different airfoil geometries and the numerical setup are discussed. The aerodynamic study of the different configurations presented, followed by three parametric studies of the solar panel position, size, and thickness in Section 4, and the results are concluded in Section 5.

2. Geometry and Numerical Setup

2.1 Studied Airfoils

Despite the fact that high camber airfoils act fine at the cruise condition, the drag would increase quickly in case that the aircraft is deviated from the design condition. The high camber airfoil design would make perpetual solar endurance flight more difficult to achieve since the drag penalties from inevitable cruise speed deviations would more than offset slightly better cruise drag. Besides, high camber airfoil would increase the airfoil pitching moment, which would require a heavier wing structure to prevent the wing from twisting. The tail load to trim the airplane would also increase, which would add drag. Hence, low camber airfoil is used, and the airfoil AG34 is decided for this investigation because it is [22]:

1. tolerate different boundary layer transition locations without a large increase in drag
2. more tolerant of cruise speed deviations and made it easier to penetrate headwinds
3. has a low pitching moment, which allowed the wing structure to be lighter and reduced the size of the horizontal stabilizer

In this study, three different shapes are studied and compared with the clear airfoil case, as shown in Figure 1.

1. The solar panel is mounted on the airfoil, and has the same curvature (Curved Over).
2. The panel is mounted on the wing, but straight not curved (Flat Over).
3. The panel is straight also, but submerged in the airfoil, as of the airfoil is cut (Flat Submerged).

The solar panel, used in the cases blow, has length of 17.5 cm, corresponding to 50% of the airfoil chord, and located in the middle of the airfoil, i.e., the leading edge of the panel is at 25% of the chord. In Section 4 the panel position, length, and thickness are changed.

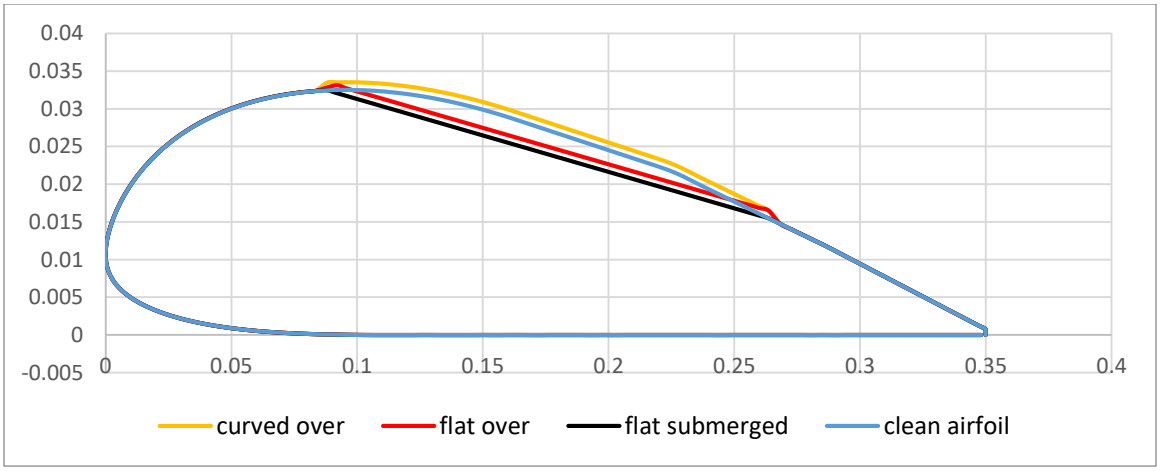

Figure 1 Studied Airfoil Configurations.

2.2 Mesh Dependency and Consistency

Different meshes are studied to stand on the mesh dependency of the solution. The domain is designed as O-shaped with diameter of 7 m, which corresponds to 10 chord lengths, and domain thickness of 0.001 m. Inlet velocity is 10.5 m/s, angle of attack is 5o, and air density is 1.225 kg/m3. Exit boundary condition is set as Open. no-slip boundary condition is used for the wing surface. Shear Stress Transport (SST) turbulence model is used for turbulence closure problem. This model is selected because it is robust enough to handle attached and separated flows with Y+ up to 10 [24]. The meshes are listed in Table 1 and the drag coefficient is shown in Figure 2.

Table 1 investigated meshes

Case	*Mesh Nodes*	*Mesh Elements*	*Drag*	*Y+*	*Mass Flow Error*
1	9709	22082	0.0444	6.389	-5.96E-08
2	18503	41307	0.0389	7.548	-1.19E-07
3	29339	64236	0.0324	8.021	<1E-8
4	61567	176682	0.0304	7.962	<1E-8
5	80989	212150	0.027	8.763	5.96E-08

One notices that increasing the mesh nodes from 6×104 to 8×104 nodes leads to decrease in the drag value by 0.003. Besides, the change in lift coefficient is 3.7% compared to the finest mesh. This minor change can be neglected to save computational power. Hence, the selected mesh is the mesh number 4 (Fig. 3).

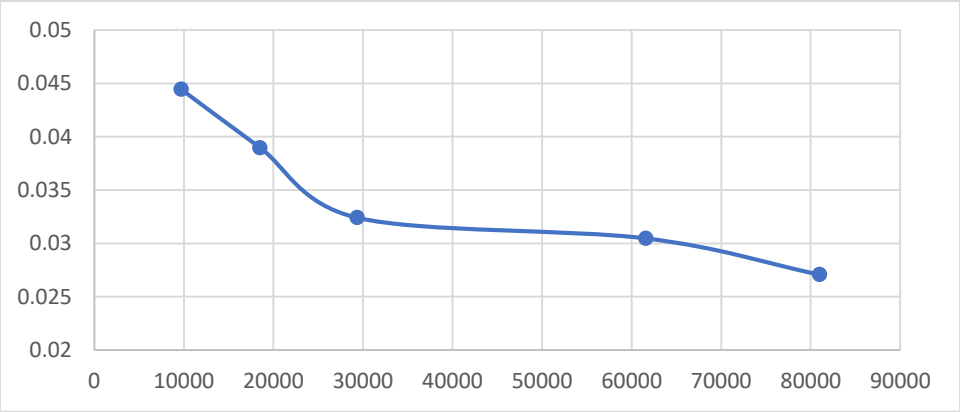

Figure 2 the drag coefficient variation with mesh nodes

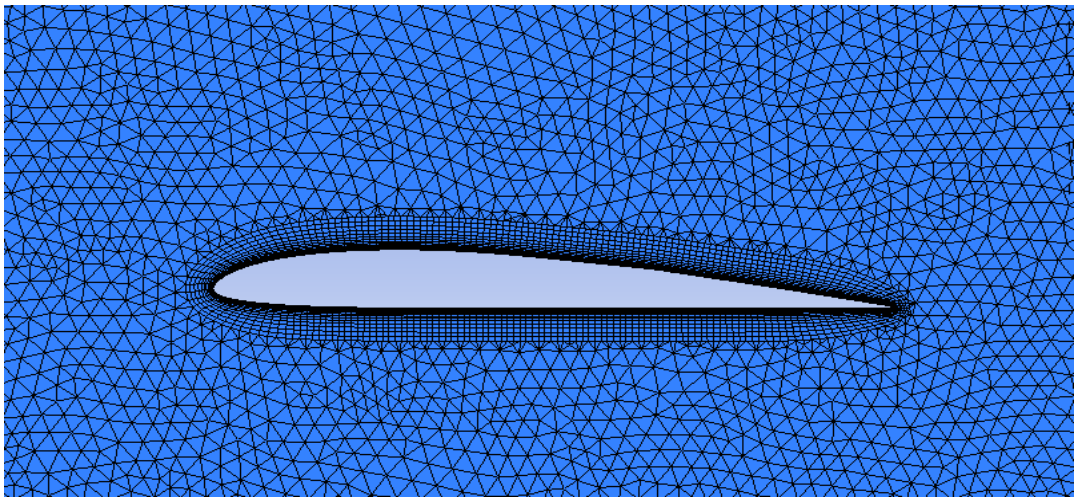

Figure 3 the two-dimensional mesh around the studied airfoil

Of interest, lift, drag, and moment coefficients of the airfoil are illustrated in Figures 4-6. The aerodynamic coefficients follow the standard definitions in the literature (see e.g. [25]), except for the moment coefficient where the moments are taken around the airfoil leading edge.

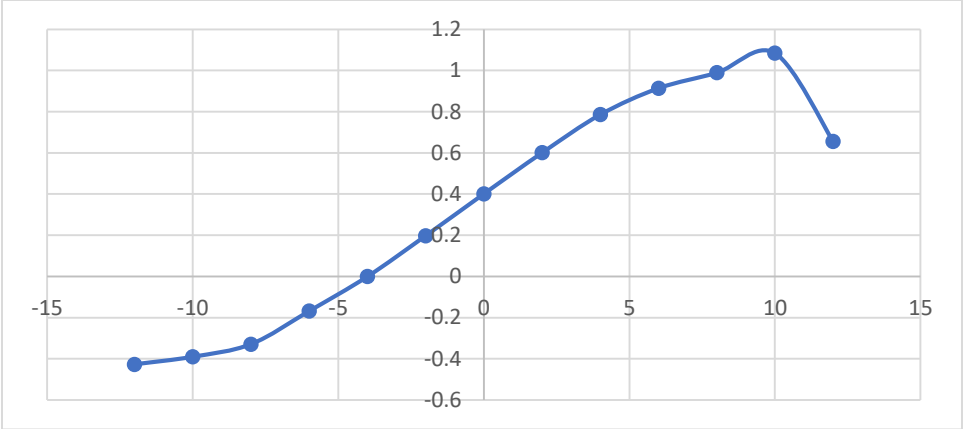

Figure 4 lift coefficient variations with angle of attack

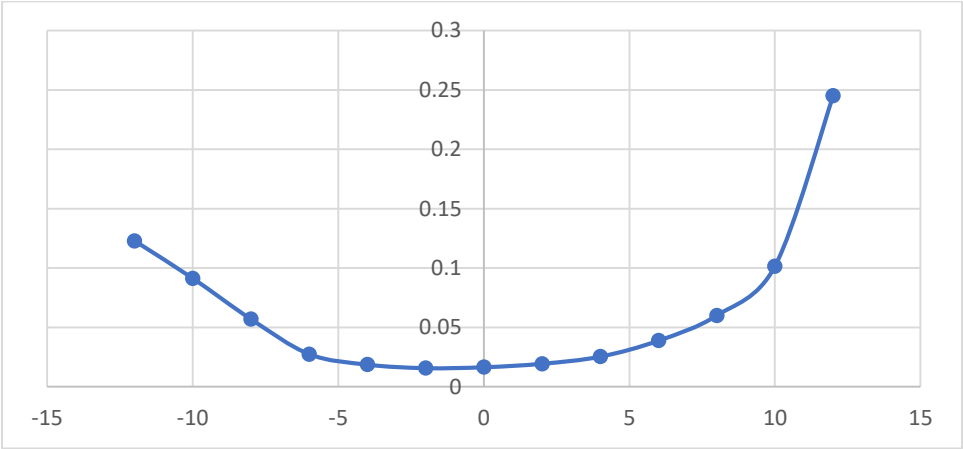

Figure 5 Drag coefficient variations with angle of attack

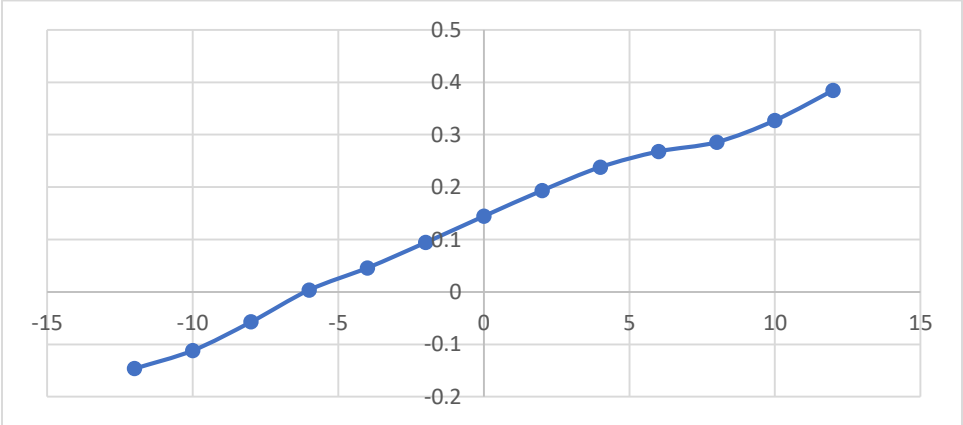

Figure 6 moment coefficient variations with angle of attack

2.3 Validation

Considering validation of the results, unfortunately there are no published experiments on this airfoil, up to the knowledge of the authors. Hence, Cross-validation with another software is used. The aforementioned 2D simulations are used to cross-validate with another code. XFLR5 [26] is used, which is based on Vortex Lattice Method [27]. This step was done to ensure that the basic step (airfoil analysis) is acceptable, to prevent the possible mistakes later.

Lift and drag coefficients of the airfoil are illustrated in Figures 7 and 8. It is notable that XFLR5 overestimate the lift, the drag is underestimated with small deviation in the trend, because of this method is not adequate for the friction drag. As for moment coefficient (Fig. 9), there is a notable difference because of the difference in the moment center.

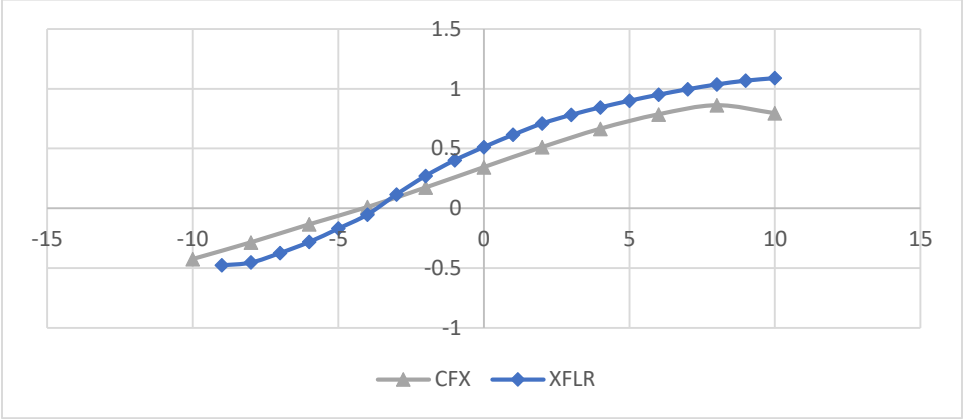

Figure 7 Lift coefficient variations with angle of attack for CFD and XFLR

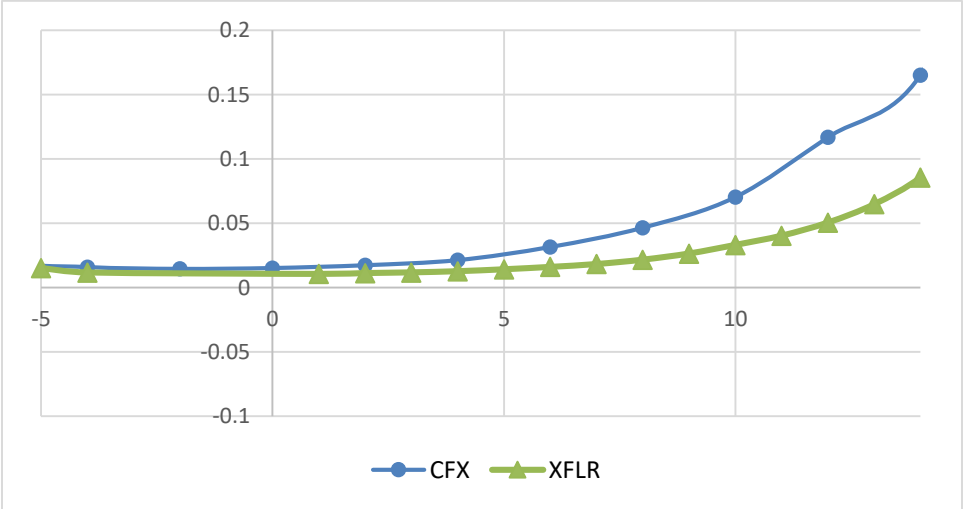

Figure 8 Drag coefficient variations with angle of attack for CFD and XFLR

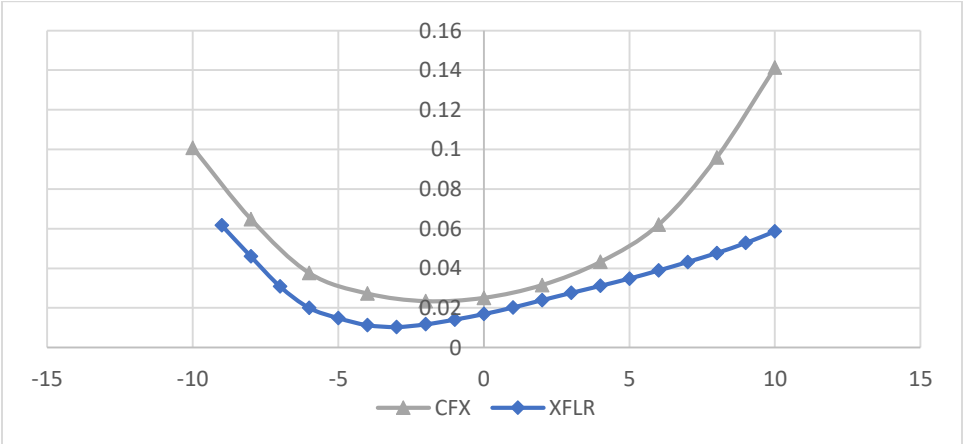

Figure 9 Moment coefficient variations with angle of attack for CFD and XFLR

3. Results and Discussion

3.1 Aerodynamic Performance

By studying the velocity contours (Figure 10 a-d) around the different configurations, one can notice that, for the 'solar over' case, the leading edge velocity is slightly less, compared to the 'clean' case. As for the 'flat over' case, the air is noticeably slower over the panel, and this effect extends downstream, leading to faster separation at the trailing edge. The same pattern exists in the 'flat submerged' case, but less severe near the trailing edge because of the absence of the 'step' of the panel.

As for the pressure contours (Figure 11 a-d), the 'solar over' case has more negative pressure zone at the leading edge for the 'solar over' case. Also, a local small negative pressure zone exists at the start of the solar step. Considering the 'flat over' case, the negative pressure zone starting at the LE is bigger and merged with the negative pressure zone at the panel start; it decreases then increases again in the vicinity of the deformed position, which may help in stabilizing the flow at higher angles of attack. The 'flat submerged' case shows similar behavior except for negative pressure zone in the airfoil beginning, where the negative pressure zone is more obvious and extends to the panel staring location. This 'extended leading edge suction' seems to enhance the airfoil performance at stall conditions, but the separation near the trailing edge worsen the stall performance. Yet, from drag coefficient as shown below, it seems that the separation is enhanced. This observation and trade-off need to be studied through unsteady simulation, because of the physics of the stall problem.

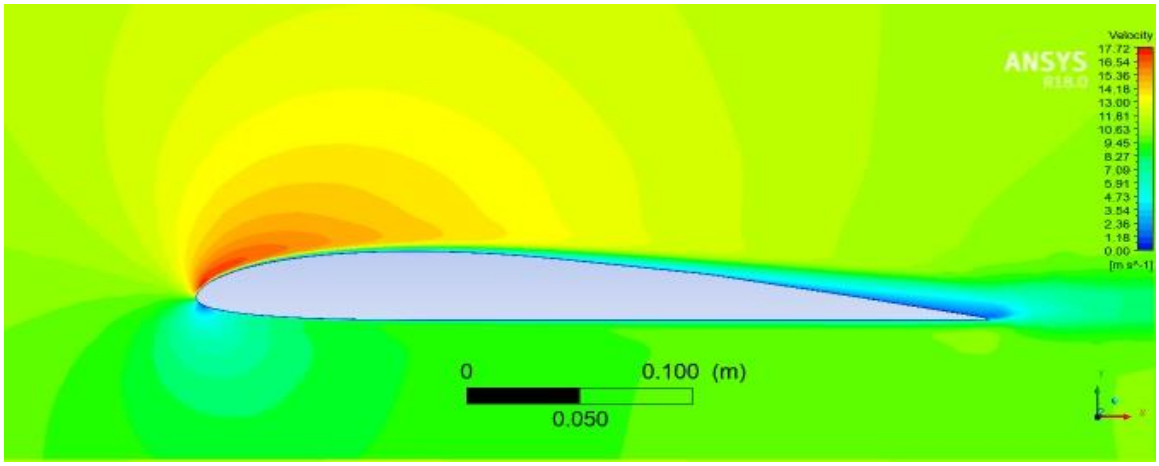

(a)

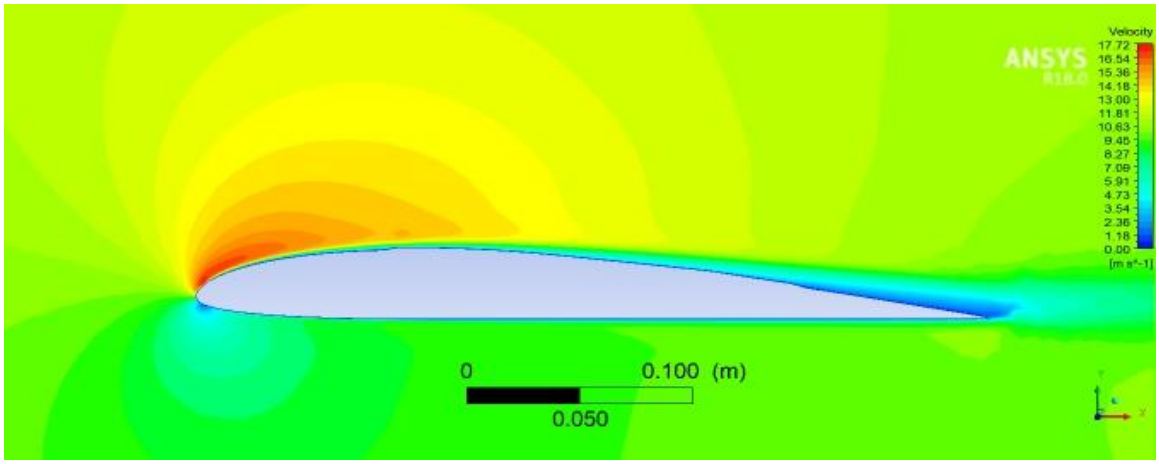

(b)

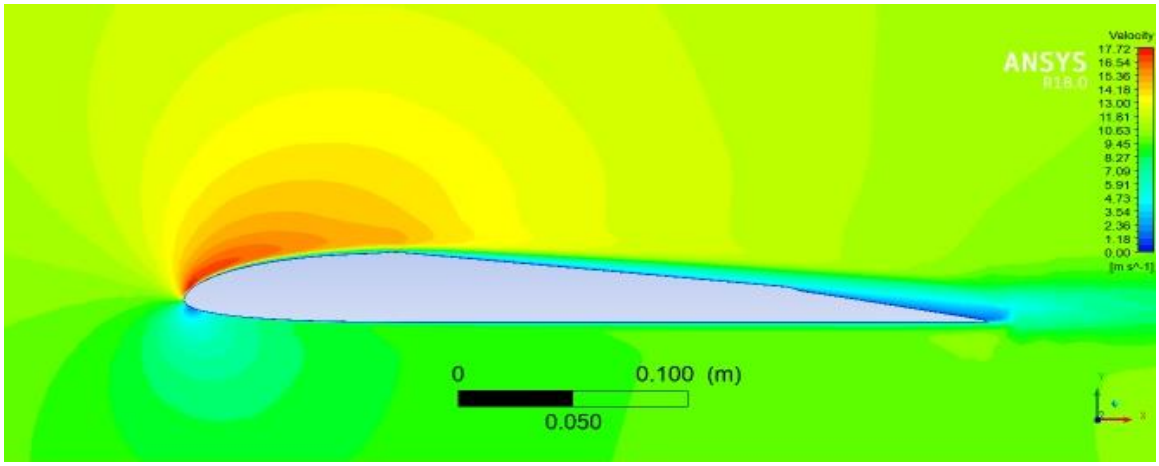

(c)

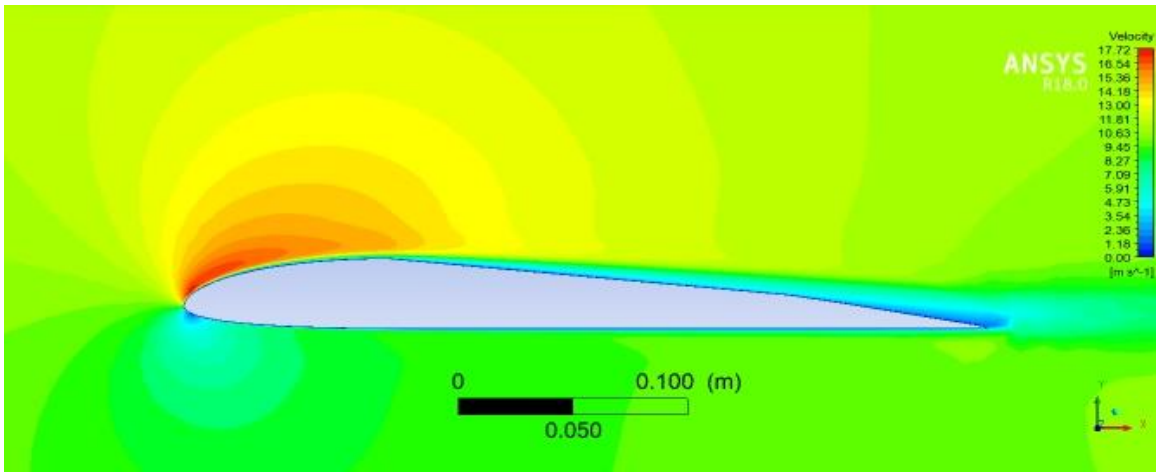

(d)

Figure 10 Velocity contour around airfoil AG34 at 6o angle of attack for the configurations a) clean airfoil, b) over curved, c) over flat, and d) submerged flat

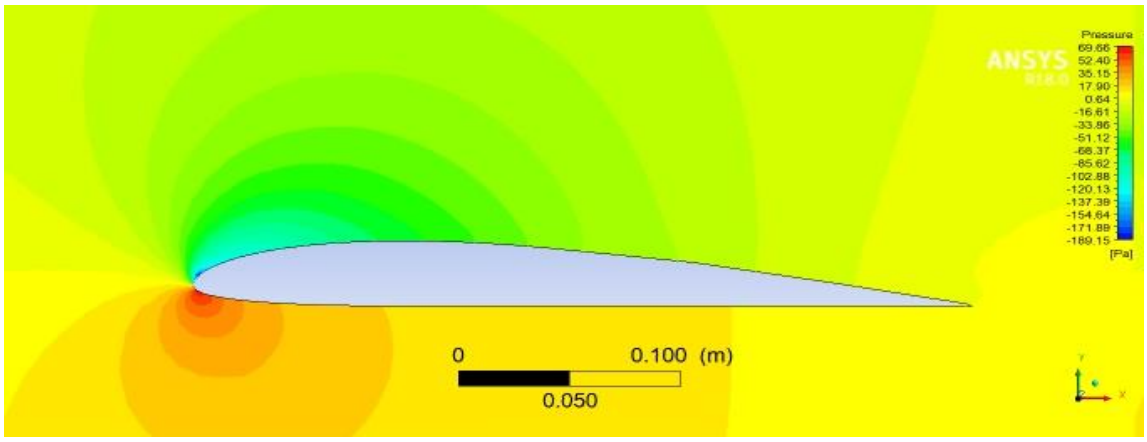

(a)

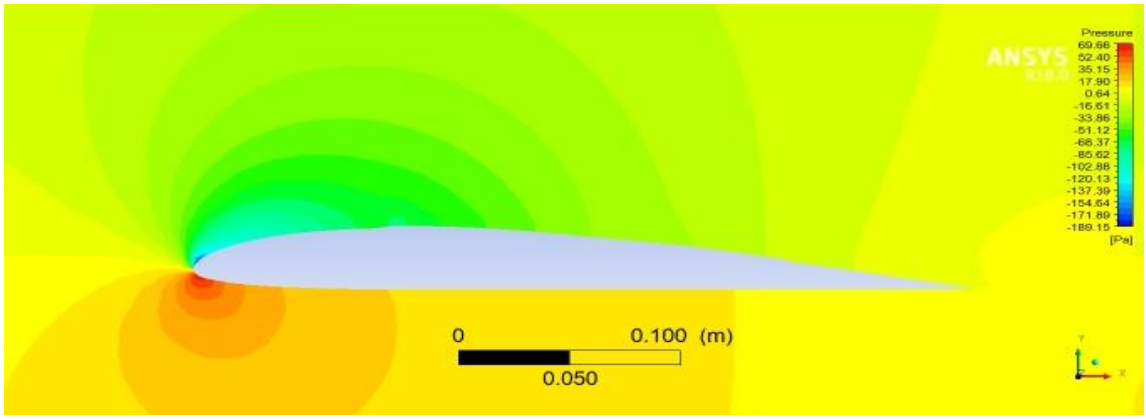

(b)

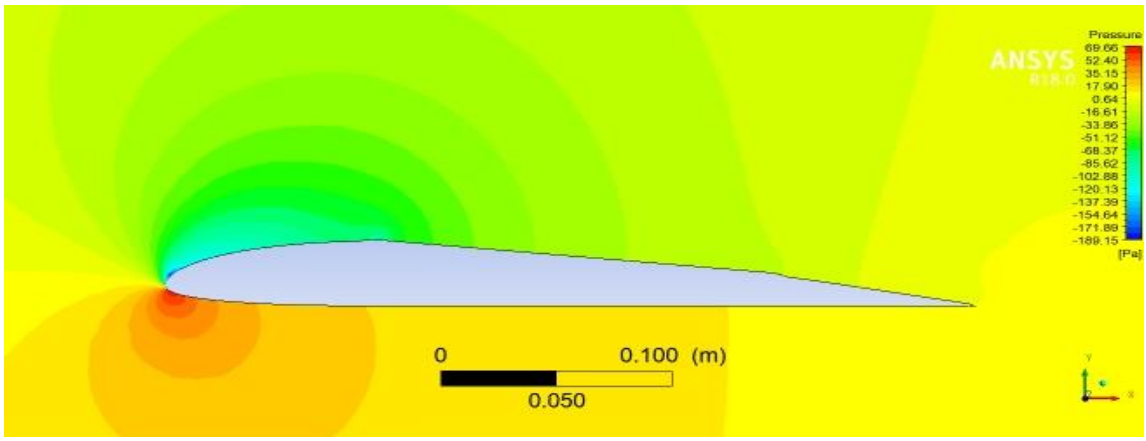

(c)

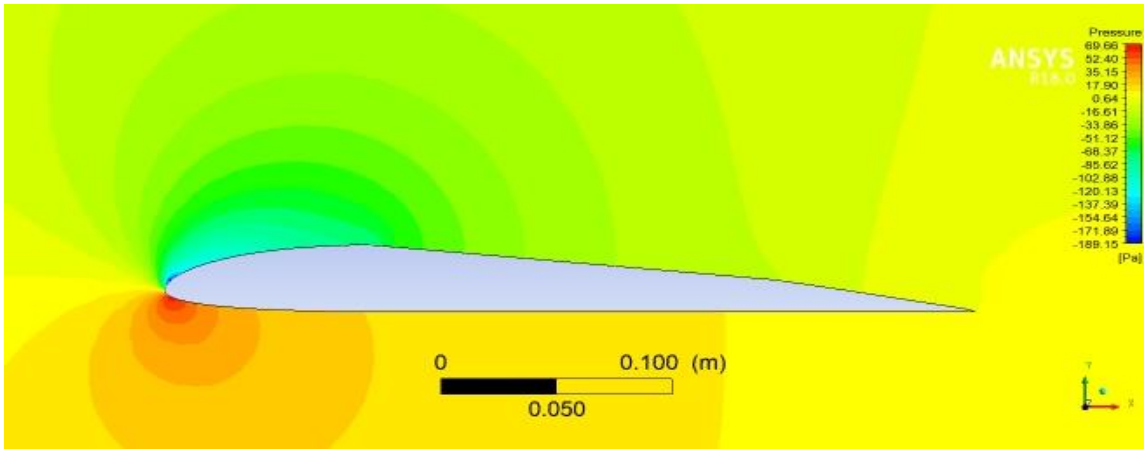

(d)

Figure 11 Pressure contour around airfoil AG34 at 6o angle of attack for the configurations a) clean airfoil, b) over curved, c) over flat, and d) submerged flat

The pressure distribution over the different configurations is shown in Figure 12, the Cp over the lower airfoil surface is the same for all cases, while over the upper surface Cp can be divided into 3 regions. Before the step the pressure increases gradually for both 'flat' cases, while in case of 'solar over' the pressure decreases

first then increases sharply at the panel start position. Over the panel, Cp decreases below the 'clean' case, while the 'solar over' case is quickly restored to match the 'clean' case. After the panel all cases start to match again with the 'clean' case.

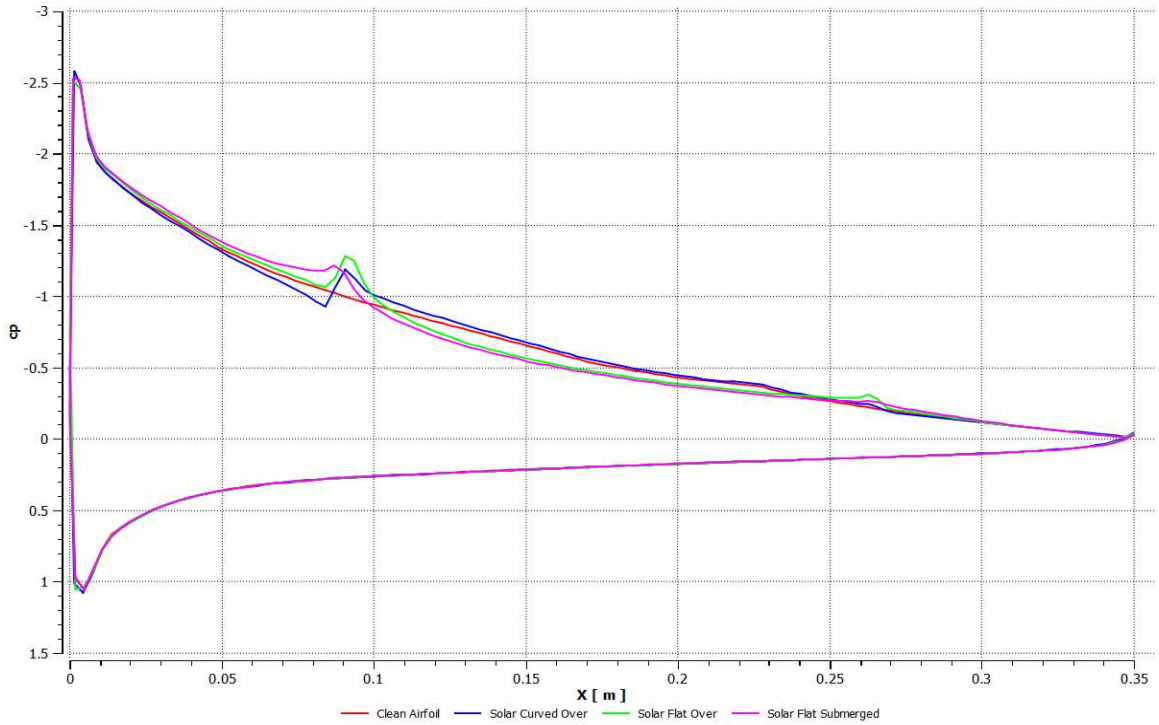

Figure 12 Pressure coefficient distribution over the different airfoil configurations

Airfoil performance coefficients are shown in Figures 13 to 15. It is shown that all cases have almost the same CL values, except that the 'solar over' case has slightly higher lift, while the '' case has slightly less CL. Hence, it has a worse stall performance.

In CD, all cases have almost the same drag, but in 'flat submerged' case has slightly less drag, while the 'solar over' has slightly higher. For 6o angle of attack, the drag is studied with some detail in Subsection 3.1. As for moment coefficients, 'solar over' case has the highest CM, while the 'flat submerged' case has the minimum.

Since CL and CD are almost the same, now we study CL/CD and $CL^{1.5}/CD$ because they provide better insight, are more useful in calculating the total aircraft performance parameters [28], and can be used in further analysis conducted by actual flight tests. For both parameters, 'solar over' case has the highest values, and the 'flat over' case has the minimum values over the whole applicable range, because its higher CD values, compared to 'flat submerged' case.

It shall be noted that the data within the range of [-10°, 8°][1] is much more reliable compared to the data out of that range, because of the unsteady separation and stall behaviors comes into action.

1 The airfoil has incident angle of approximately 1.5-2o.

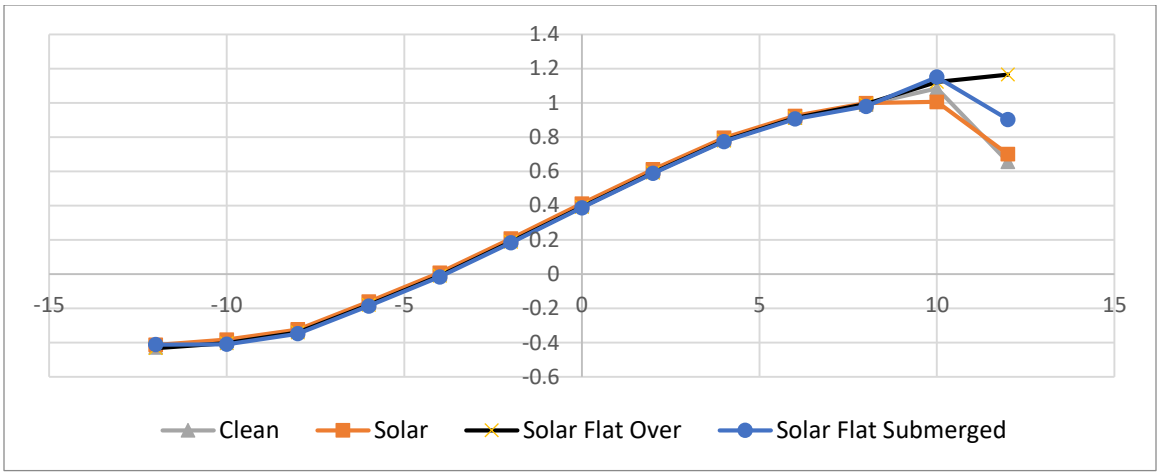

Figure 13 Lift coefficient VS. angle of attack for the different airfoil configurations

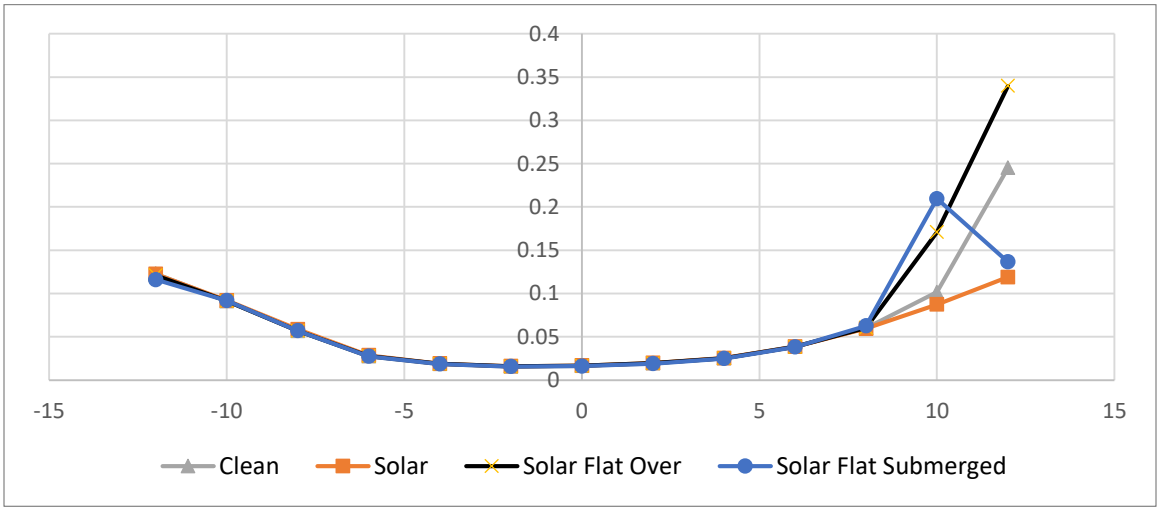

Figure 14 Drag coefficient VS. angle of attack for the different airfoil configurations

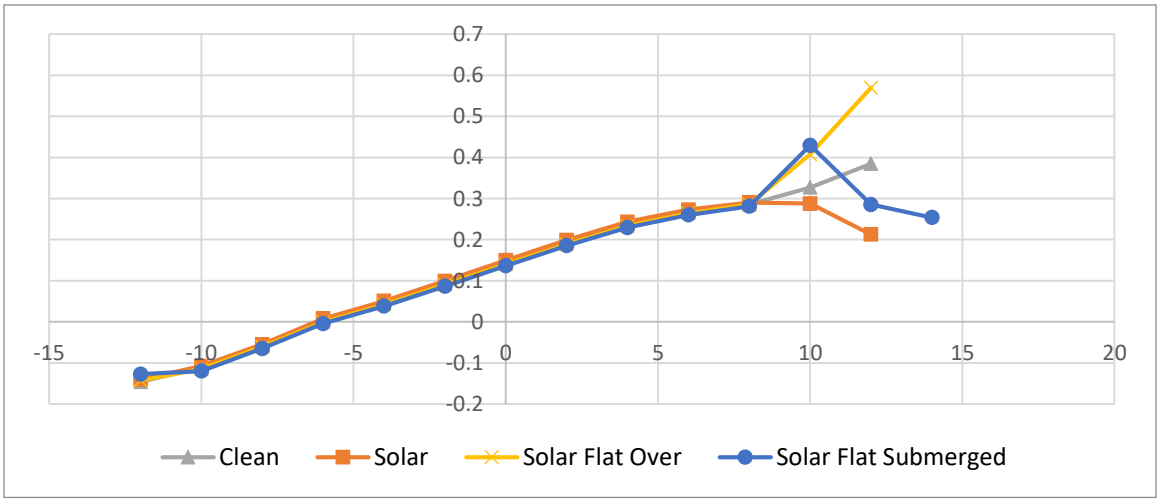

Figure 15 Moment coefficient VS. angle of attack for the different airfoil configurations

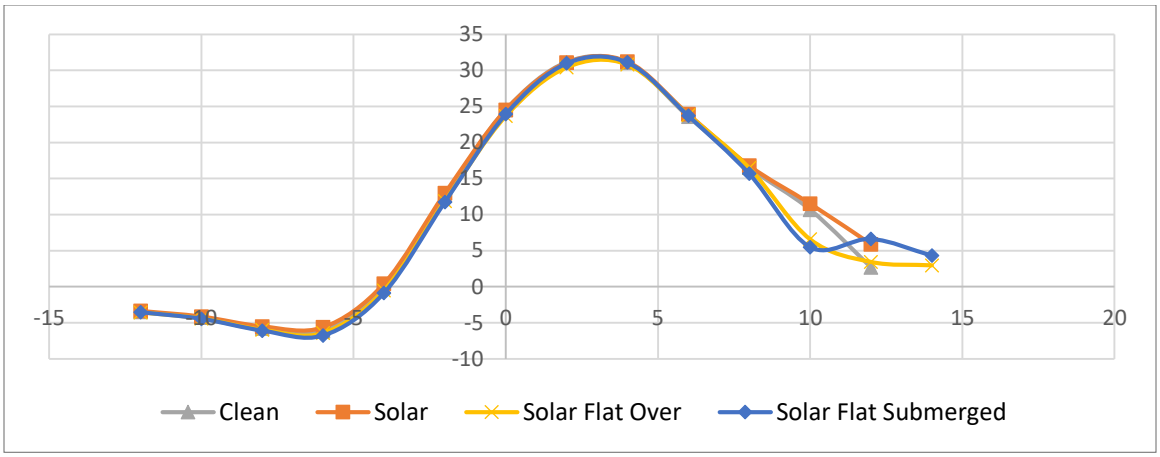

Figure 16 Lift to drag ratio VS. angle of attack for the different airfoil configurations

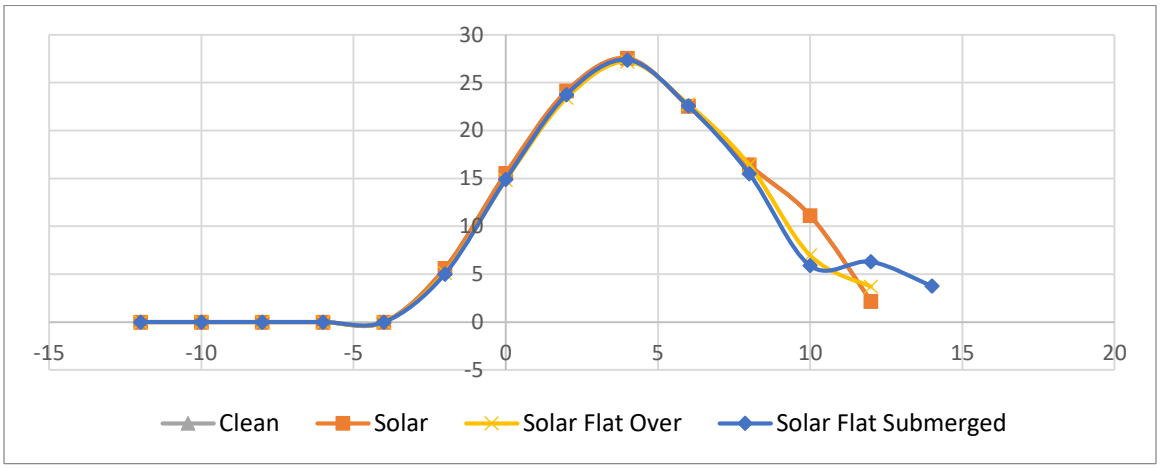

Figure 17 $C_L^{3/2}/C_D$ VS. angle of attack for the different airfoil configurations

3.2 Drag Decomposition

To understand how the drag is affected by the shape change, the drag is decomposed into pressure and viscus forces. Although all of the cases have almost the same drag, there is a countable difference. In Table 2, the drag decomposition in as a percent of 'clean' case, as illustrated in Figure 18.

It can be seen that the 'solar flat submerged' case has the minimum drag among all cases, while the 'solar over' case has the maximum. It seems that the the 'solar flat submerged' case has less pressure drag because the maximum-thickness is less. The contrary case happens for the 'solar over' case, where the maximum thickness is bigger, so the pressure drag is more compared to the clean case. In the same way, the 'solar flat over' case has more thickness compared to the clean case. Hence, pressure drag is more.

As for friction drag, less wetted area / airfoil perimeter shall create less friction drag. This can be applied for both 'flat' cases. On the other hand, this hypothesis does not explain the reduction in the viscous drag in the 'solar over' case. This issue needs to be studied in detail in a further study.

Table 2 Drag decomposition at AOA 6 degrees for the different airfoil configurations

Airfoil	*Pressure Drag*	*Viscous Drag*	*Total Drag*
clean	100.00%	100.00%	100.00%
solar flat over	100.20%	98.74%	100.04%

solar flat submerged	99.28%	98.20%	99.16%
solar over	101.63%	98.93%	101.33%

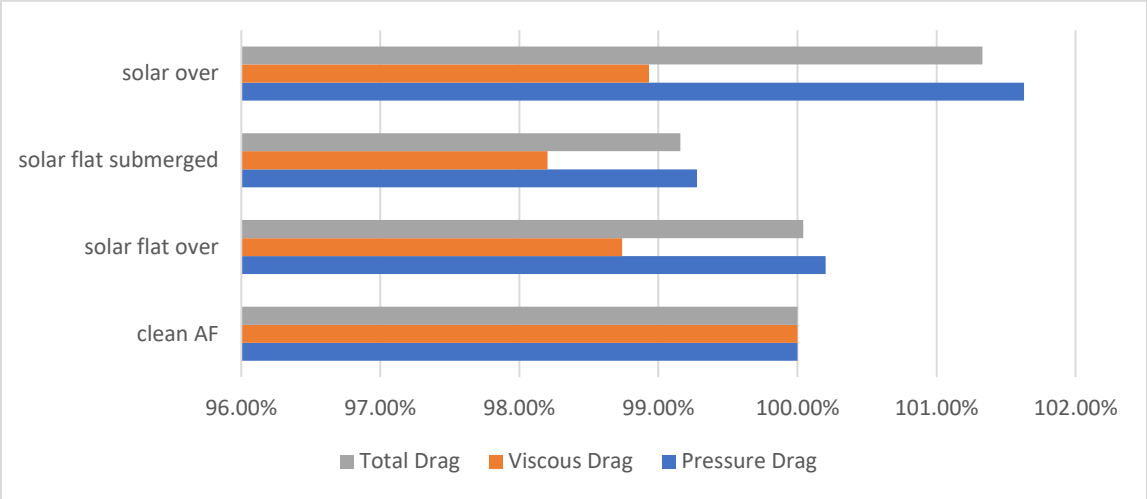

Figure 18 Drag decomposition at AOA 6 degrees for the different airfoil configurations

4. Parametric Study

4.1 Effect of the position of the Solar Panel

In this section a parametric study is presented, where the solar panel position is changed, to study the effect of its variation on the aerodynamic performance of the wing. The panel starting position has three values; 10, 25, and 40% of the chord. The panel length is 50% of the chord, as illustrated in Figure 19. The 25% case and the 'solar over' case are the same. So, the pressure and velocity contours are omitted hereafter.

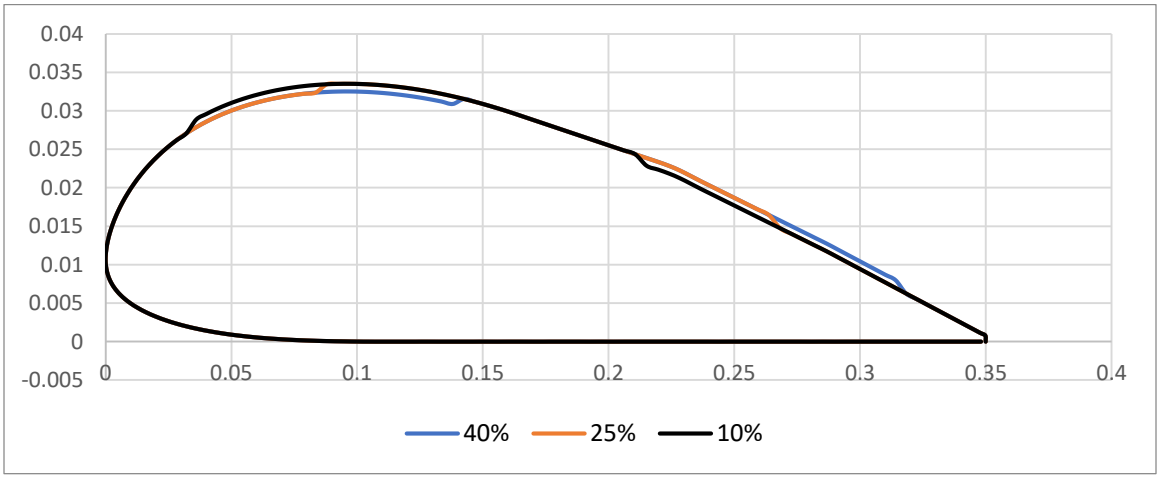

Figure 19 Studied Airfoil Configurations for different panel positions

The results, Figures 20-22, show that there is almost no variation in CL, CD, or CM, except that the 40% case has slightly higher Cl, and CM. Also, this can be more notable in the CL/CD and CL1.5/CD curves, Figures 23 and 24.

the pressure and velocity contours, Figures 25 and 26, also are almost identical. Hence, one can conclude that the airfoil characteristics are almost independent of the solar panel position.

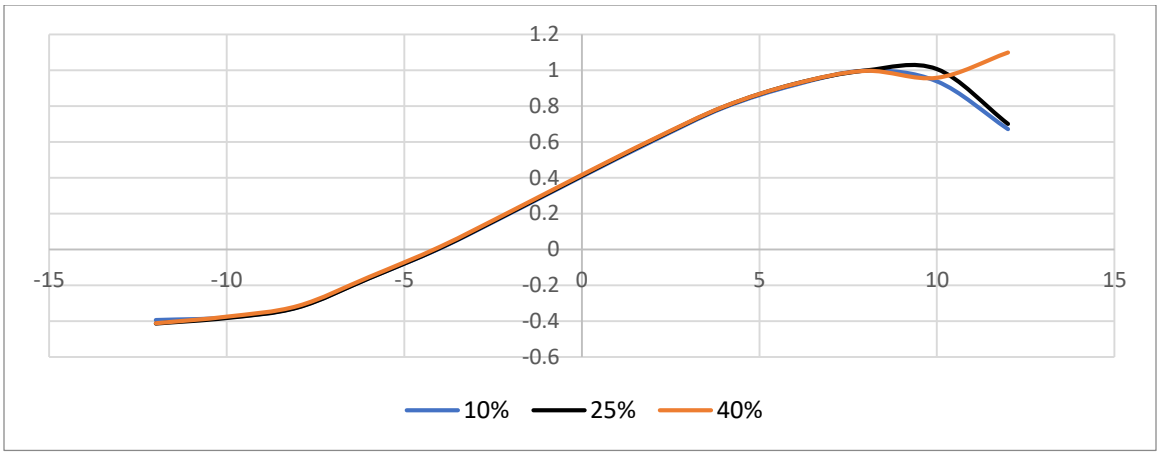

Figure 20 Lift coefficient VS. angle of attack for the different panel positions

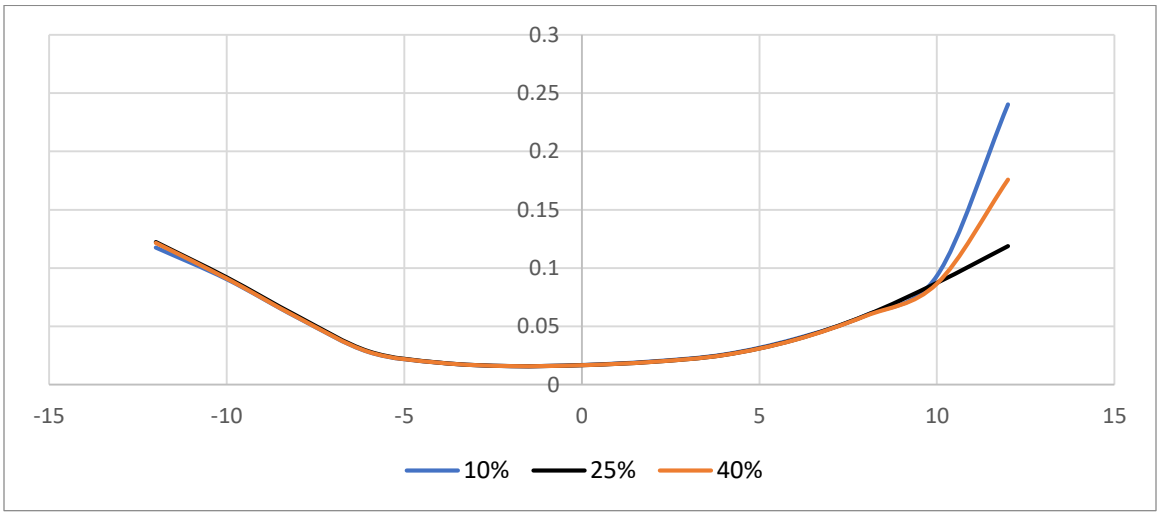

Figure 21 Drag coefficient VS. angle of attack for the different panel positions

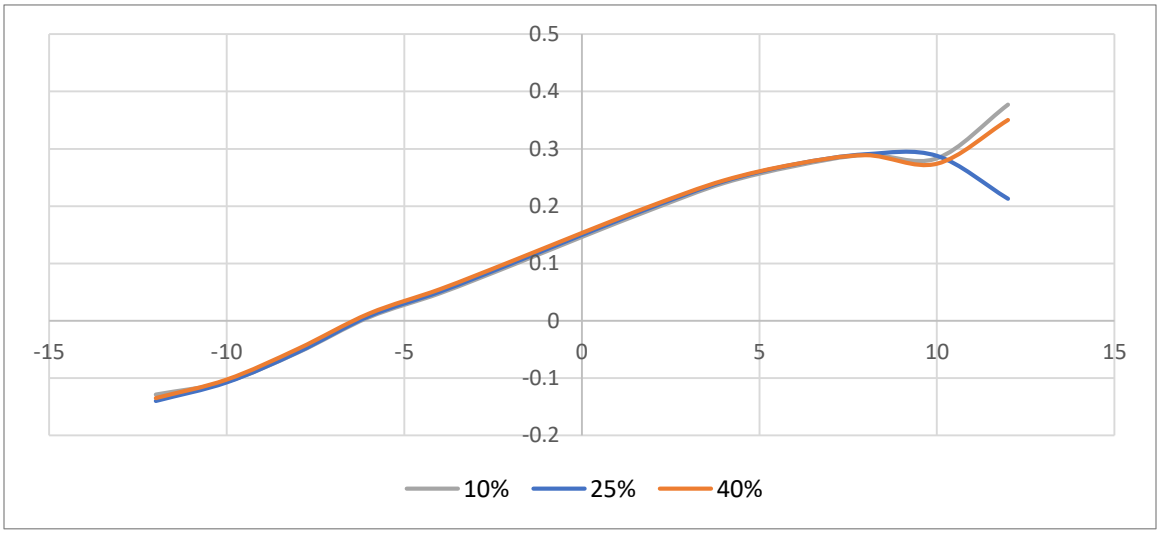

Figure 22Moment coefficient VS. angle of attack for the different panel positions

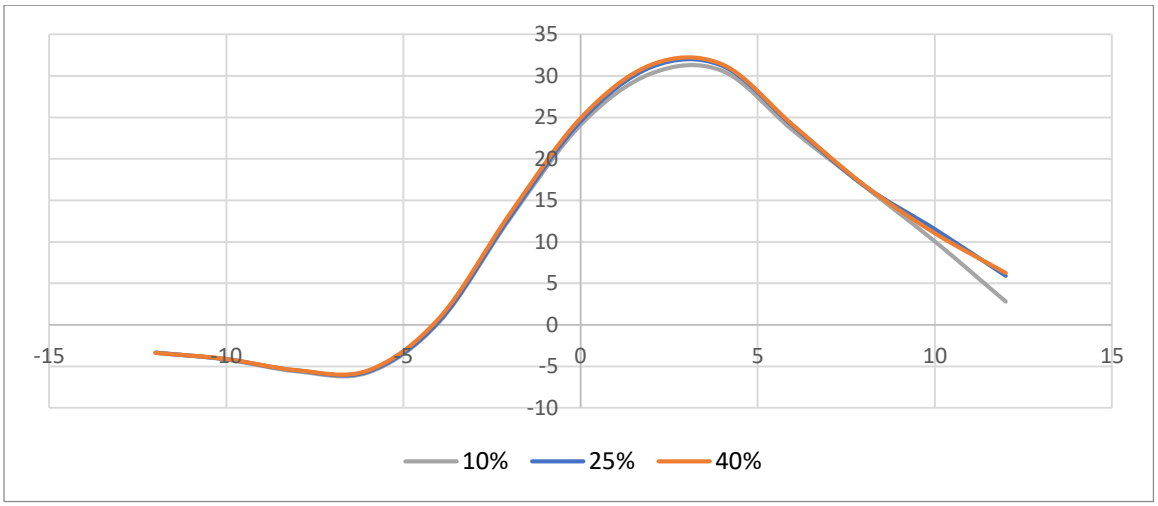

Figure 23 Lift to drag ratio VS. angle of attack for the different panel positions

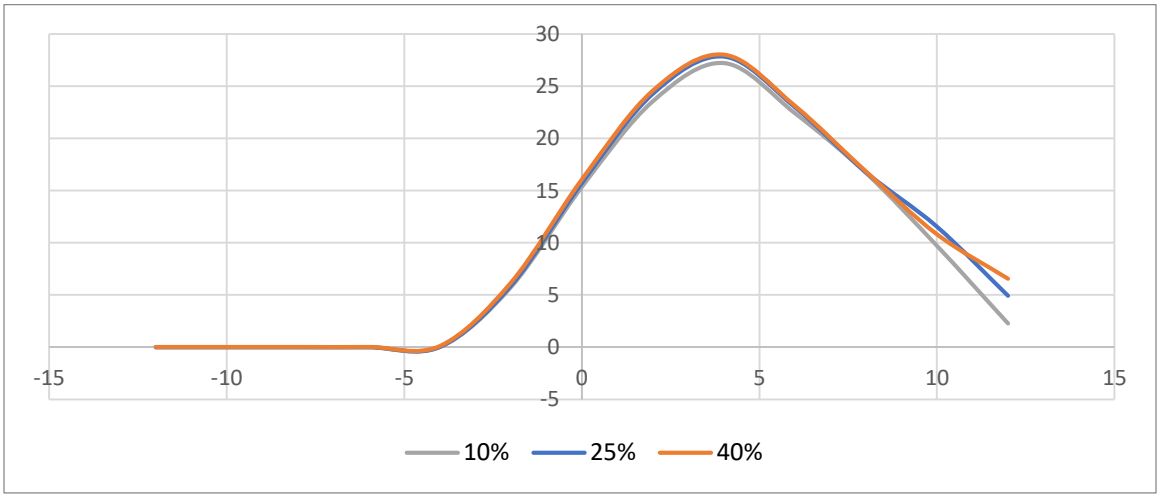

Figure 24 CL3/2/CD VS. angle of attack for the different panel positions.

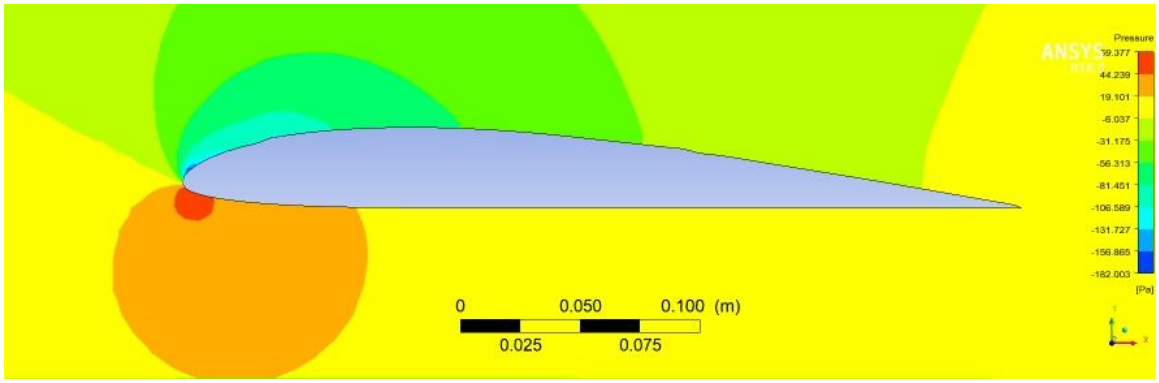

(a)

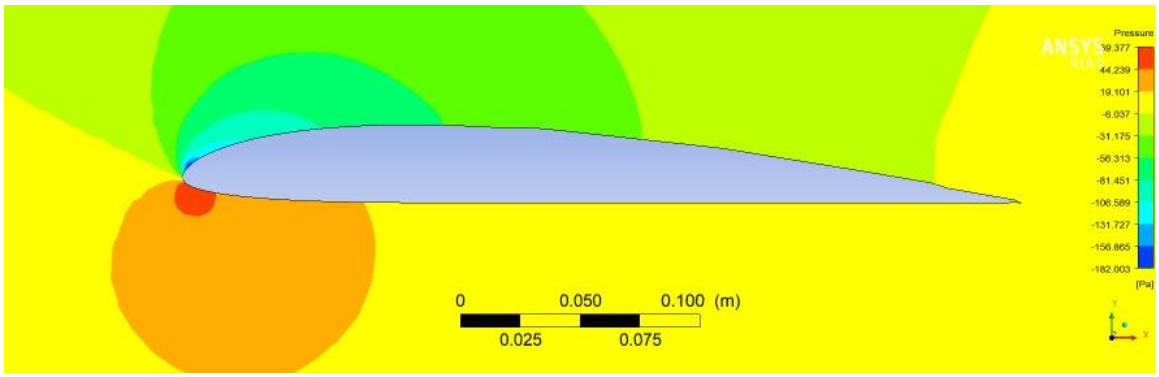

(b)

Figure 25 Pressure contour around airfoil AG34 at 6o angle of attack for the configurations a) cell starts at 10%, and b) cell starts at 40%

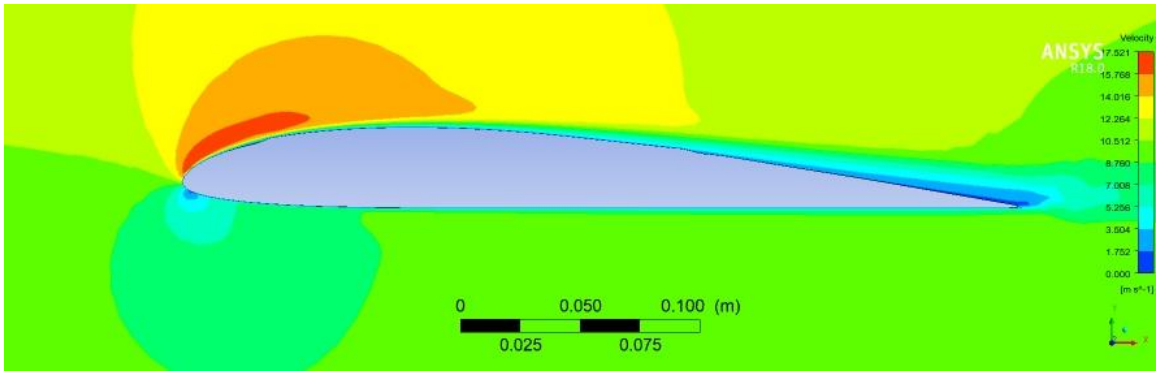

(a)

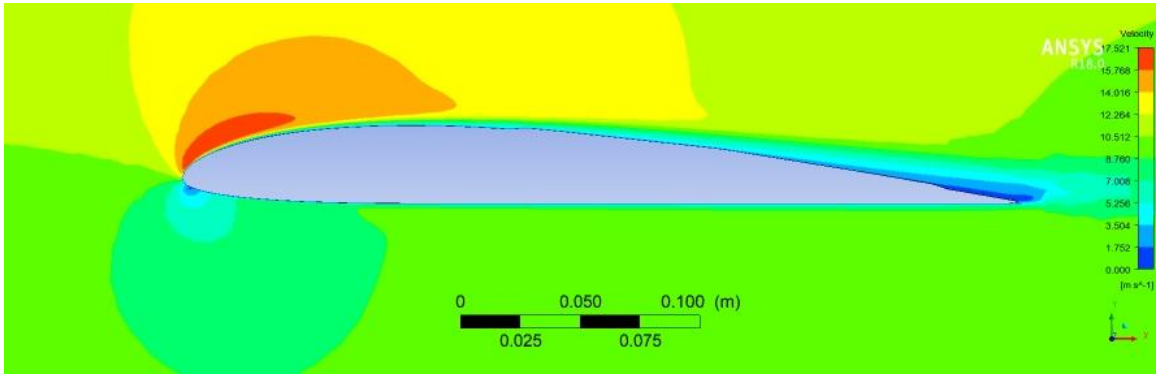

(b)

Figure 26 Velocity contour around airfoil AG34 at 6o angle of attack for the configurations a) cell starts at 10%, and b) cell starts at 40%

As for the Pressure distribution, there is a significant pressure jump at the start point of the solar panel. Along the panel, pressure recovers quickly, and so the pressure jump, located at the panel end, is very small. The pressure jump at the panel leading edge becomes less significant when the panel moves downstream. This is shown in Figure 27.

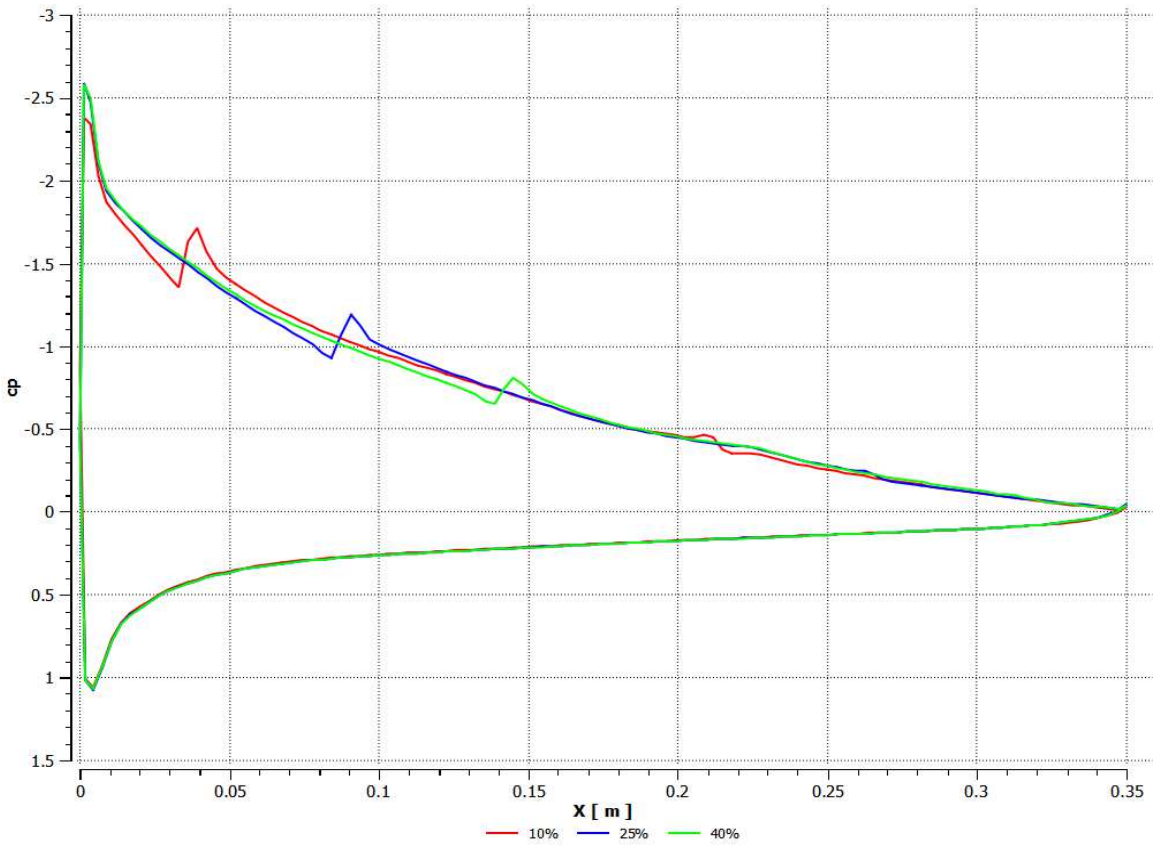

Figure 27 Pressure coefficient distribution over the configurations of different panel positions

4.2 Effect of the size of the Solar Panel

The second parametric study presented in this section considers the solar panel size effect on the aerodynamic performance of the wing. The panel length has three values; 50, 70, and 90% of the chord. The panel center is located in the airfoil center, as illustrated in Figure 28. The 50% case and the 'solar over' case are the same. So, the pressure and velocity contours are absent hereafter.

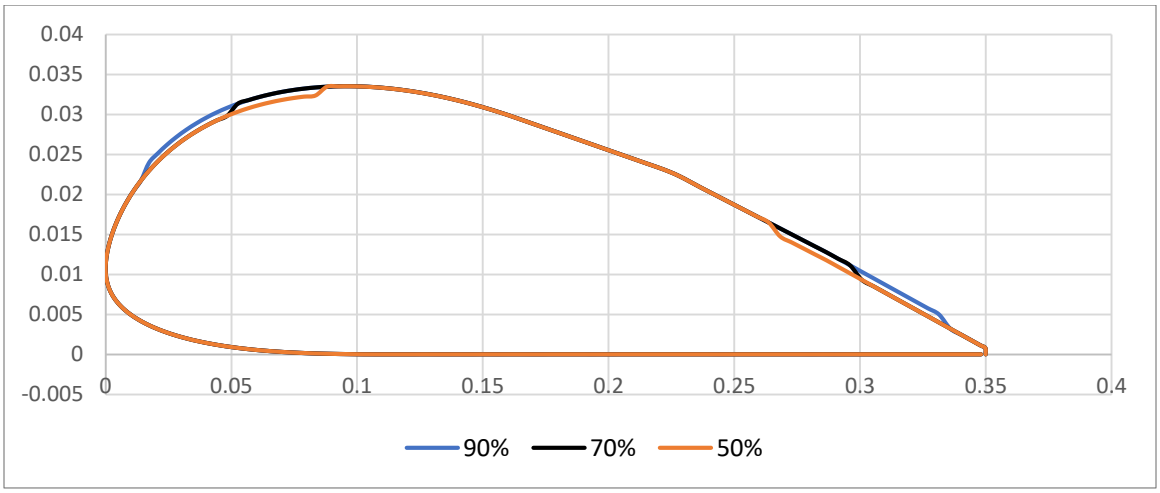

Figure 28 Studied Airfoil Configurations for different panel sizes

As for the aerodynamic coefficients, shown in Figures 29-31, CL and CD are identical. CM is also indifferent except for the 90% case, where its CM is slightly more. Considering CL/CD and $CL^{1.5}/CD$ parameters, the shorter panel has better performance. Again, the difference between the cases is rather small, as shown in Figures 32 and 33.

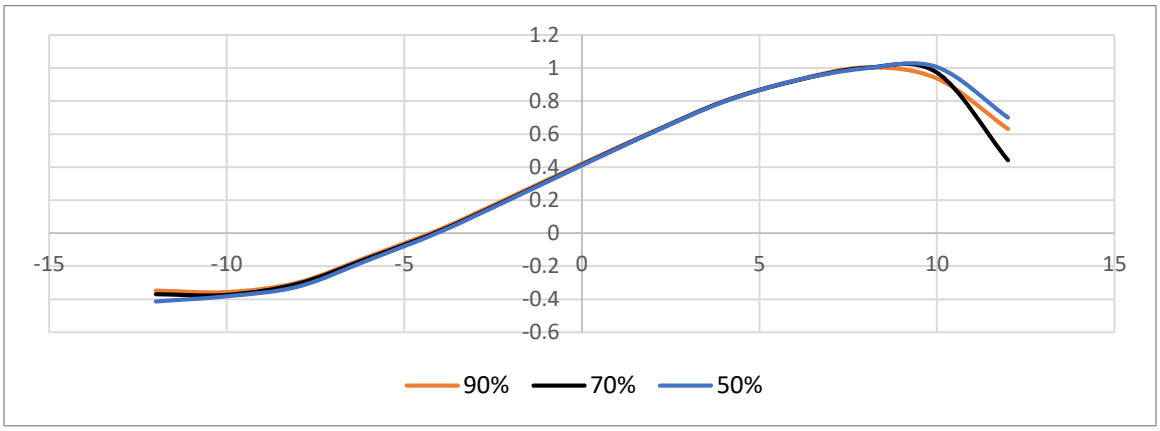

Figure 29 Lift coefficient VS. angle of attack for the different panel sizes

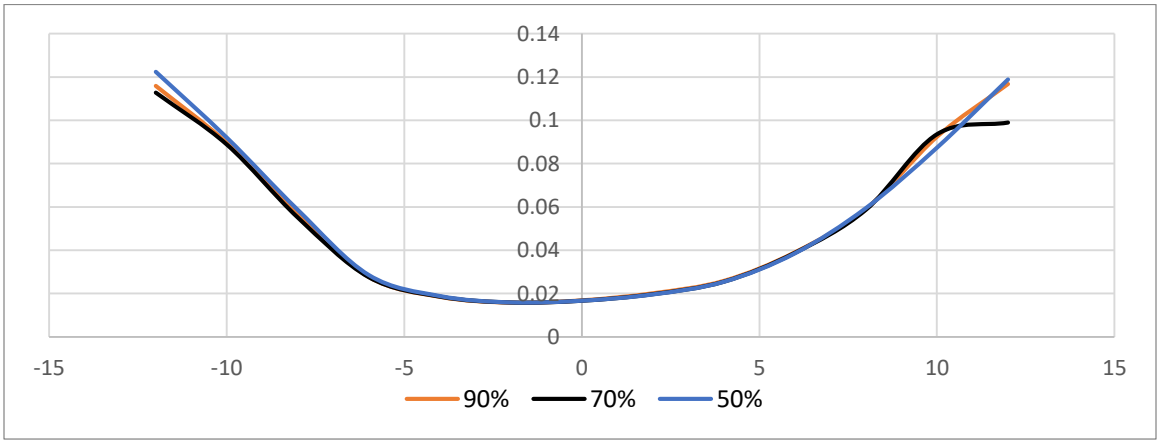

Figure 30 Drag coefficient VS. angle of attack for the different panel sizes

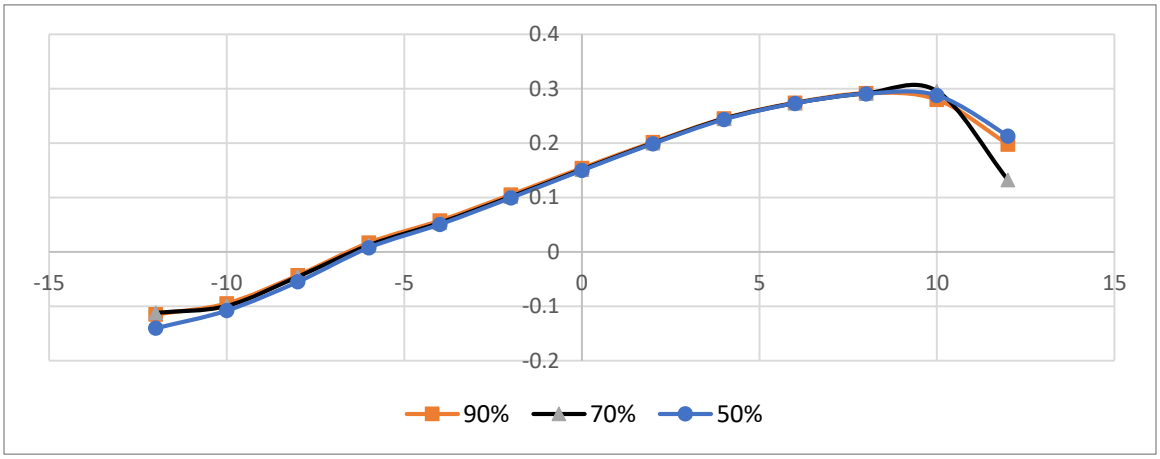

Figure 31 Moment coefficient VS. angle of attack for the different panel sizes

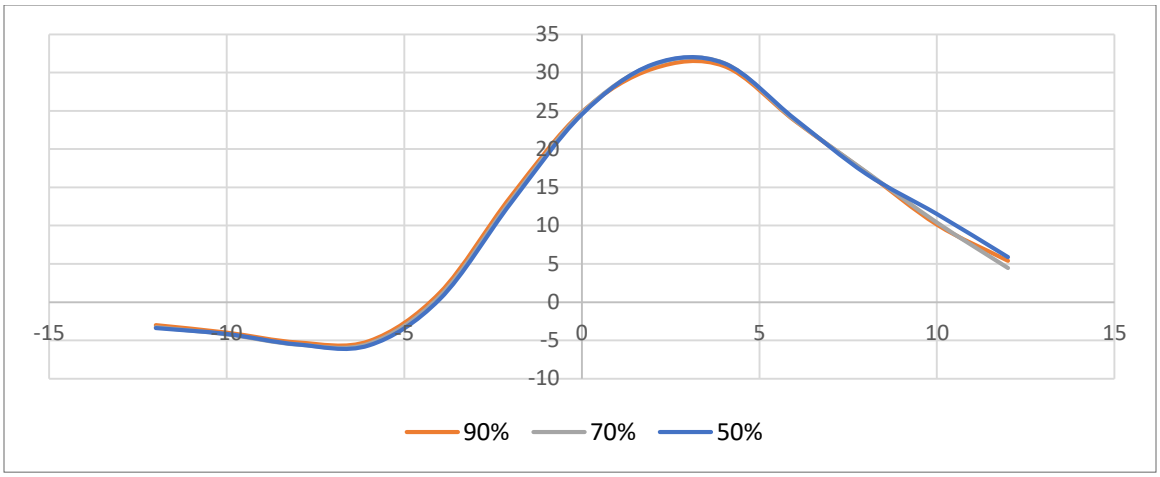

Figure 32 Lift-to-drag ratio coefficient VS. angle of attack for the different panel sizes

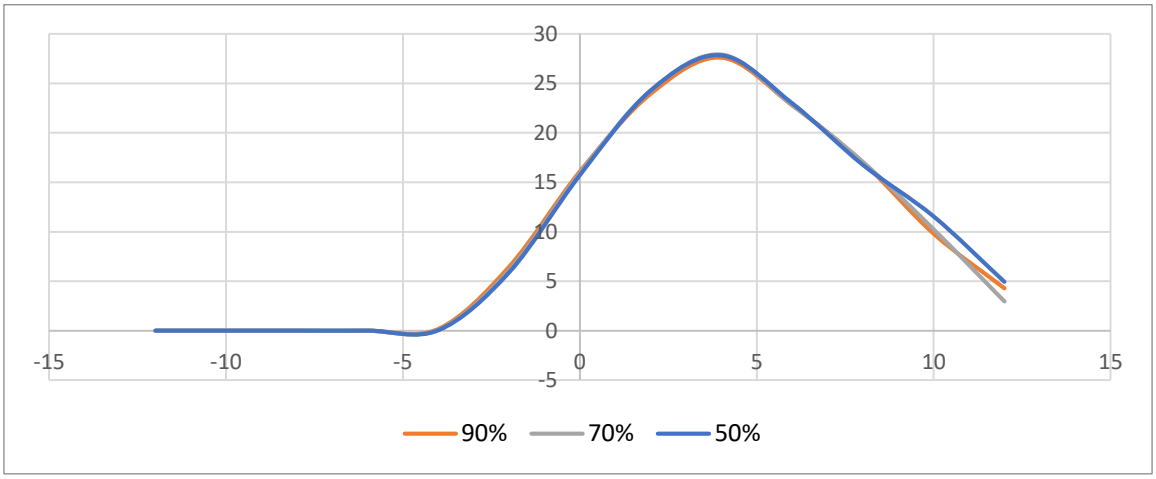

Figure 33 CL3/2/CD VS. angle of attack for the different panel sizes

As for the Pressure distribution, the same behavior of Figure 27 appears again. There is a significant pressure jump at the start point of the solar panel. Along the panel, pressure recovers quickly, and so the pressure jump, located at the panel end, is very small. The pressure jump at the panel leading edge becomes less significant when the panel moves downstream, as shown in Figure 34. Velocity and pressure contours are also indifferent, as shown in Figures 35 and 36.

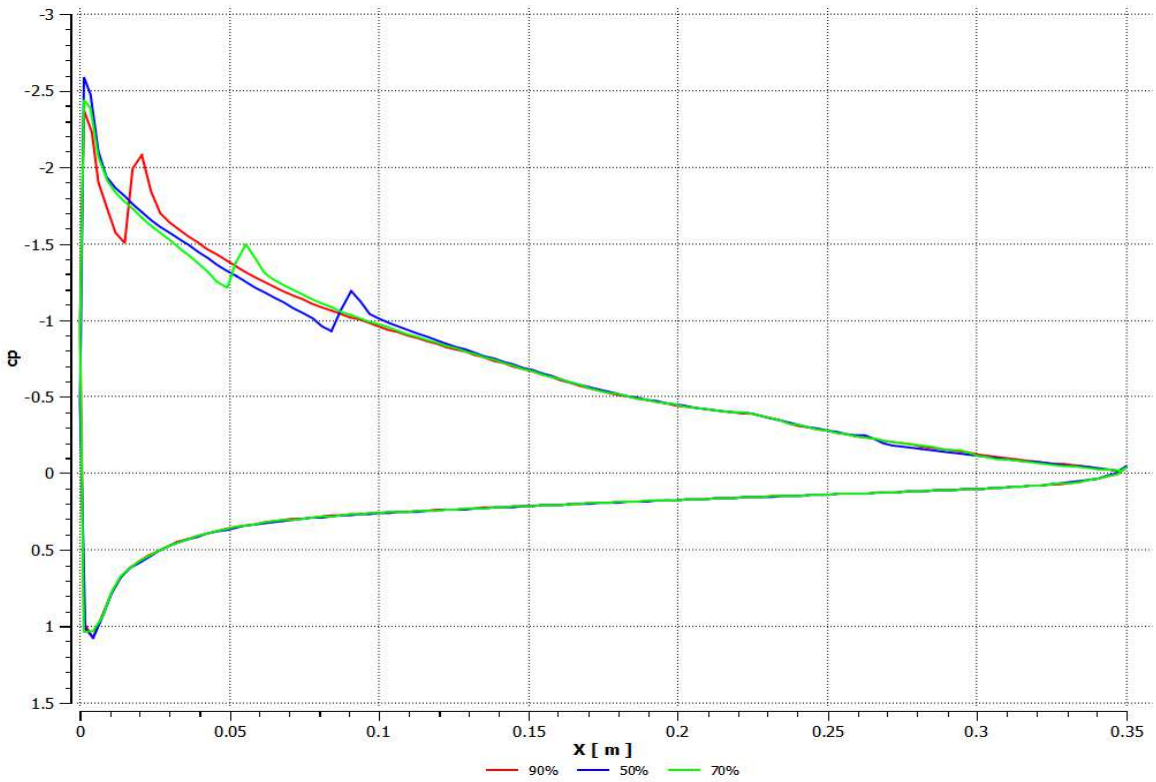

Figure 34 Pressure coefficient distribution over the configurations of different panel sizes

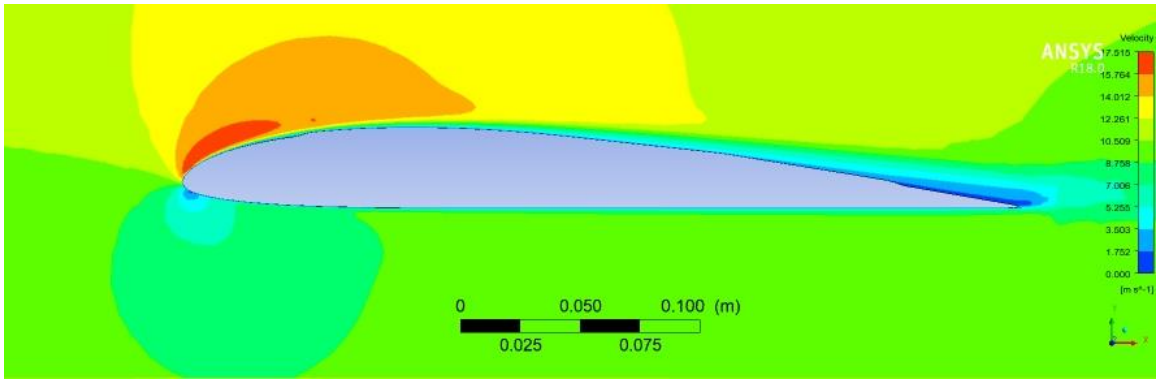

(a)

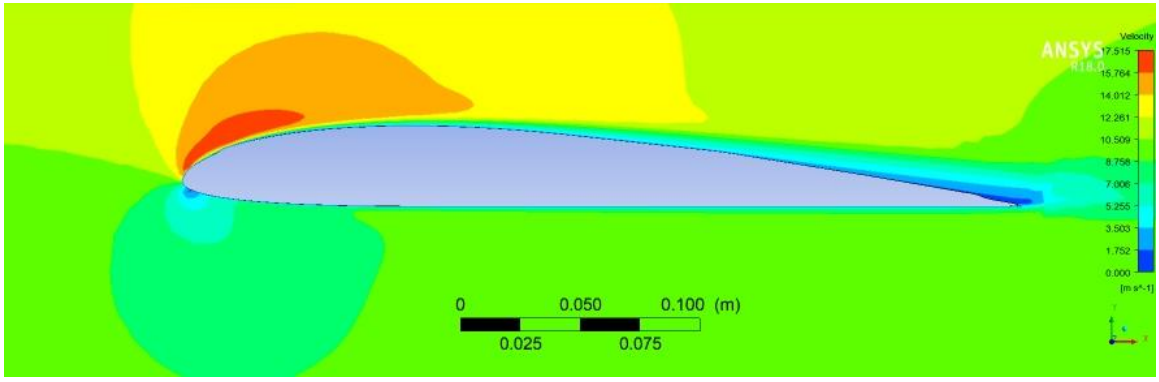

(b)

Figure 35 Velocity contour around airfoil AG34 at 6o angle of attack for the configurations a) cell covers 70%, and b) cell covers 90%

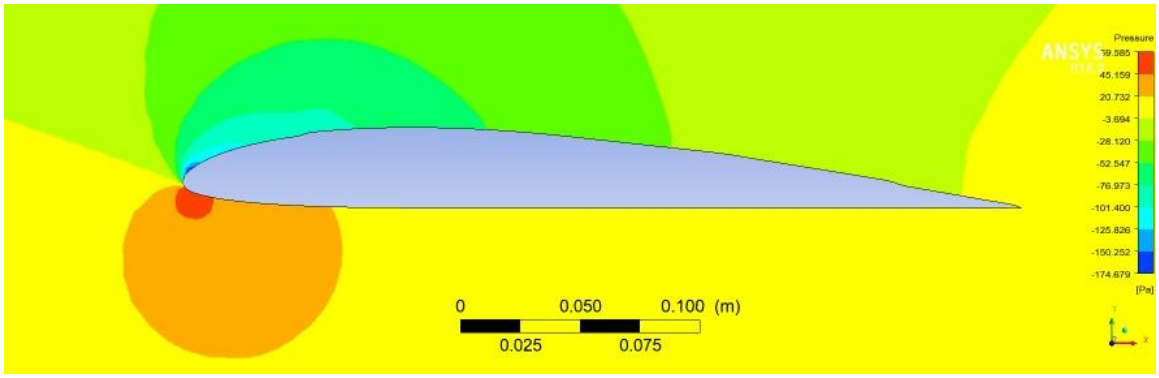

(a)

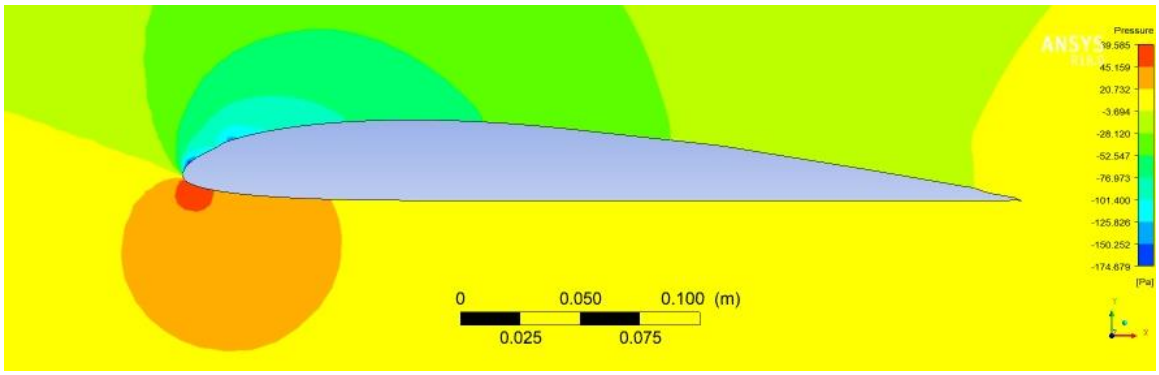

(b)

Figure 36 Pressure contour around airfoil AG34 at 6o angle of attack for the configurations a) cell covers 70%, and b) cell covers 90%

4.3 Effect of the Thickness of the Solar Panel

The third parametric study presented in this section considers the solar panel thickness effect on the aerodynamic performance of the wing. Although the solar panels are quite thin, this study considers the extreme cases where the panel mounting is rather thick. The panel thickness has three values; 1, 3, and 5 mm. The panel center is located in the airfoil center, and its length is 50% chord, as illustrated in Figure 37. The 1 mm case and the 'solar over' case are the same. So, the pressure and velocity contours are absent hereafter.

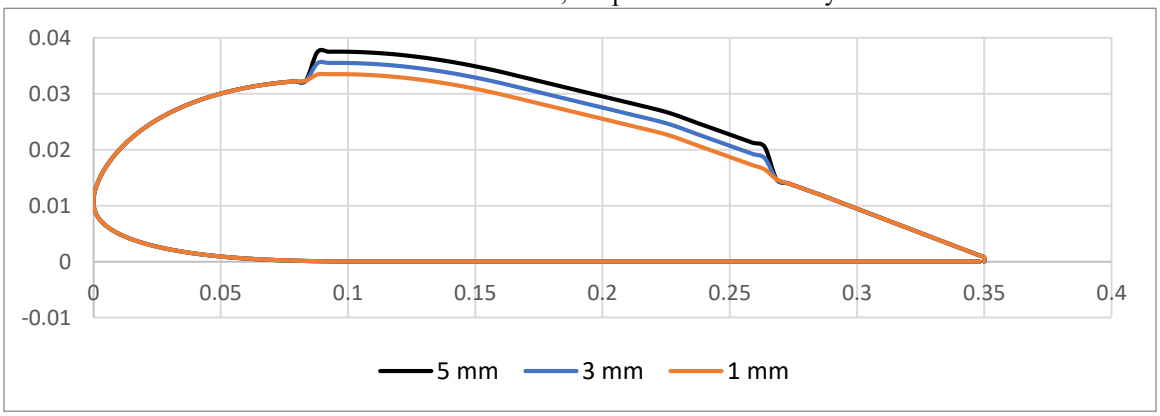

Figure 37 Studied Airfoil Configurations for different panel thicknesses

At low angles of attack, CL is the same for all cases, as shown in Figure 38. The variation starts to appear at angle of 4o. It shows that the thicker airfoil is, the less CL possible. As for CD, all cases show similar trend with an obvious difference between cases. As the solar panel setup thickness increases, CD increases significantly. This is illustrated in Figure 39. The CM curves are identical, but as the thickness increases, the slope slightly decreases, as illustrated in Figure 40. Considering CL/CD and $CL^{1.5}/CD$ parameters, there is an obvious change, with a maximum at 4o. as the thickness increases, the CL/CD and $CL^{1.5}/CD$ decrease severely, as shown in Figures 41 and 42.

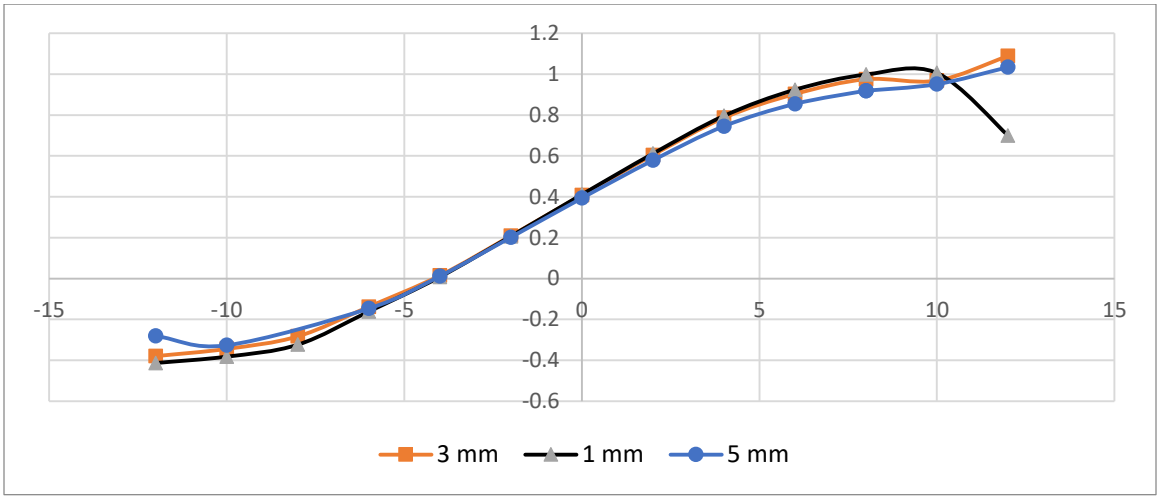

Figure 38 Lift coefficient VS. angle of attack for the different panel thicknesses

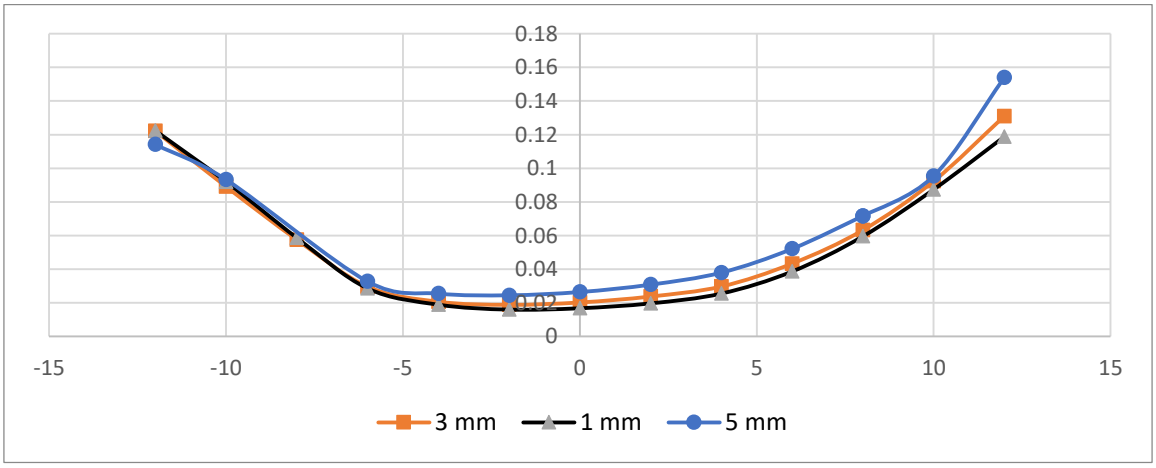

Figure 39 Drag coefficient VS. angle of attack for the different panel thicknesses

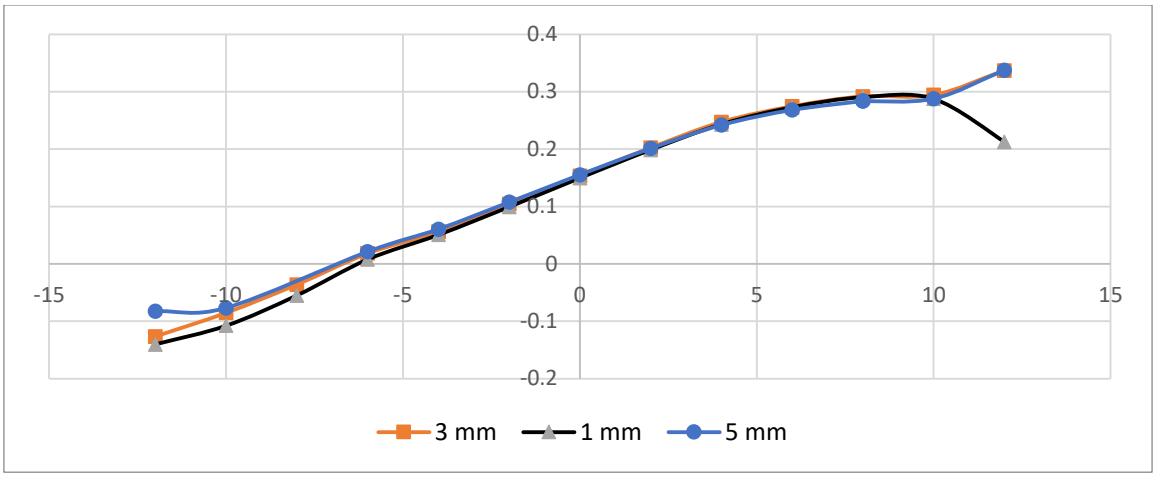

Figure 40 Moment coefficient VS. angle of attack for the different panel thicknesses

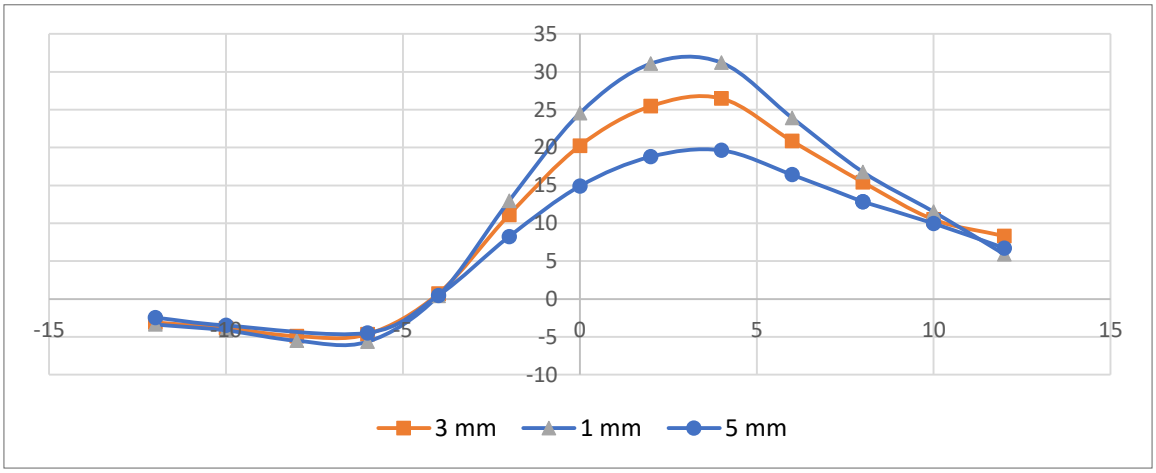

Figure 41 Lift-to-drag ratio VS. angle of attack for the different panel thicknesses

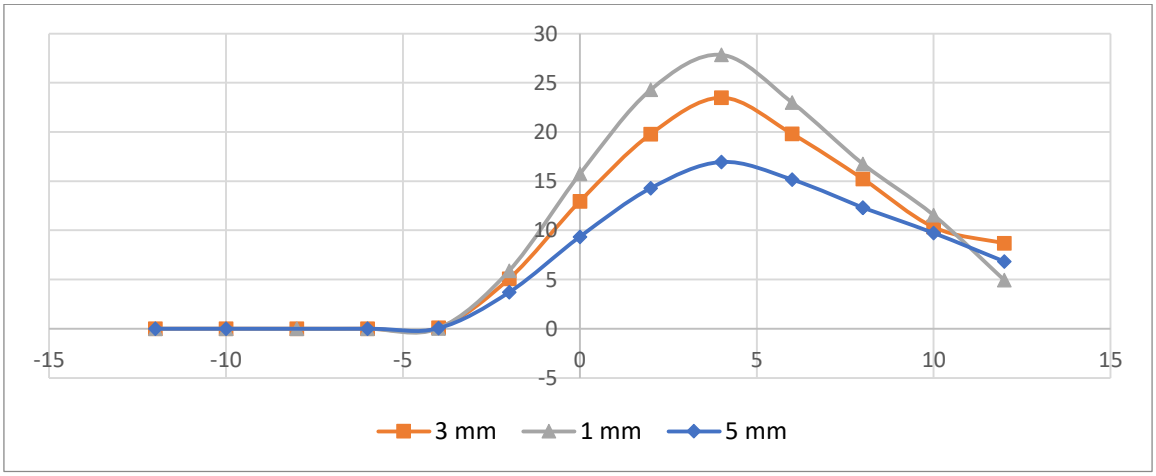

Figure 42 CL3/2/CD VS. angle of attack for the different panel thicknesses

As for the Pressure distribution, the behavior appears different, even near the leading edge. The leading-edge negative pressure jump decreases as the thickness increases, which has an unfavorable effect on the airfoil. At the solar panel starting point the pressure jump increases significantly as the panel thickness increases.

Along the panel, pressure recovers quickly as usual, and so the pressure jump, located at the panel end, is very small, as shown in Figure 43. Yet, in the vicinity of the trailing edge, there is mismatch for the different cases. The pressure is less for the thickest panel

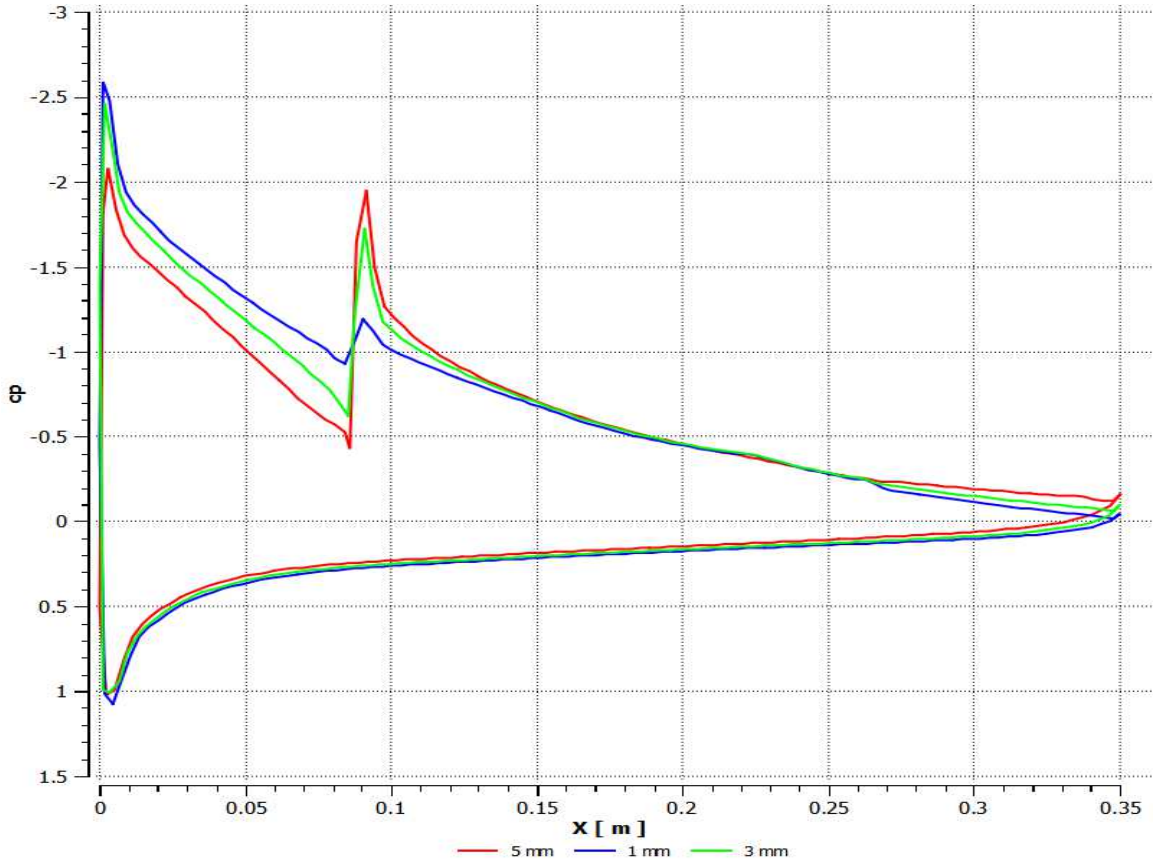

Figure 43 Pressure coefficient distribution over the configurations of different panel thicknesses

Velocity and pressure contours show the significant effect of the panel thickness, as shown in Figures 44 and 45. Pressure contours show that at the leading edge the pressure is more negative for the 5 mm case. besides, there is a local positive pressure zone in the vicinity of the solar panel start, followed by a negative zone. Intensity of these zones increases as the panel becomes thicker.

Velocity contours show that for the case of 5 mm, in the vicinity of the panel start there is a local flow acceleration, while further downstream the flow is slower and, hence, separation increases. Also, near the trailing edge at the lower airfoil surface, the flow accelerates once more, and the accelerated flow regime increases as the panel thickness over the upper surface increases.

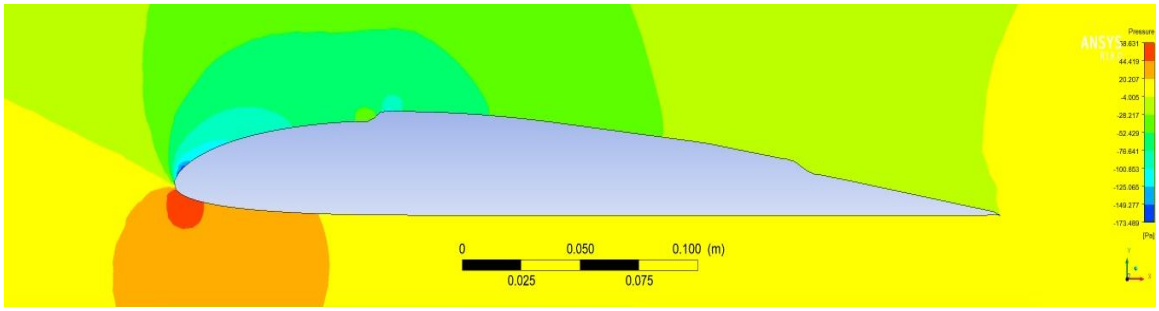

(a)

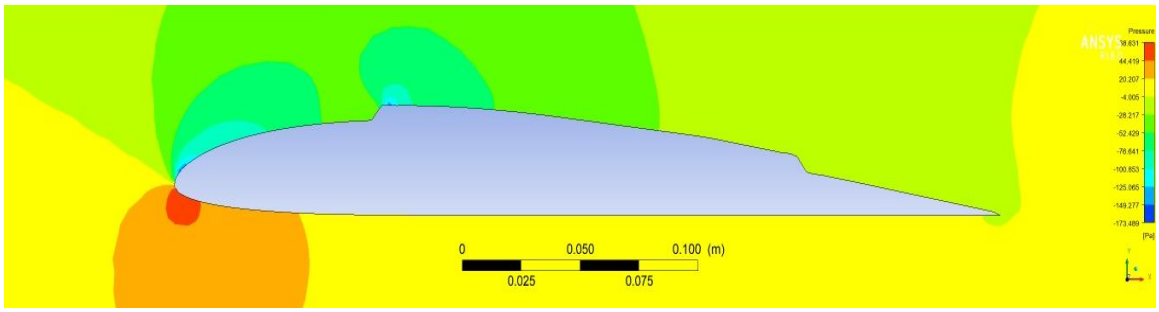

(b)

Figure 44 Pressure contour around airfoil AG34 at 6o angle of attack for the solar panel of thickness a) 3 mm, and b) 5 mm

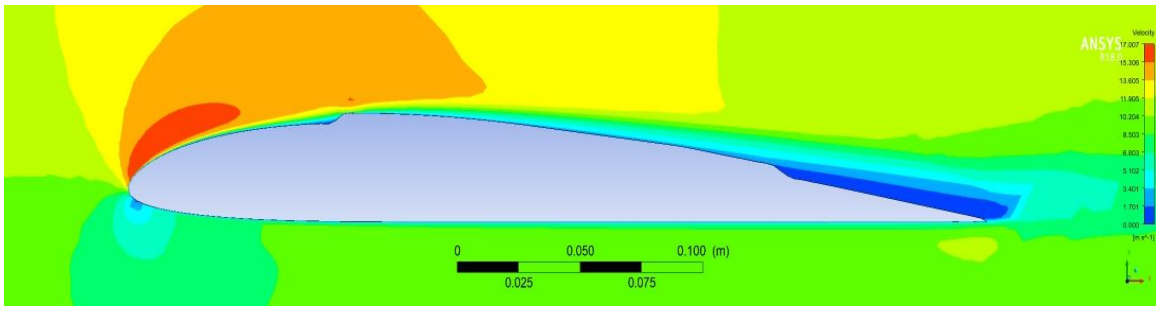

(a)

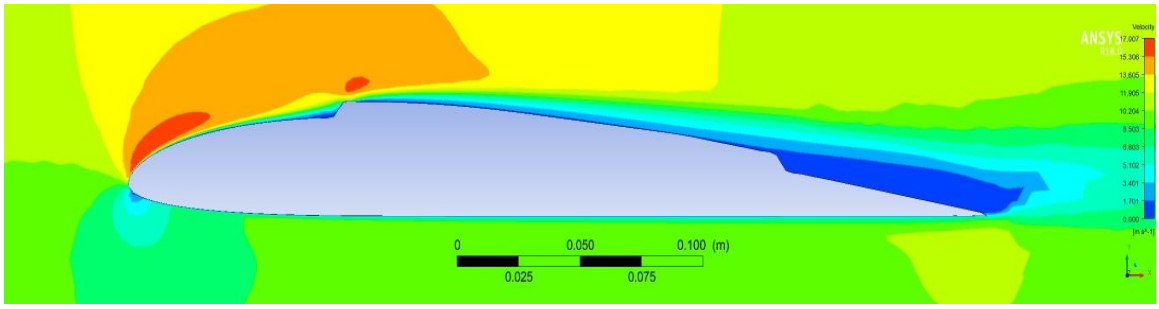

(b)

Figure 45 Velocity contour around airfoil AG34 at 6o angle of attack for the solar panel of thickness a) 3 mm, and b) 5 mm

5. Conclusion

This study investigates the effect of adding a solar panel over an airfoil of a small unmanned aircraft. Several panel geometries are studied. It is shown that the solar panel has a limited effect on the airfoil performance; lift, drag, and moment coefficients. A parametric study of solar panel position, size, and thickness is conducted. It is found that as the panel tip becomes closer to the leading edge, the lift slightly increases. The panel size is almost ineffective. The panel thickness has a significant effect on the airfoil performance. As the panel thickness increases, the lift decreases notably, while drag increases severely. This has a significant effect on the lift-to-drag ratio and the general aircraft performance. For the current case study, panel thickness up to 1 mm has a negligible effect on the airfoil.

Acknowledgements

The authors appreciate the fruitful discussions and recommendations of Dr. Sergey Serokhvostov, of Moscow Institute of Physics and Technology, Department of Aeromechanics and Flight Engineering.

Declarations

Availability of data and materials

Not applicable

Competing interests

Not applicable

Funding

Not applicable

Authors' contributions

Not applicable

Acknowledgements

The authors appreciate the fruitful discussions and recommendations of Dr. Sergey Serokhvostov, of Moscow Institute of Physics and Technology, Department of Aeromechanics and Flight Engineering.

Authors' information (optional)

Not applicable

References

1. Gao, X. Z., Hou, Z. X., Guo, Z., & Chen, X. Q. (2015). Reviews of methods to extract and store energy for solar-powered aircraft. Renewable and Sustainable Energy Reviews, 44, 96-108.
2. Richfield, P. Aloft for 5 Years: DARPA's Vulture Project Aims for Ultra Long UAV Missions. Defense News, Vol. 22, No. 30, July 2007, p. 30.
3. Baldock, N. and Mokhtarzadeh-Dehghan, M.R., "A Study of Solar-Powered, High-Altitude Unmanned Aerial Vehicles," Aircraft Engineering and Aerospace Technology: An International Journal, Vol. 78, No. 3, 2006, pp. 187–193.
4. Boucher, R. J., "History of Solar Flight," 20th Joint Propulsion Conference, AIAA-84-1429, Cincinnati, Ohio, USA, June 1984.
5. Boucher, R. J., "Sunrise: The World's First Solar-Powered Airplane," Journal of Aircraft, Vol. 22, No. 10, 1985, pp. 840–846.
6. Ramos A.C.B., Shiguemori E.H., Serokhvostov S., Gupta P.K., Zhong L., Hu X.B. 2018. Solar-Powered UAV Platform System: A Case Study for Ground Change Detection in BRIC Countries. In: Latifi S. (eds) Information Technology - New Generations. Advances in Intelligent Systems and Computing, vol 738. Springer, Cham.
7. Noll, T.E., Ishmael, S.D., Henwood, B., Perez-Davis, M.E., Tiffany, G.C., Madura, J., Gaier, M., Brown, J.M. and Wierzbanowski, T., 2007. Technical findings, lessons learned, and recommendations resulting from the Helios prototype vehicle mishap. National Aeronautics and Space Admin Langley Research Center Hampton VA.

8. Montgomery, S., & Mourtos, N. (2013). Design of a 5 Kilogram Solar-Powered Unmanned Airplane for Perpetual Solar Endurance Flight. In 49th AIAA/ASME/SAE/ASEE Joint Propulsion Conference (p. 3875).
9. Ross, H. (2008). Fly around the world with a solar powered airplane. In The 26th Congress of ICAS and 8th AIAA ATIO (p. 8954).
10. Kumar, G., Sepat, S., & Bansal, S. (2015). Review paper of solar-powered UAV. International Journal of Scientific & Engineering Research, 6(2), 41-44.
11. Wu, J., Wang, H., Li, N., Yao, P., Huang, Y., & Yang, H. (2018). Path planning for solar-powered UAV in urban environment. Neurocomputing, 275, 2055-2065.
12. Andrew, T. K., and Pierre, T. K., "Solar-Powered Aircraft: Energy Optimal Path Planning and Perpetual Endurance," Journal of Guidance, Control, and Dynamics, Vol. 32, No. 4, 2009, pp. 1320–1329.
13. Serokhvostov, S., & Churkina, T. E. (2016). Optimization of the trajectory and accumulator mass for the solar-powered airplane. International Council of the Aeronautics Sciences.
14. Shiau, J., Ma, D., Chiu, C., and Shie, J., "Optimal Sizing and Cruise Speed Determination for a Solar-Powered Airplane," Journal of Aircraft, Vol. 47, No. 2, 2010, pp. 622–629.
15. Sara, C. S., and Elmer, G. G., "Power Optimization of Solar-Powered Aircraft with Specified Closed Ground Tracks," Journal of Aircraft, Vol. 50, No. 1, 2013, pp. 232–238.
16. Barbosa, L. and Andrade de Oliveira, P., "Weight Analysis for Low-Speed and Sun-Powered Aircraft," SAE Technical Paper 2014-36-0508, 2014.
17. Serokhvostov, S. V., & Churkina, T. E. (2008). Optimal Control for The Sun-Powered Airplane in a Multi-Day Mission. Transport & Engineering, 27.
18. Ma, D., Shiau, J., Su, Y., and Chen, Y., "Optimal Level Turn of Solar Powered Unmanned Aerial Vehicle Flying in Atmosphere," Journal of Guidance, Control, and Dynamics, Vol. 33, No. 5, 2010, pp. 1347–1356.
19. Daniel, J. E., Aaron, D. K., Matthew, K., Stearns, H., David, A. S., Phillip, P. J., Robert, W., and Raymond, H., "Maximizing Net Power in Circular Turns for Solar and Autonomous Soaring Aircraft," Journal of Aircraft, Vol. 53, No. 5, 2016, pp. 1237–1247.
20. Barbarino, S., Bilgen, O., Ajaj, R. M., Friswell, M. I., & Inman, D. J. (2011). A review of morphing aircraft. Journal of intelligent material systems and structures, 22(9), 823-877.z
21. Wu, M., Shi, Z., Xiao, T., Chen, Z. L. J., & Ang, H. (2019). Effect of solar cell efficiency and flight condition on optimal flight control and energy performance for Z-shaped wing stratospheric solar aircraft. Acta Astronautica, 164, 366-375.
22. El-Salamony, M., Aziz, M. 2018. "Analysis of N Shaped Morphing Wing: Aerodynamic Prospective". In Proceedings of 4th Extremal and Record-Breaking Aircrafts Workshop (ERBA), Russia.
23. Abu-Mulaweh, H. I. (2003). A review of research on laminar mixed convection flow over backward- and forward-facing steps. International Journal of Thermal Sciences, 42(9), 897-909.
24. Pope, S. B. 2000. Turbulent Flows, Cambridge University Press.
25. Nelson, R. C. 1998. Flight stability and automatic control. New York: WCB/McGraw Hill
26. Drela, M. (1989). XFOIL: An analysis and design system for low Reynolds number airfoils. In Low Reynolds number aerodynamics (pp. 1-12). Springer, Berlin, Heidelberg.
27. Drela, M. (2014). Flight vehicle aerodynamics. MIT press.
28. Anderson, J. D. (1999). Aircraft performance and design, Boston: WCB/McGraw-Hill.

Figures

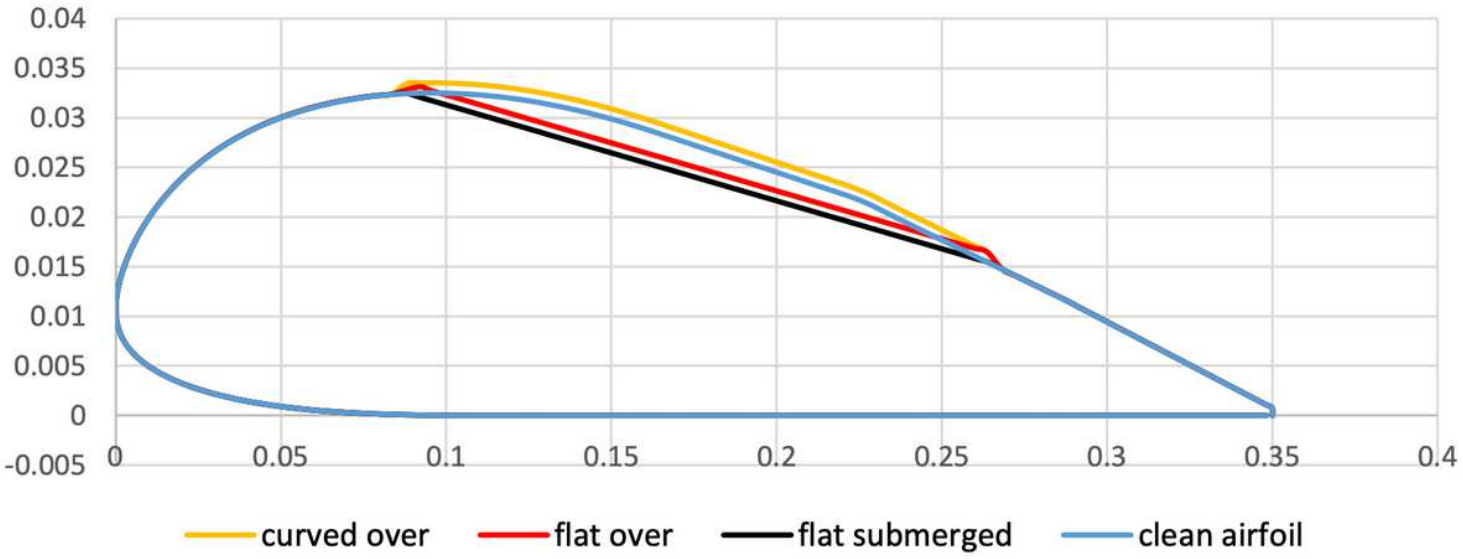

Figure 1

Studied Airfoil Configurations.

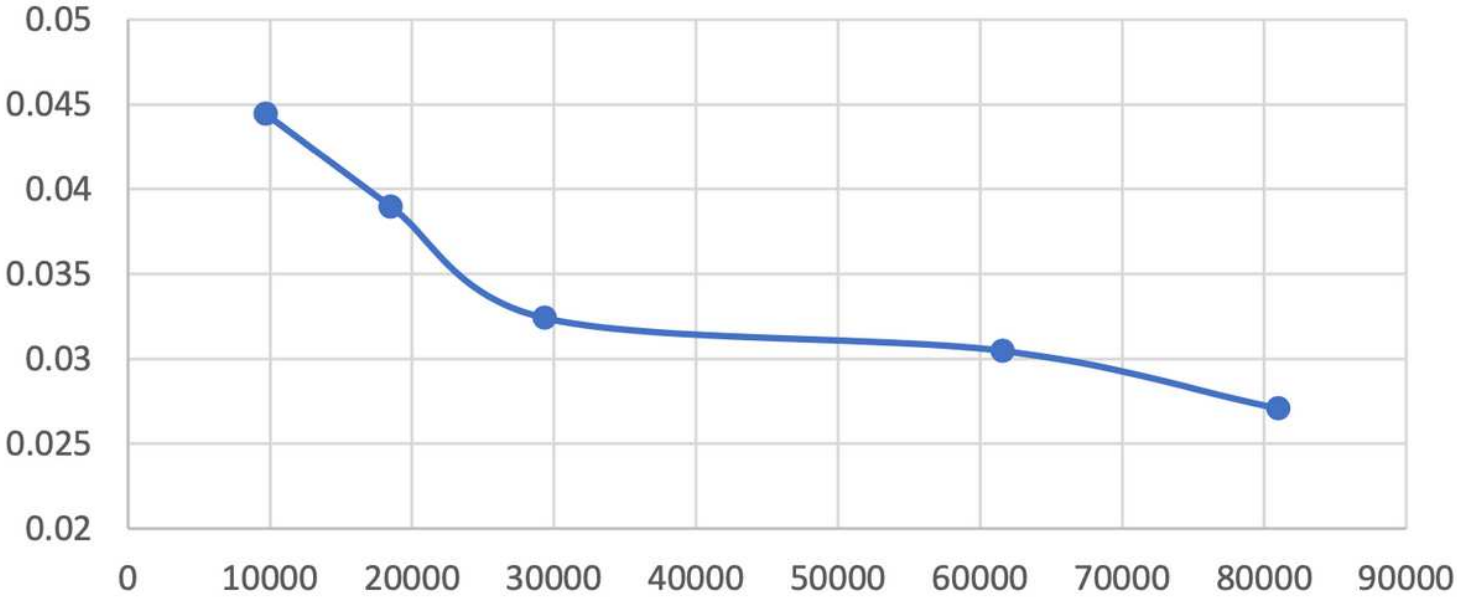

Figure 2

the drag coefficient variation with mesh nodes

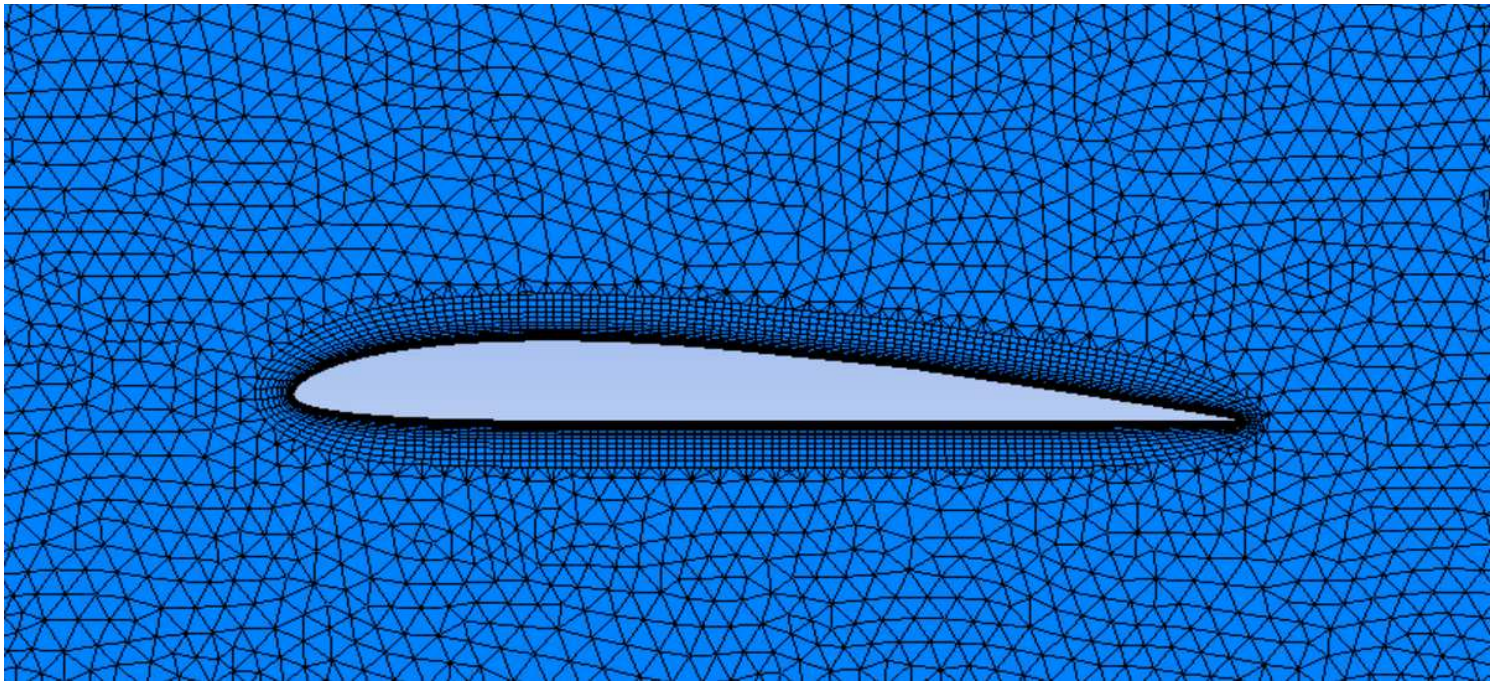

Figure 3

the two-dimensional mesh around the studied airfoil

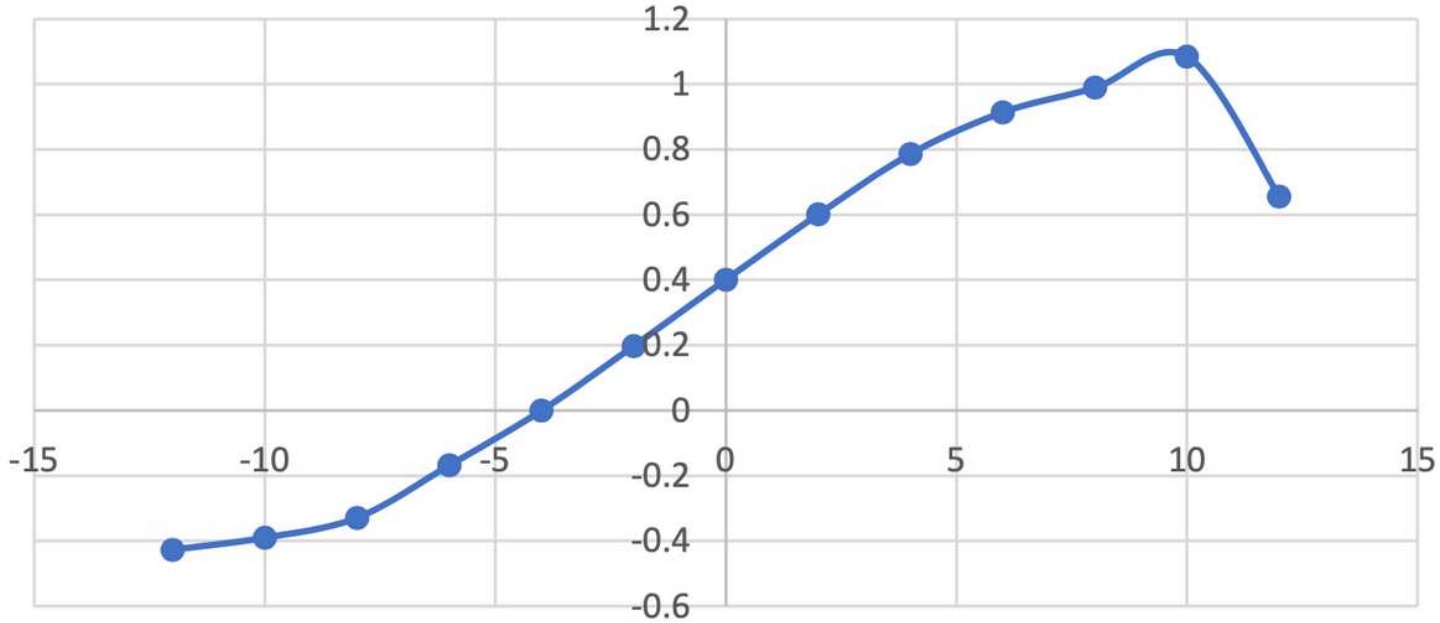

Figure 4

lift coefficient variations with angle of attack

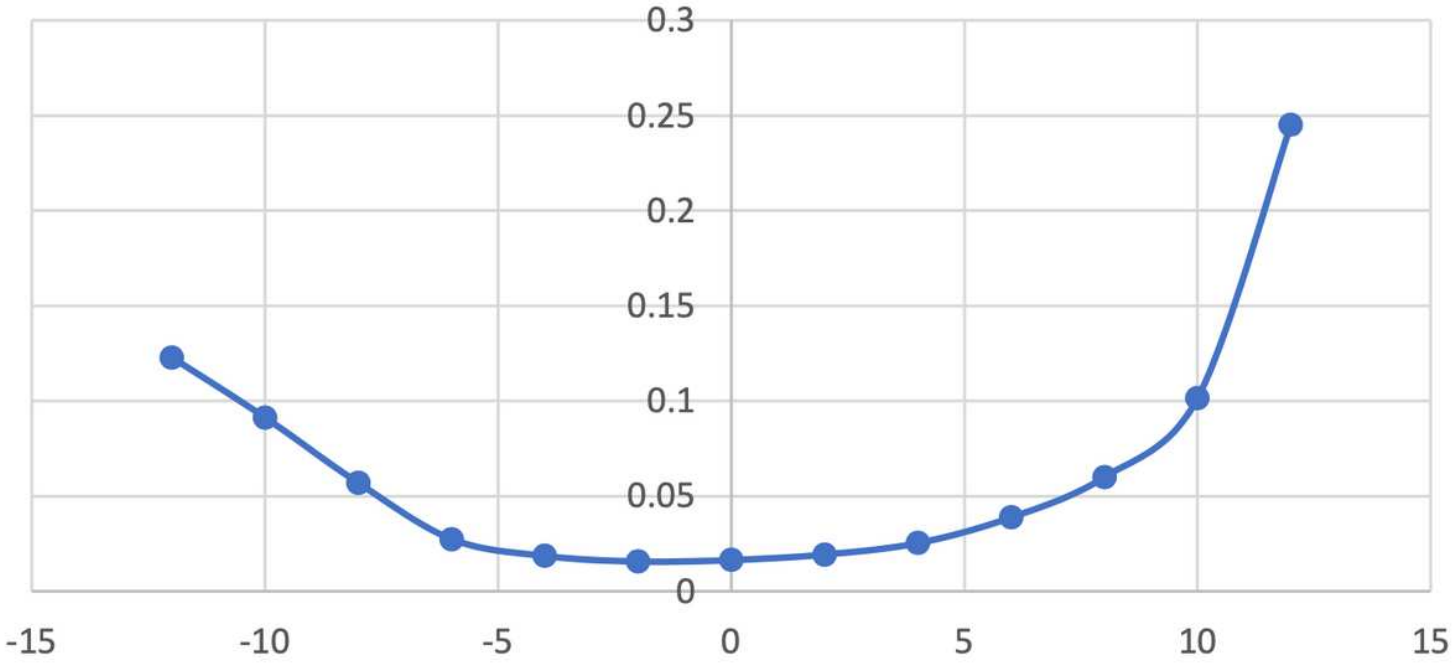

Figure 5

Drag coefficient variations with angle of attack

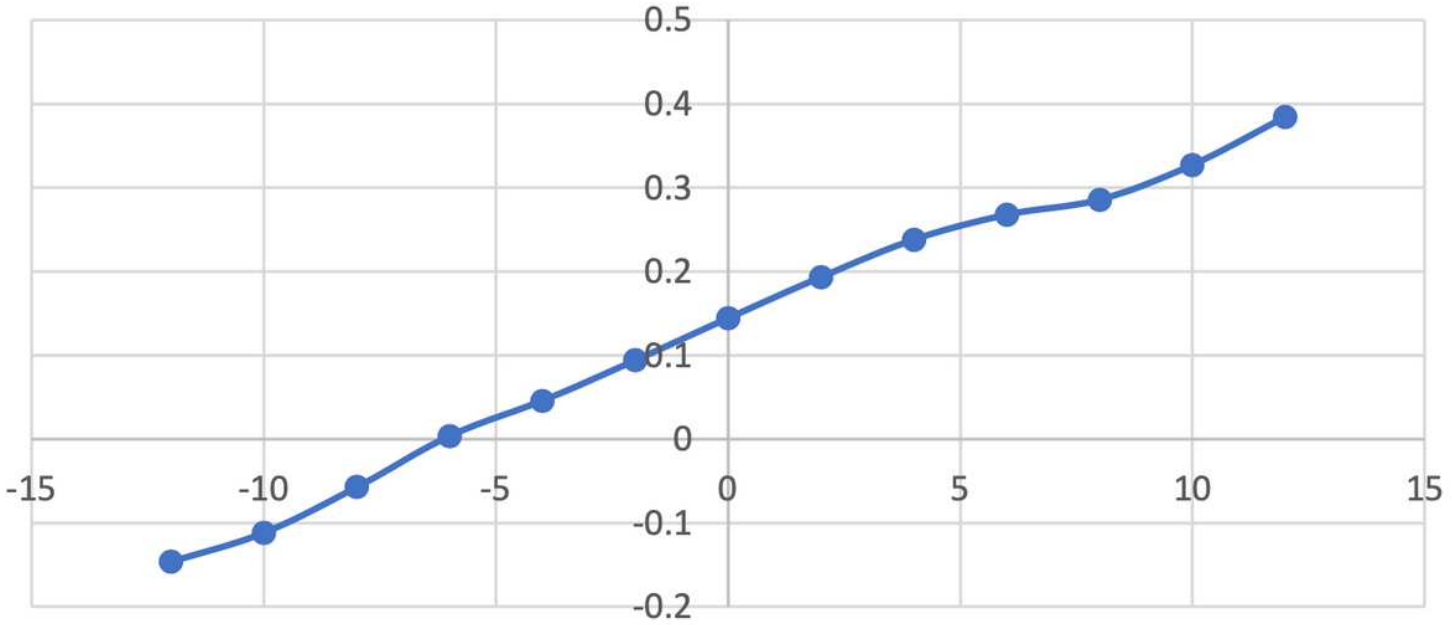

Figure 6

moment coefficient variations with angle of attack

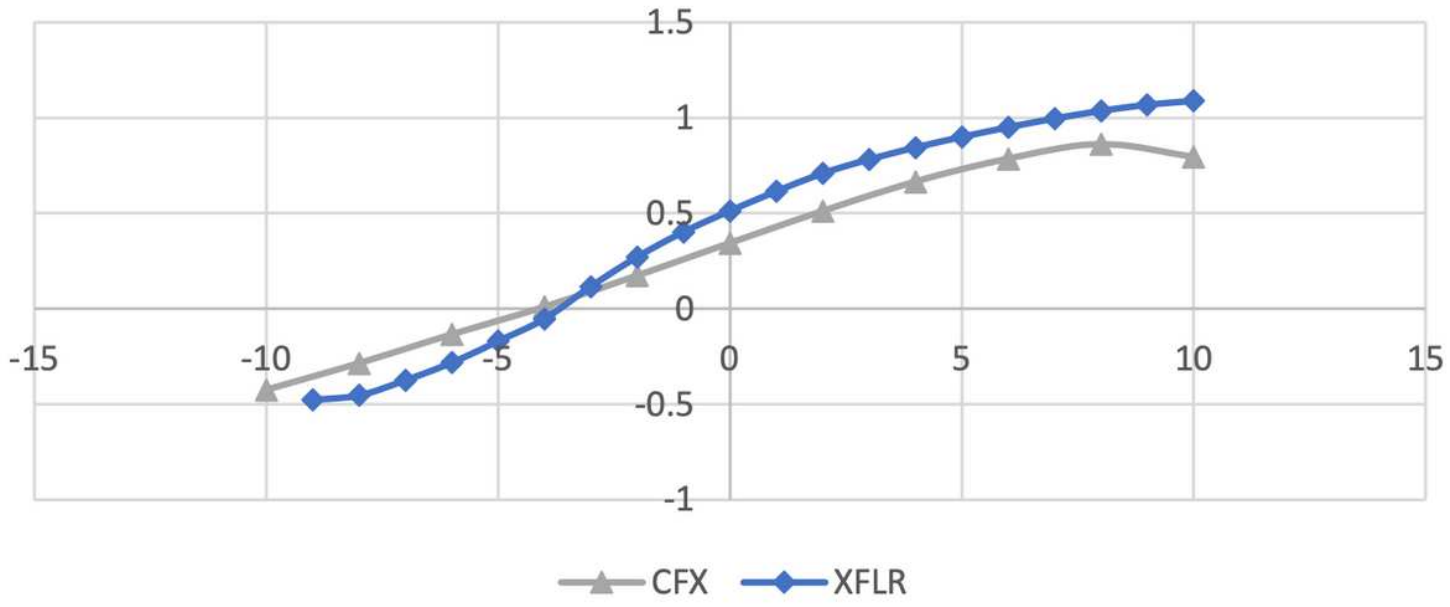

Figure 7

Lift coefficient variations with angle of attack for CFD and XFLR

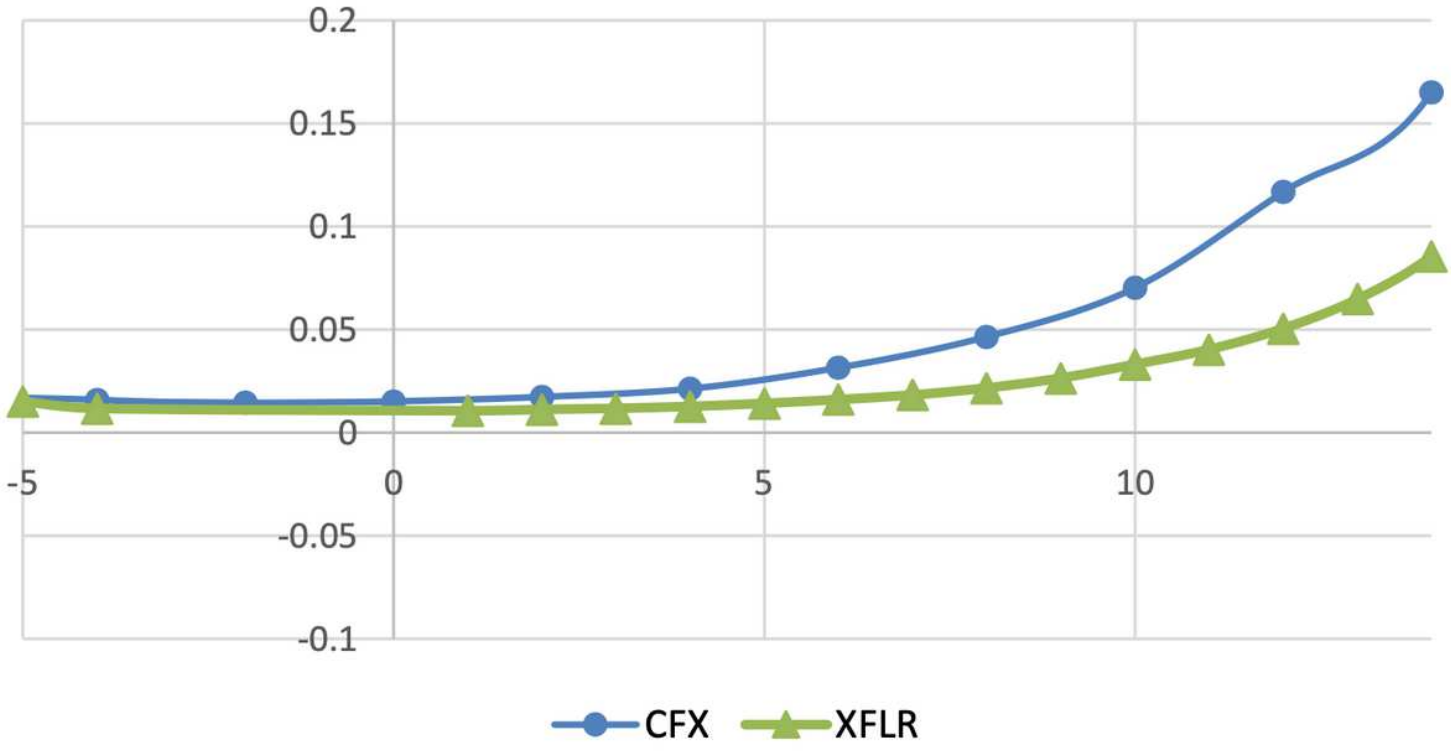

Figure 8

Drag coefficient variations with angle of attack for CFD and XFLR

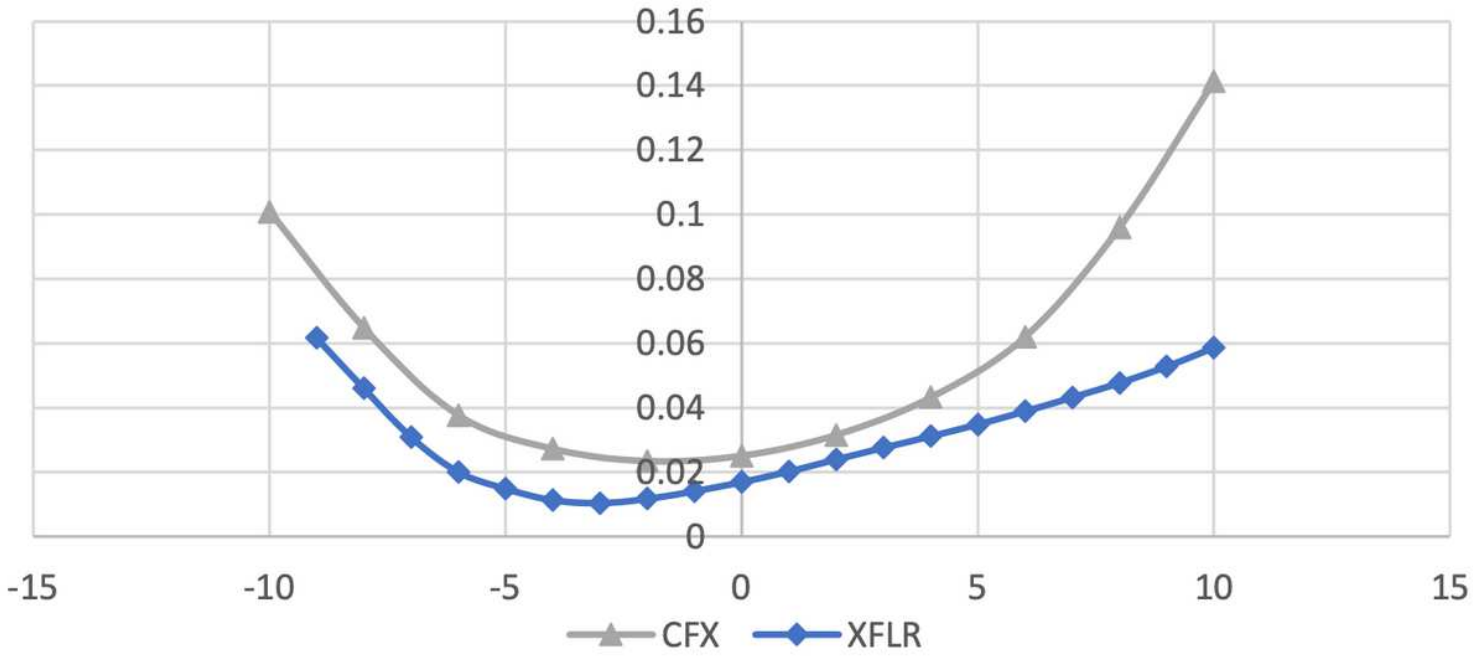

Figure 9

Moment coefficient variations with angle of attack for CFD and XFLR

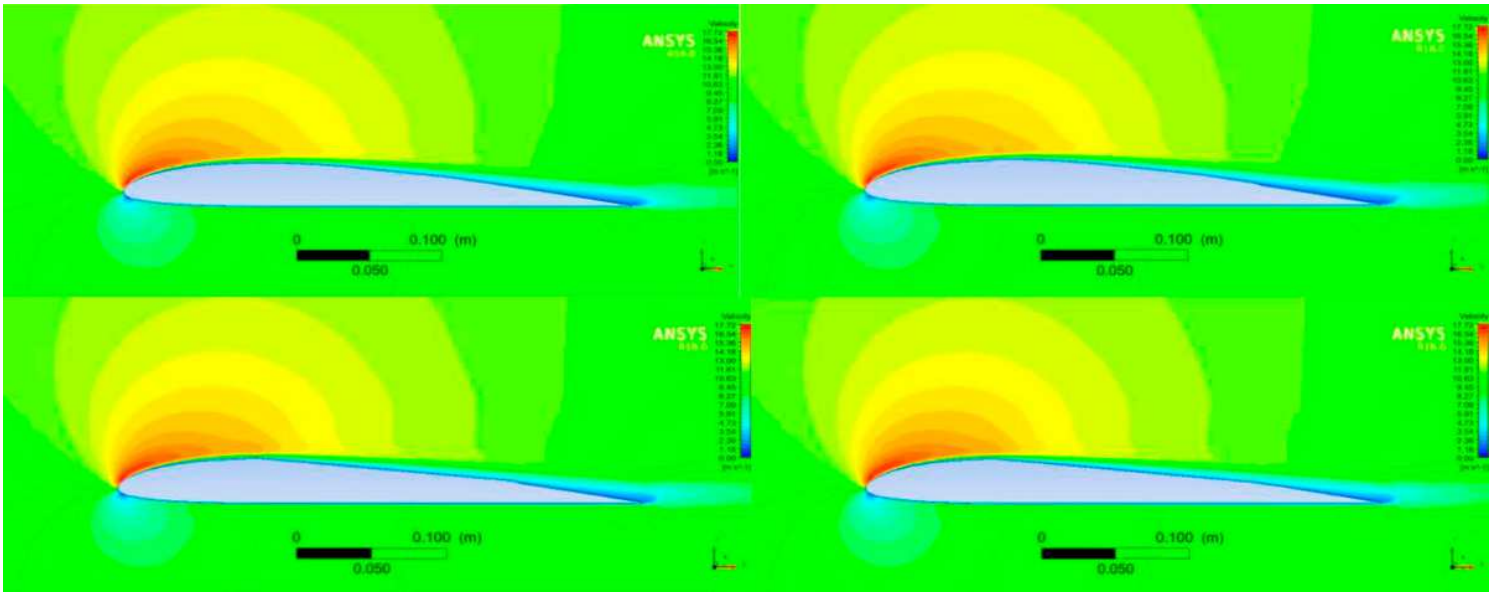

Figure 10

Velocity contour around airfoil AG34 at 6o angle of attack for the configurations a) clean airfoil, b) over curved, c) over flat, and d) submerged flat

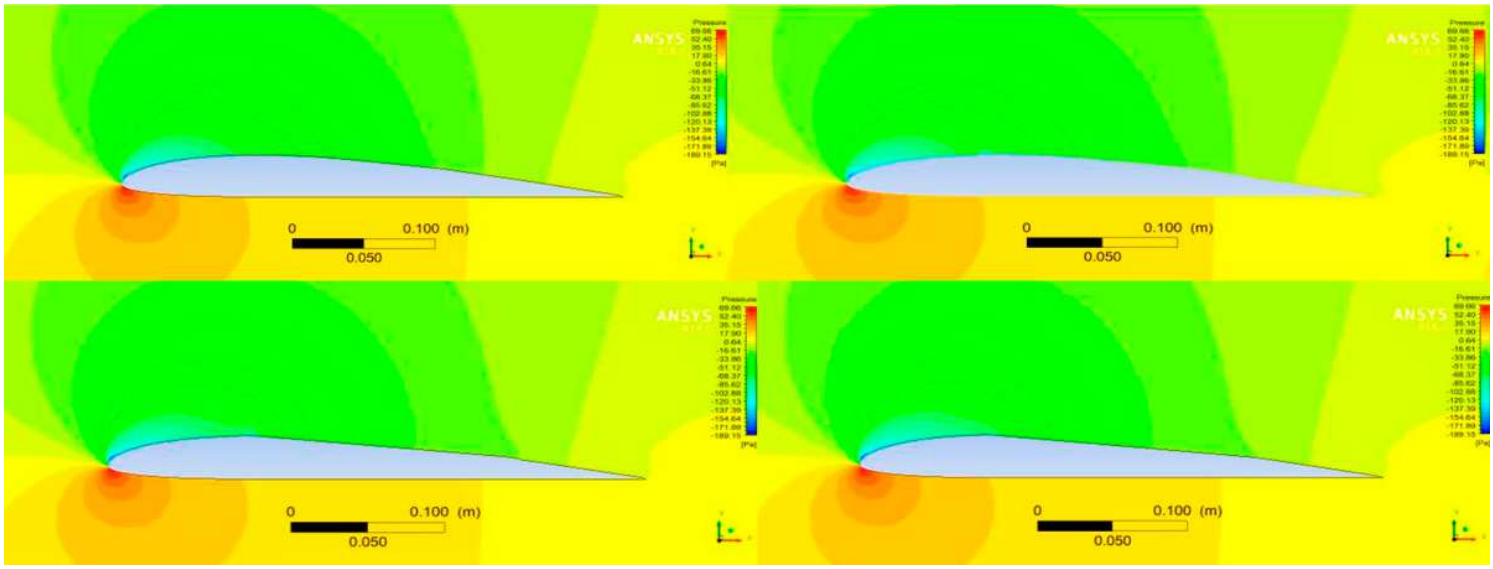

Figure 11

Pressure contour around airfoil AG34 at 6o angle of attack for the configurations a) clean airfoil, b) over curved, c) over flat, and d) submerged flat

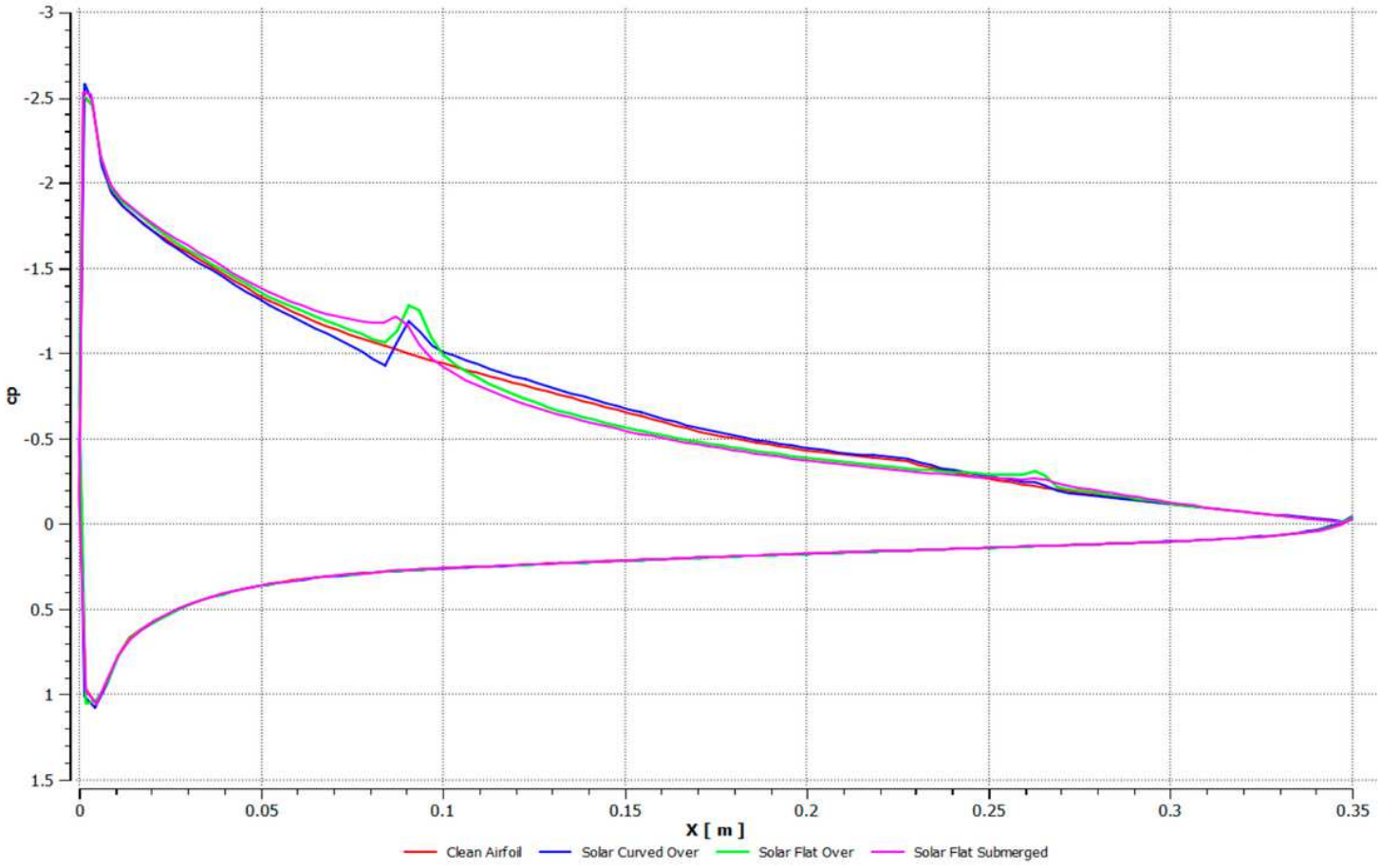

Figure 12

Pressure coefficient distribution over the different airfoil configurations

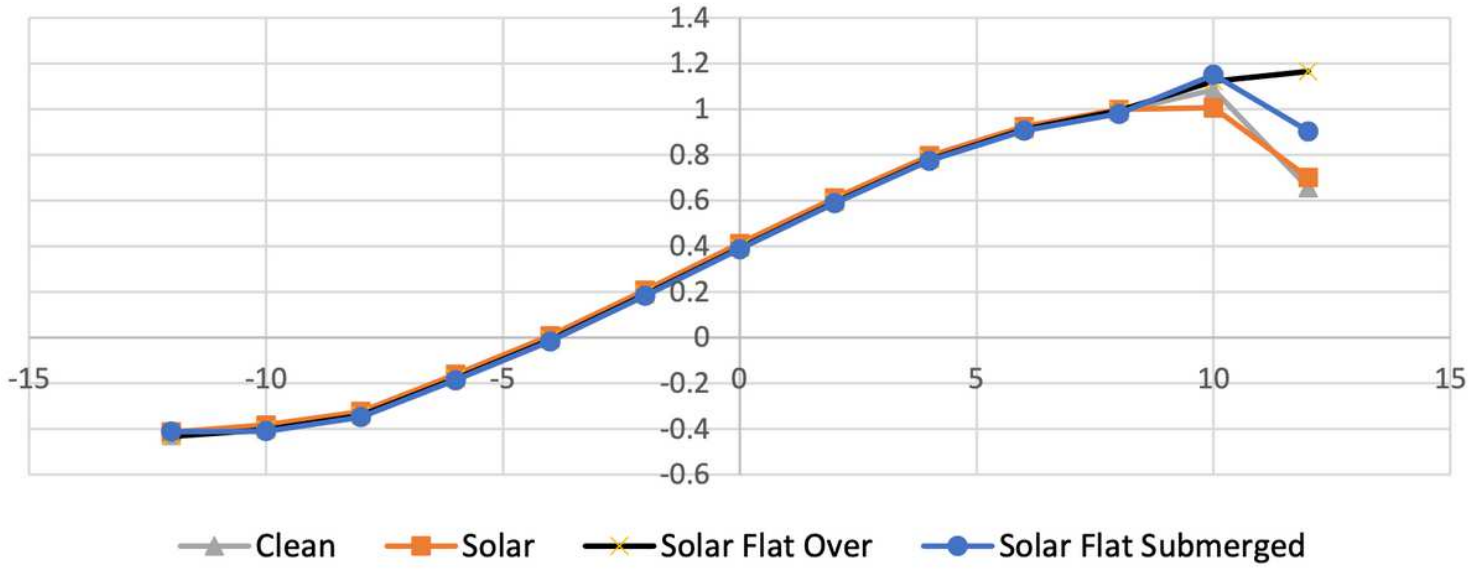

Figure 13

Lift coefficient VS. angle of attack for the different airfoil configurations

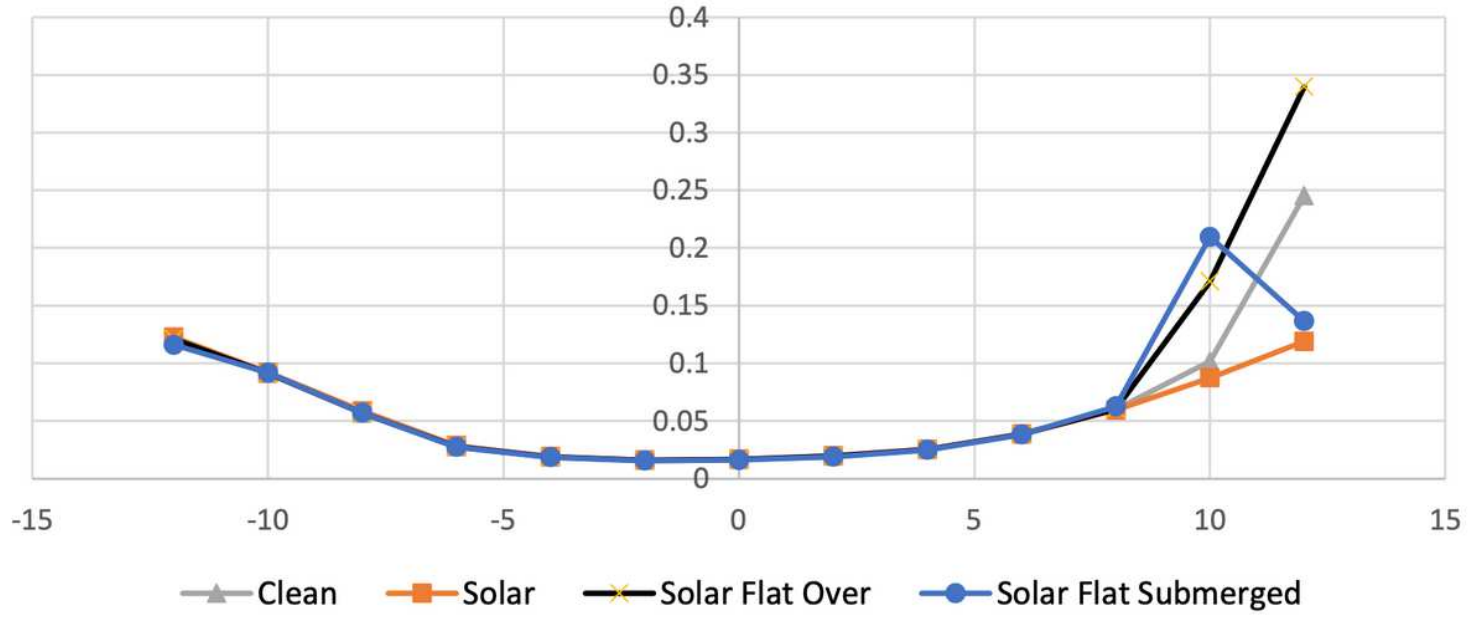

Figure 14

Drag coefficient VS. angle of attack for the different airfoil configurations

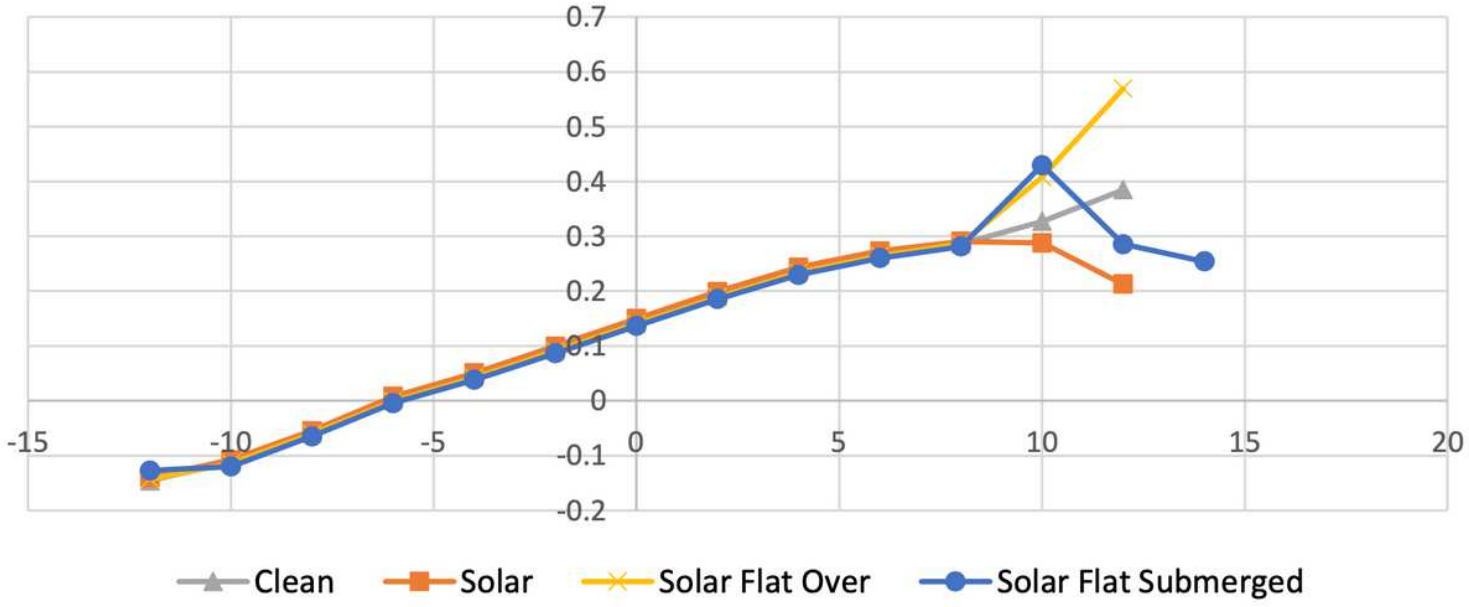

Figure 15

Moment coefficient VS. angle of attack for the different airfoil configurations

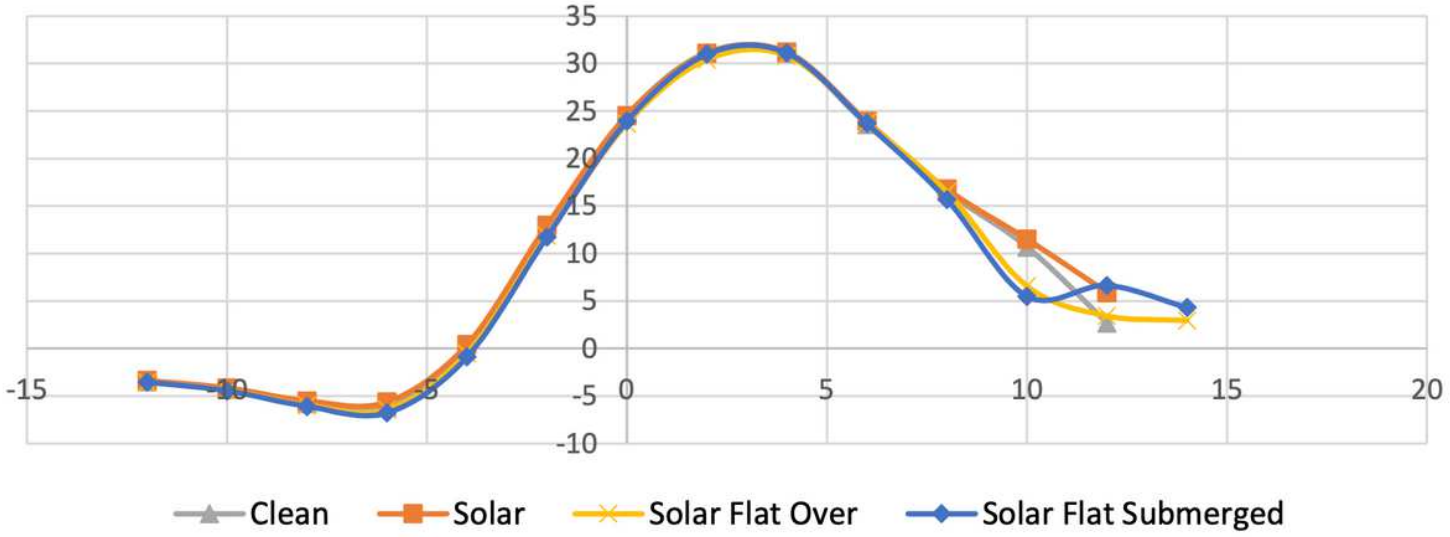

Figure 16

Lift to drag ratio VS. angle of attack for the different airfoil configurations

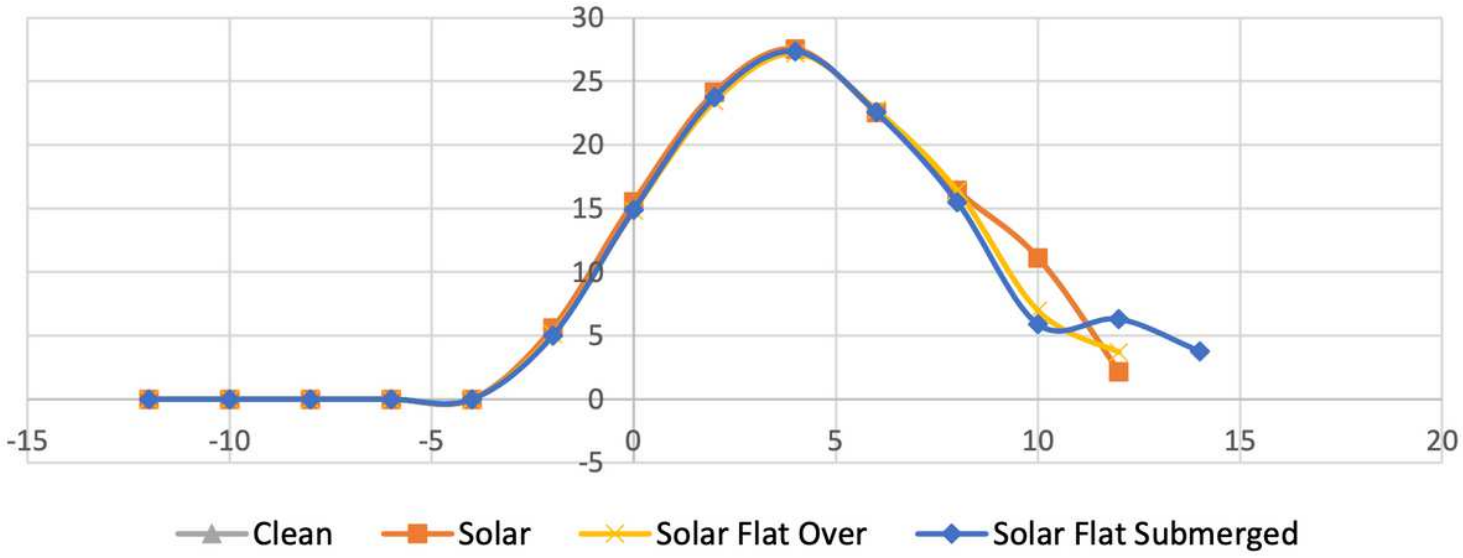

Figure 17

CL3/2/CD VS. angle of attack for the different airfoil configurations

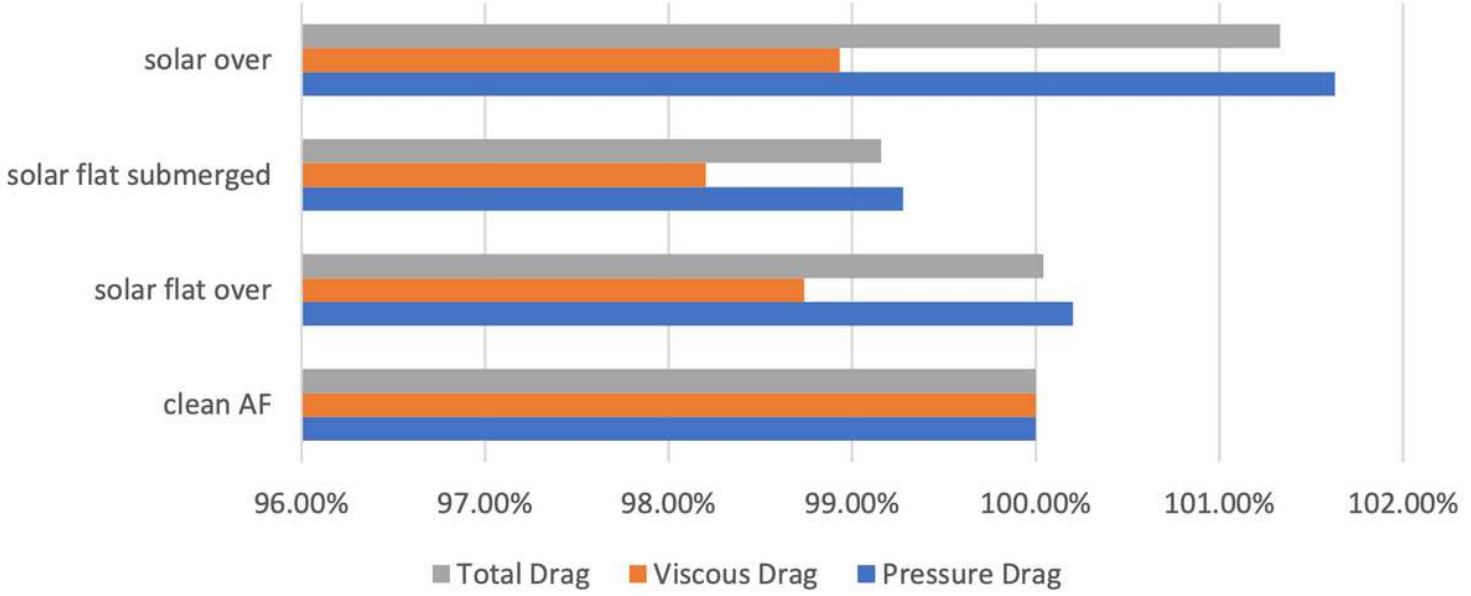

Figure 18

Drag decomposition at AOA 6 degrees for the different airfoil configurations

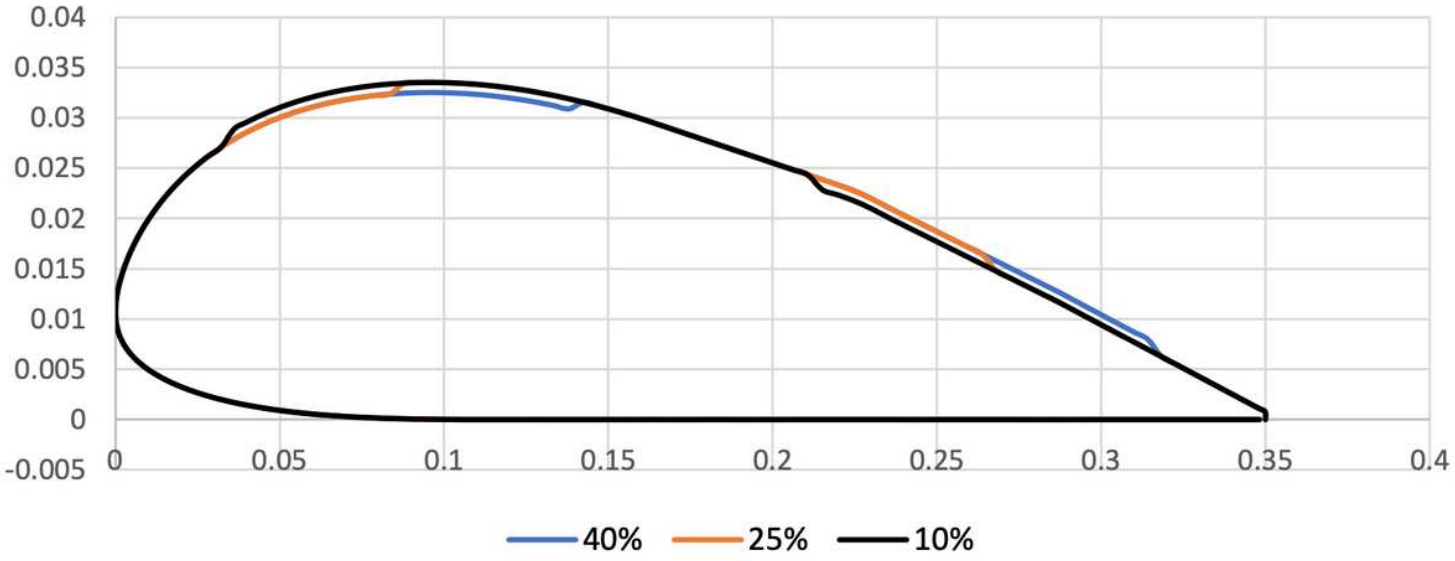

Figure 19

Studied Airfoil Configurations for different panel positions

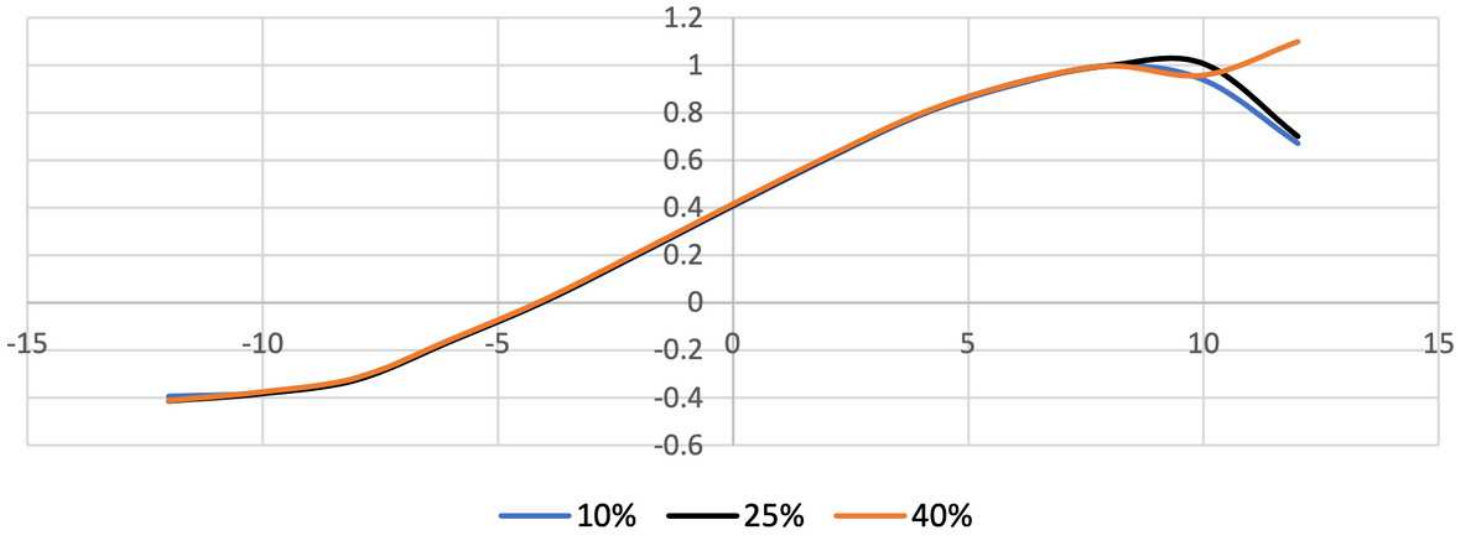

Figure 20

Lift coefficient VS. angle of attack for the different panel positions

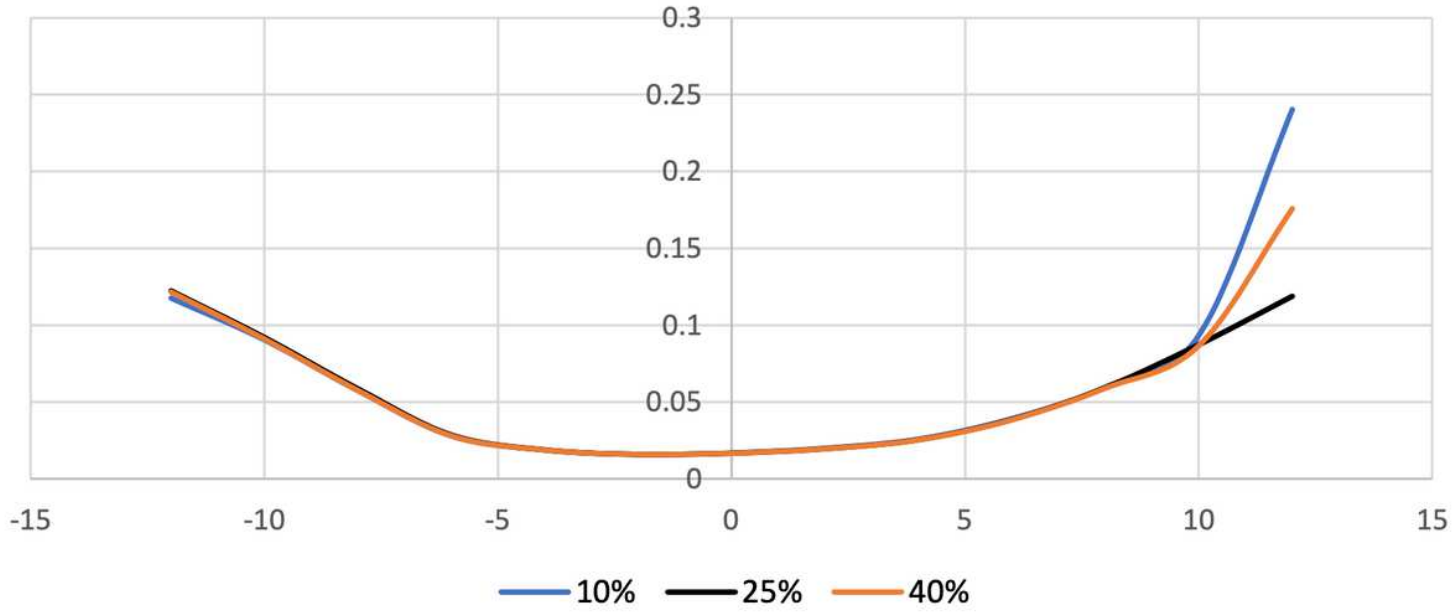

Figure 21

Drag coefficient VS. angle of attack for the different panel positions

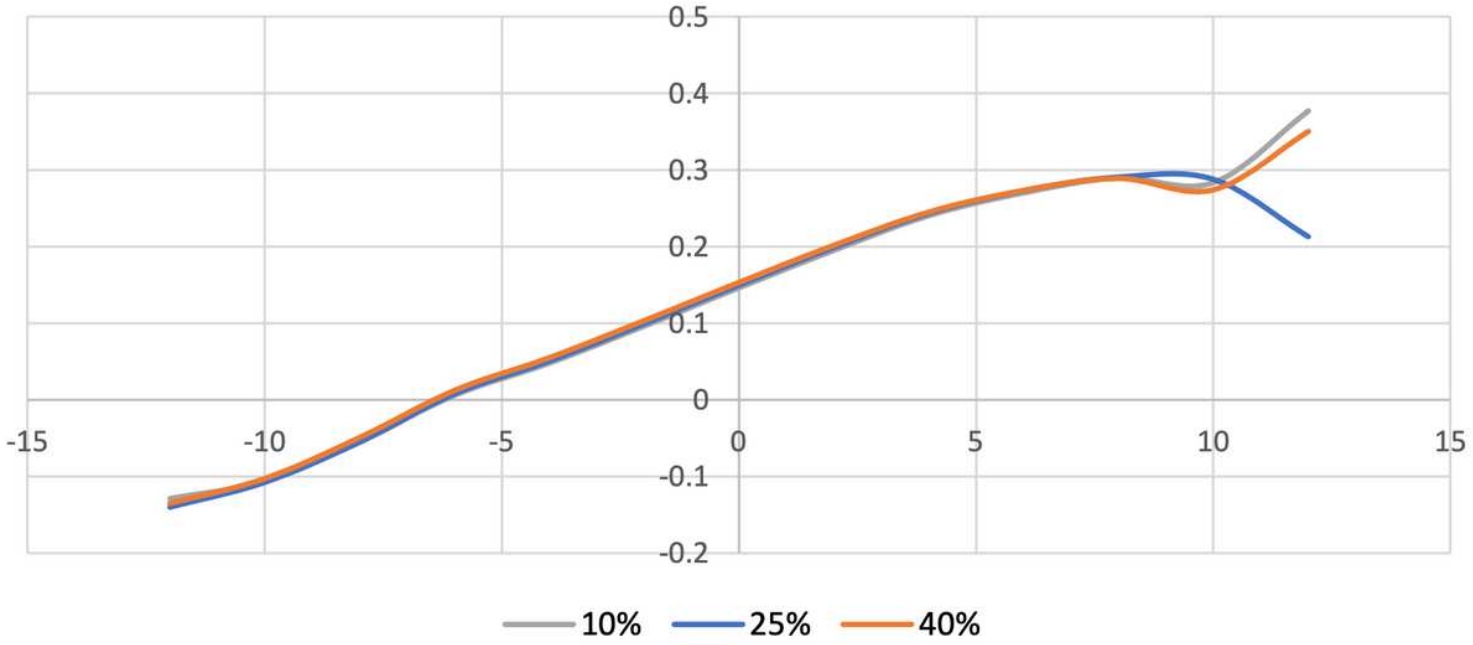

Figure 22

Moment coefficient VS. angle of attack for the different panel positions

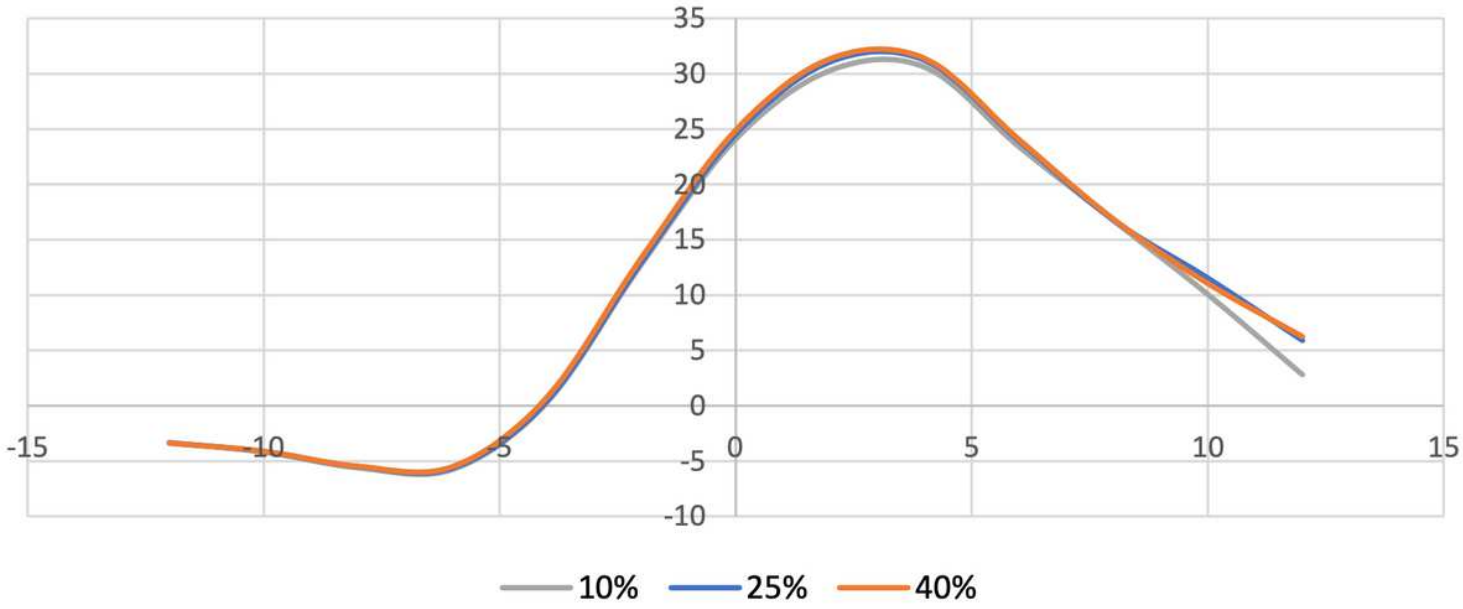

Figure 23

Lift to drag ratio VS. angle of attack for the different panel positions

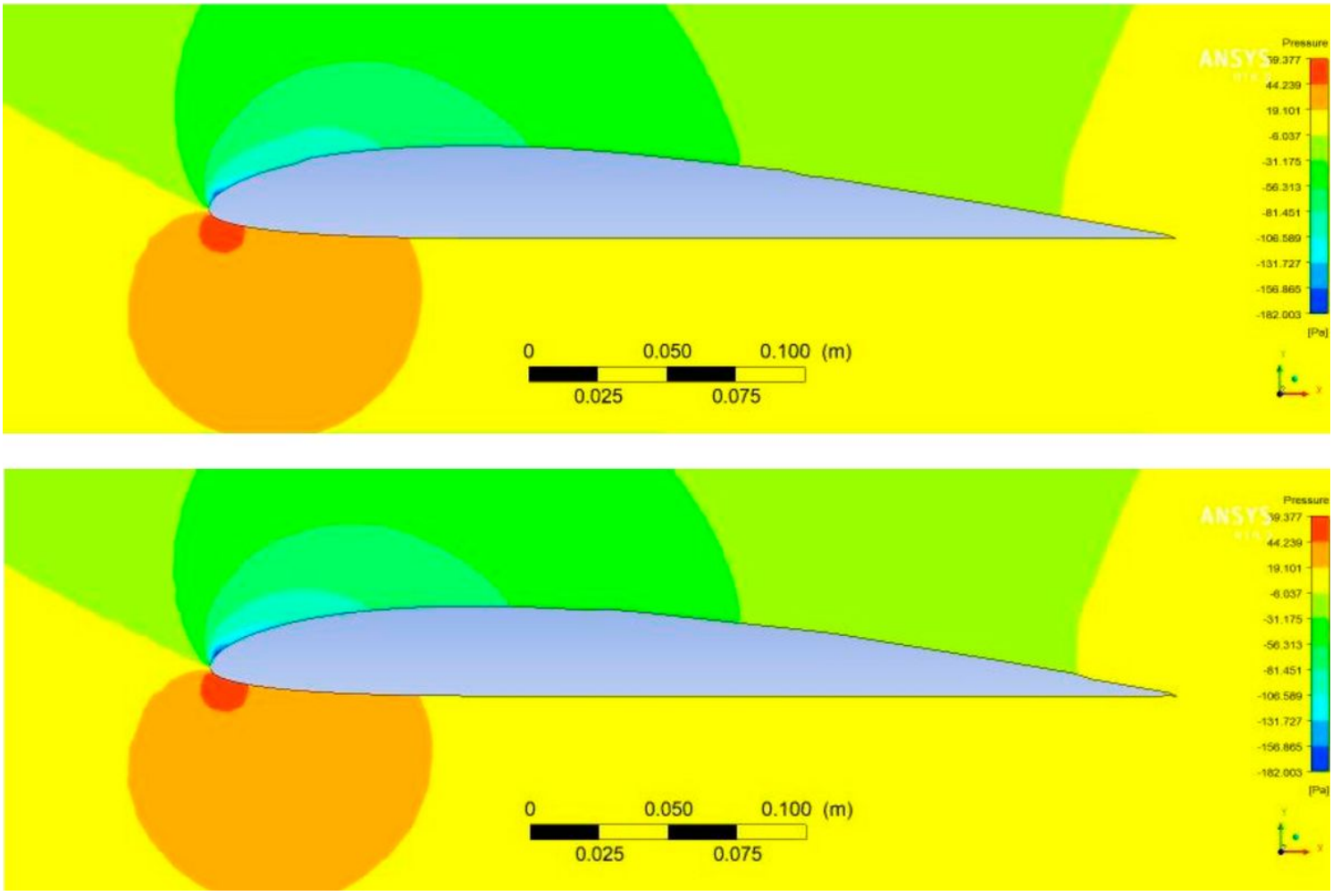

Figure 25

Pressure contour around airfoil AG34 at 6o angle of attack for the configurations a) cell starts at 10%, and b) cell starts at 40%

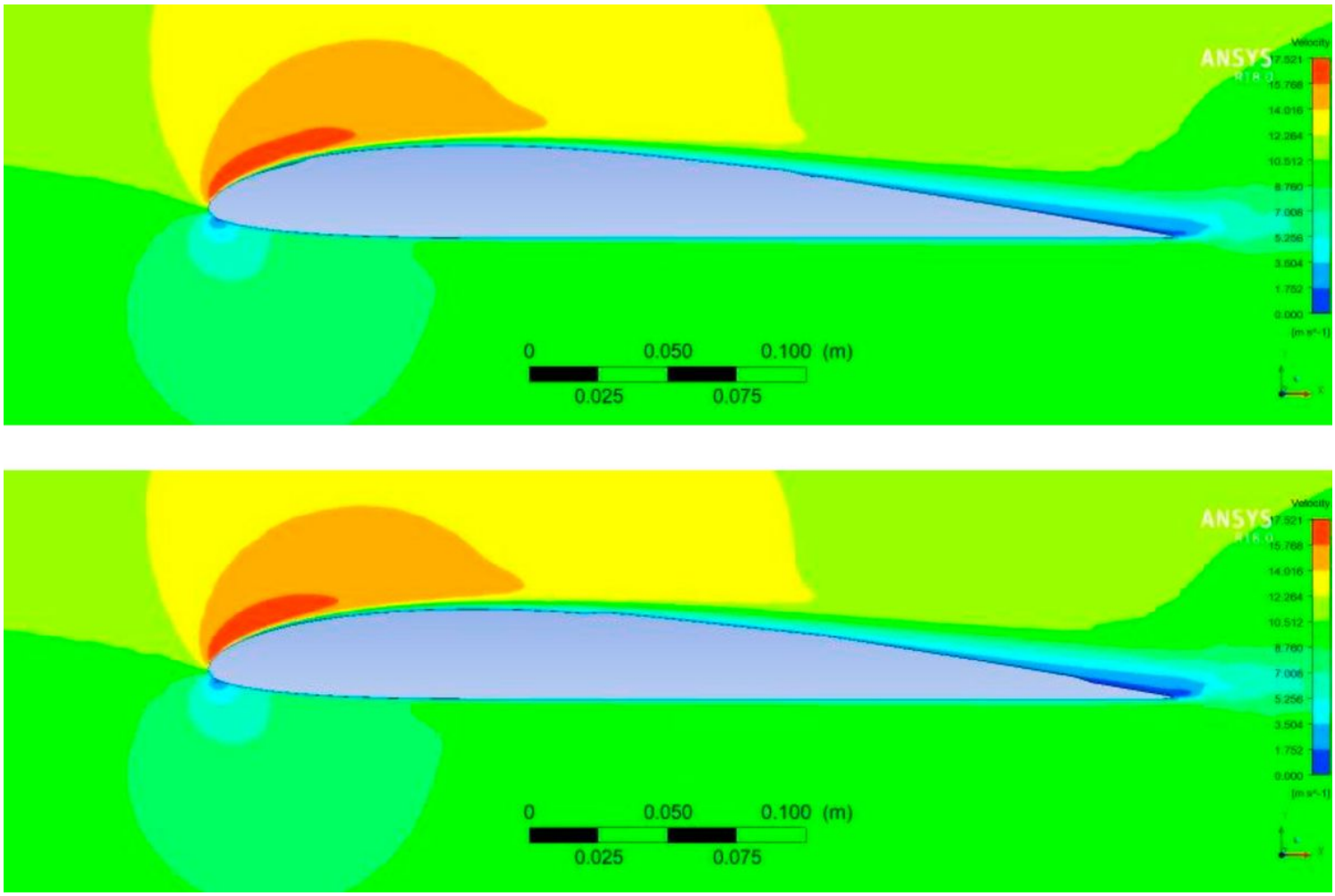

Figure 26

Velocity contour around airfoil AG34 at 6o angle of attack for the configurations a) cell starts at 10%, and b) cell starts at 40%

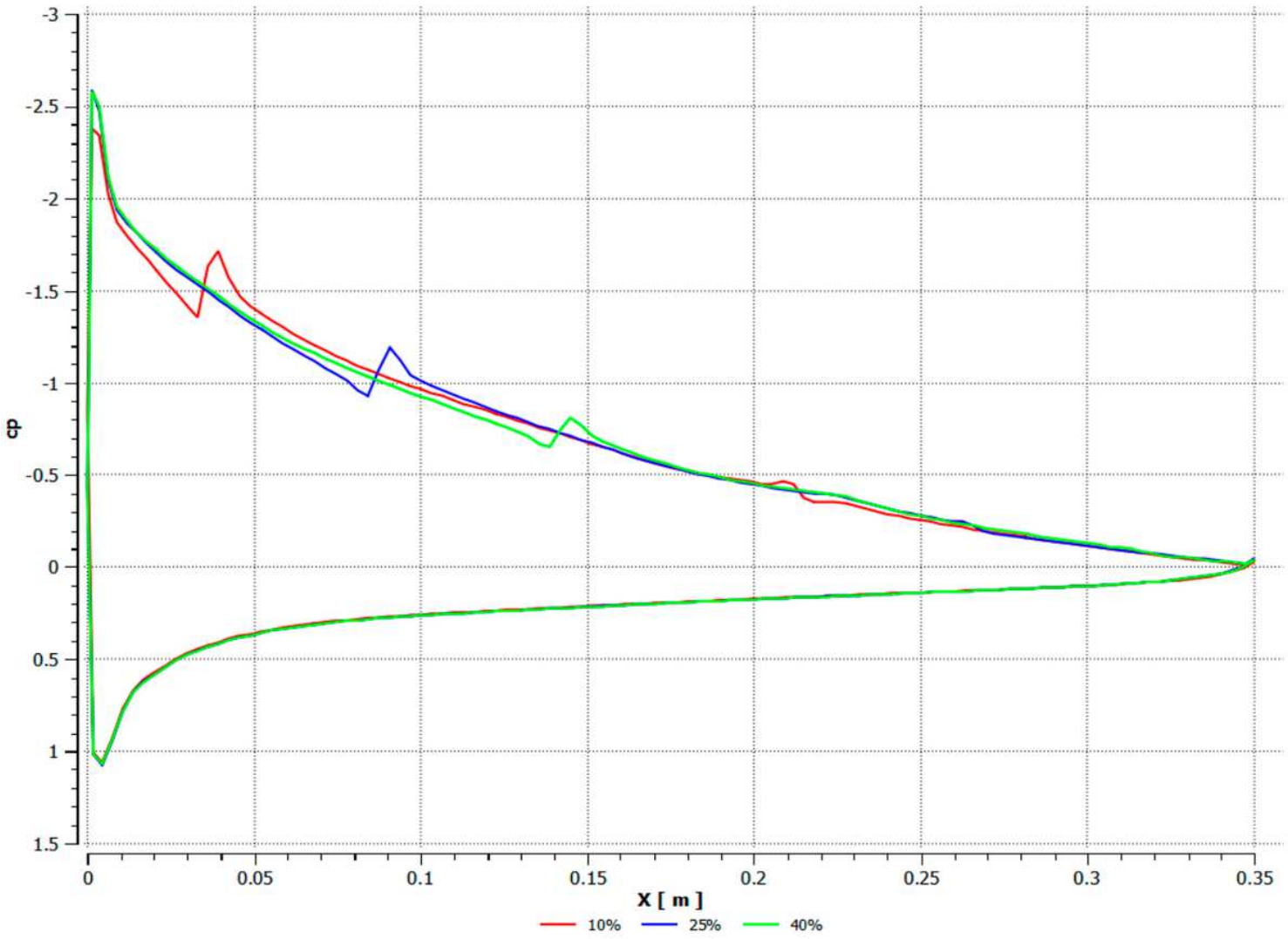

Figure 27

Pressure coefficient distribution over the configurations of different panel positions

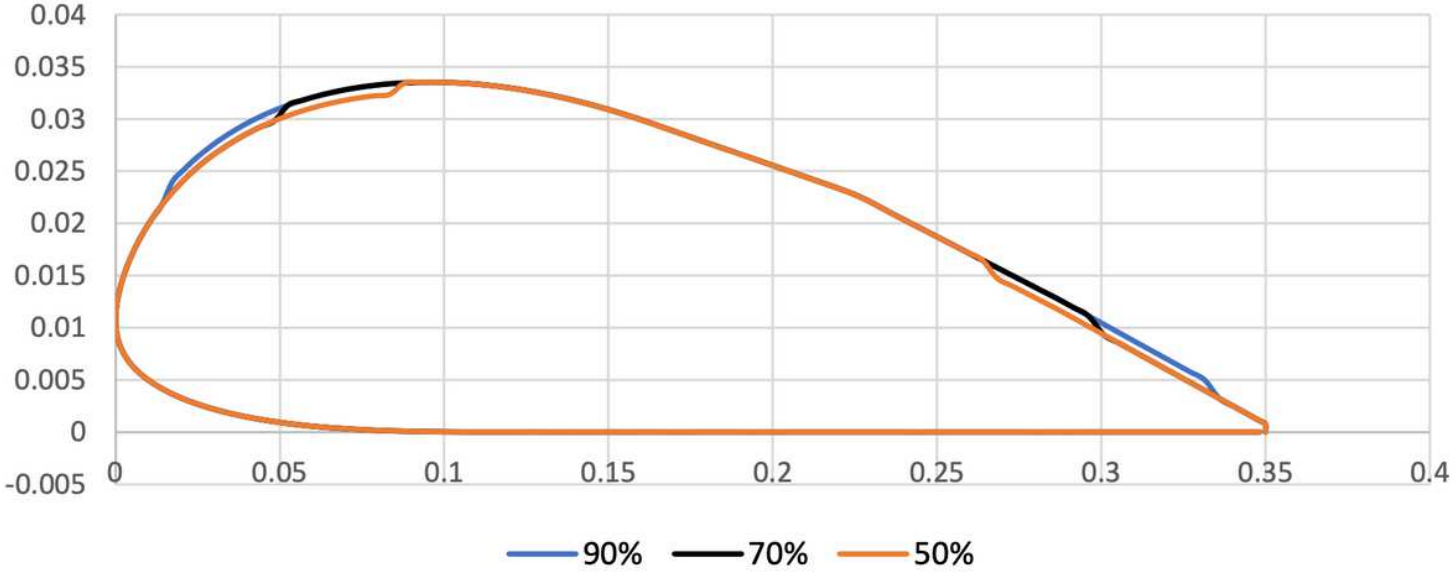

Figure 28

Studied Airfoil Configurations for different panel sizes

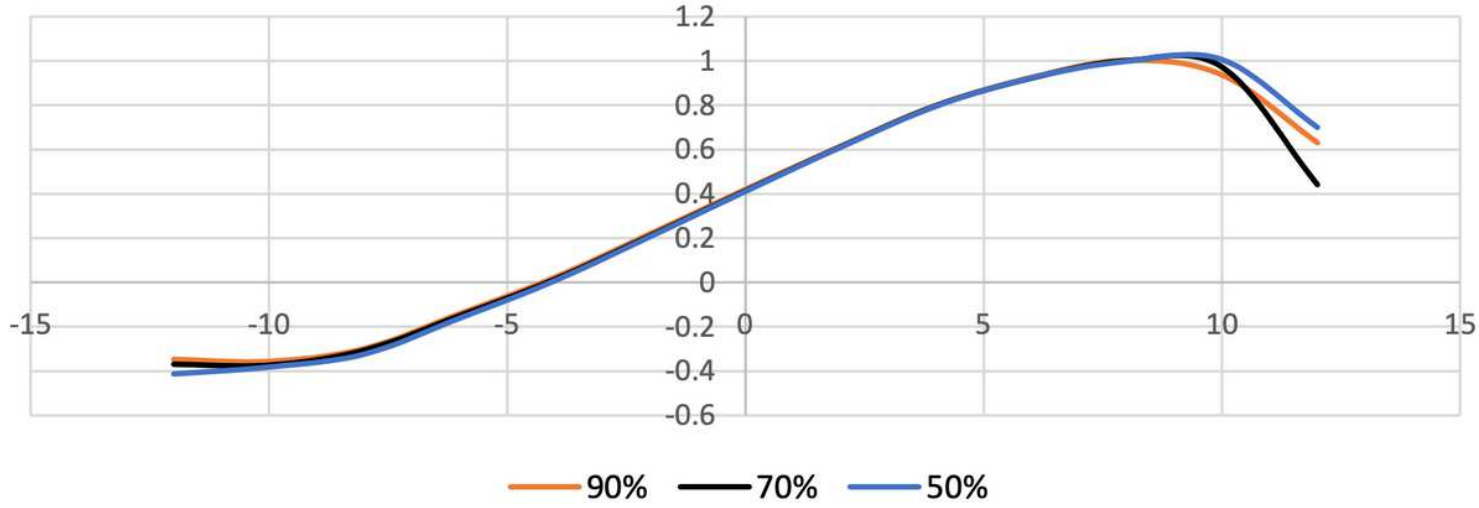

Figure 29

Lift coefficient VS. angle of attack for the different panel sizes

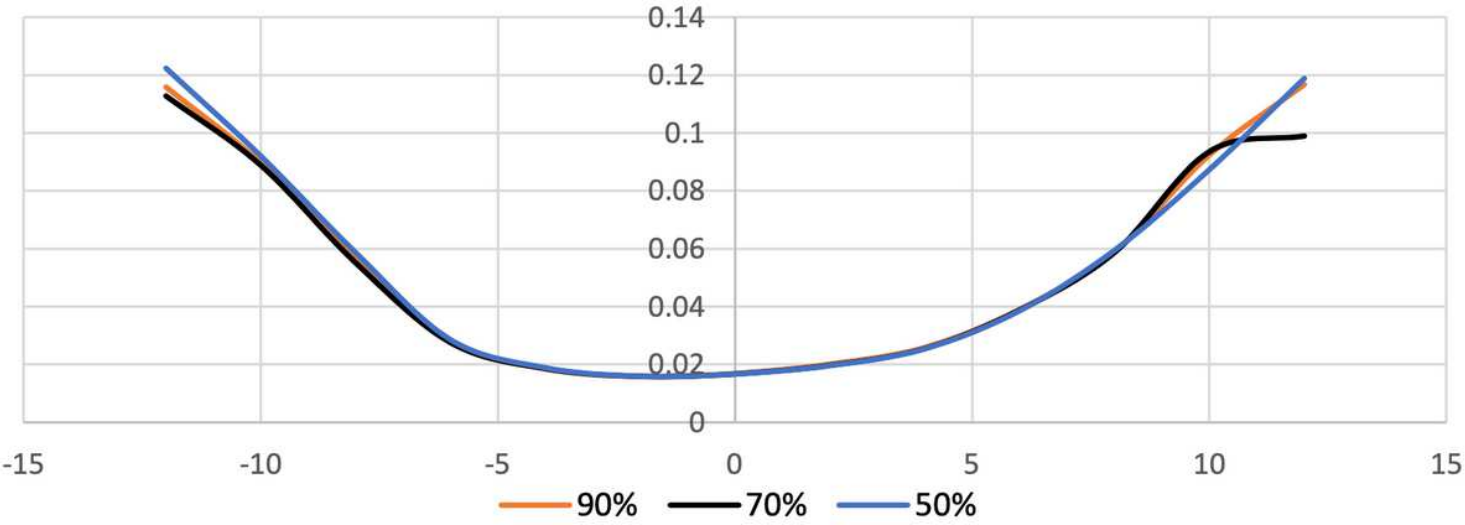

Figure 30

Drag coefficient VS. angle of attack for the different panel sizes

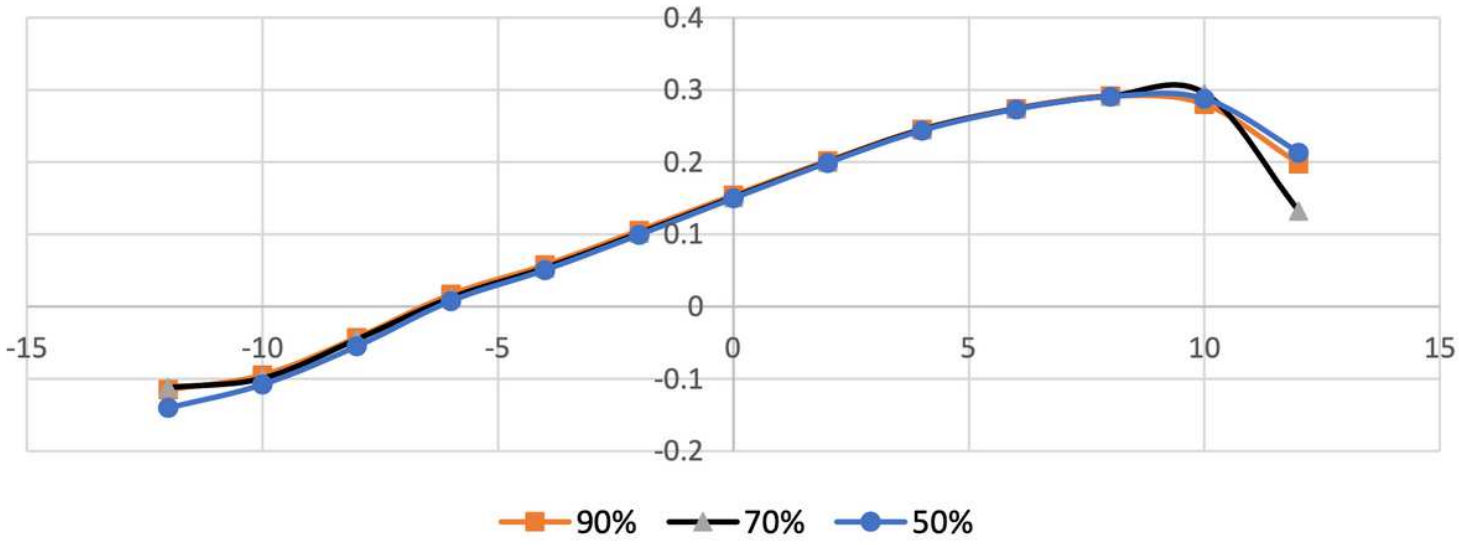

Figure 31

Moment coefficient VS. angle of attack for the different panel sizes

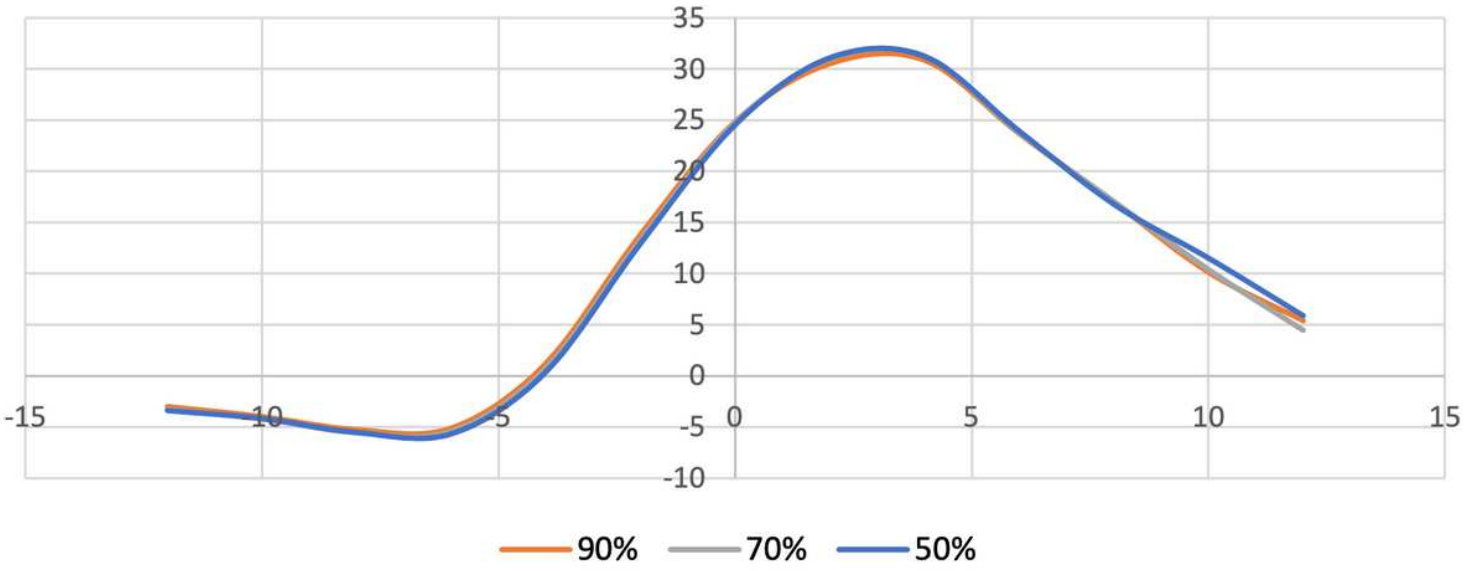

Figure 32

Lift-to-drag ratio coefficient VS. angle of attack for the different panel sizes

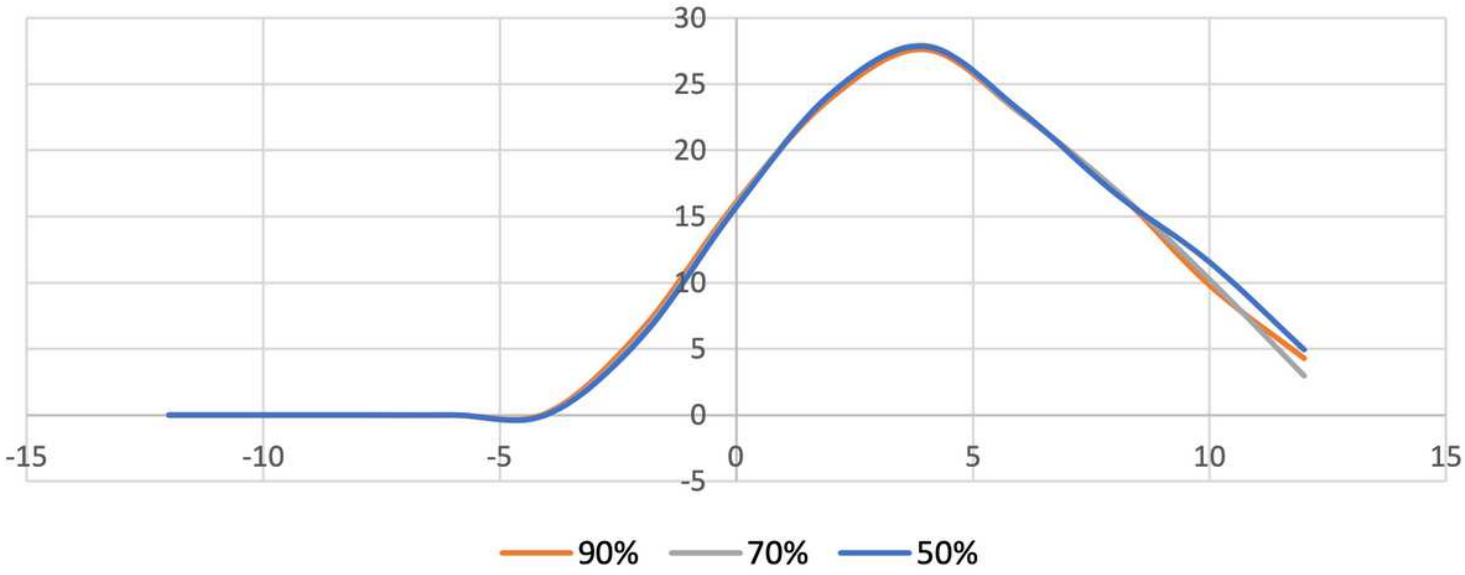

Figure 33

CL3/2/CD VS. angle of attack for the different panel sizes

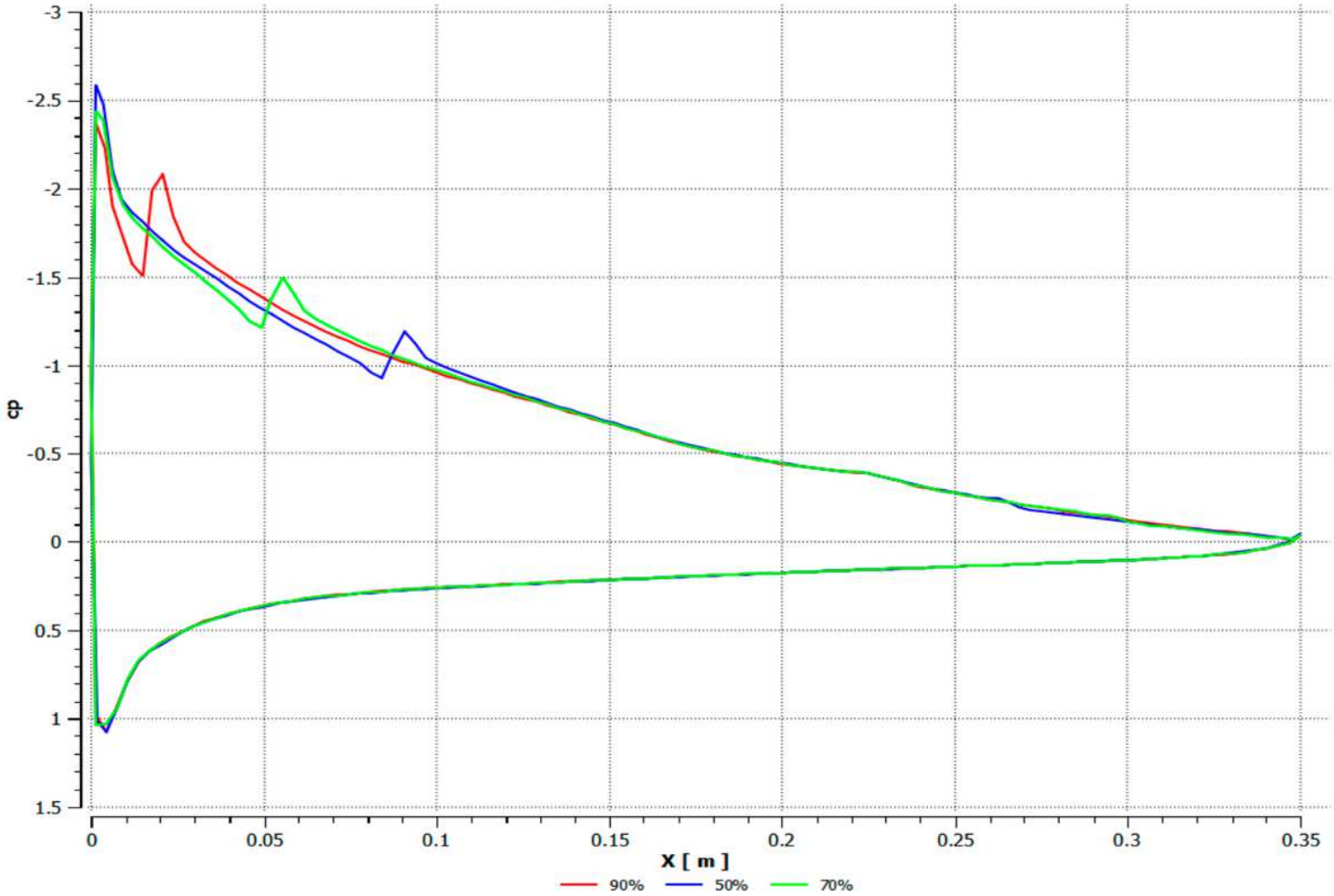

Figure 34

Pressure coefficient distribution over the configurations of different panel sizes

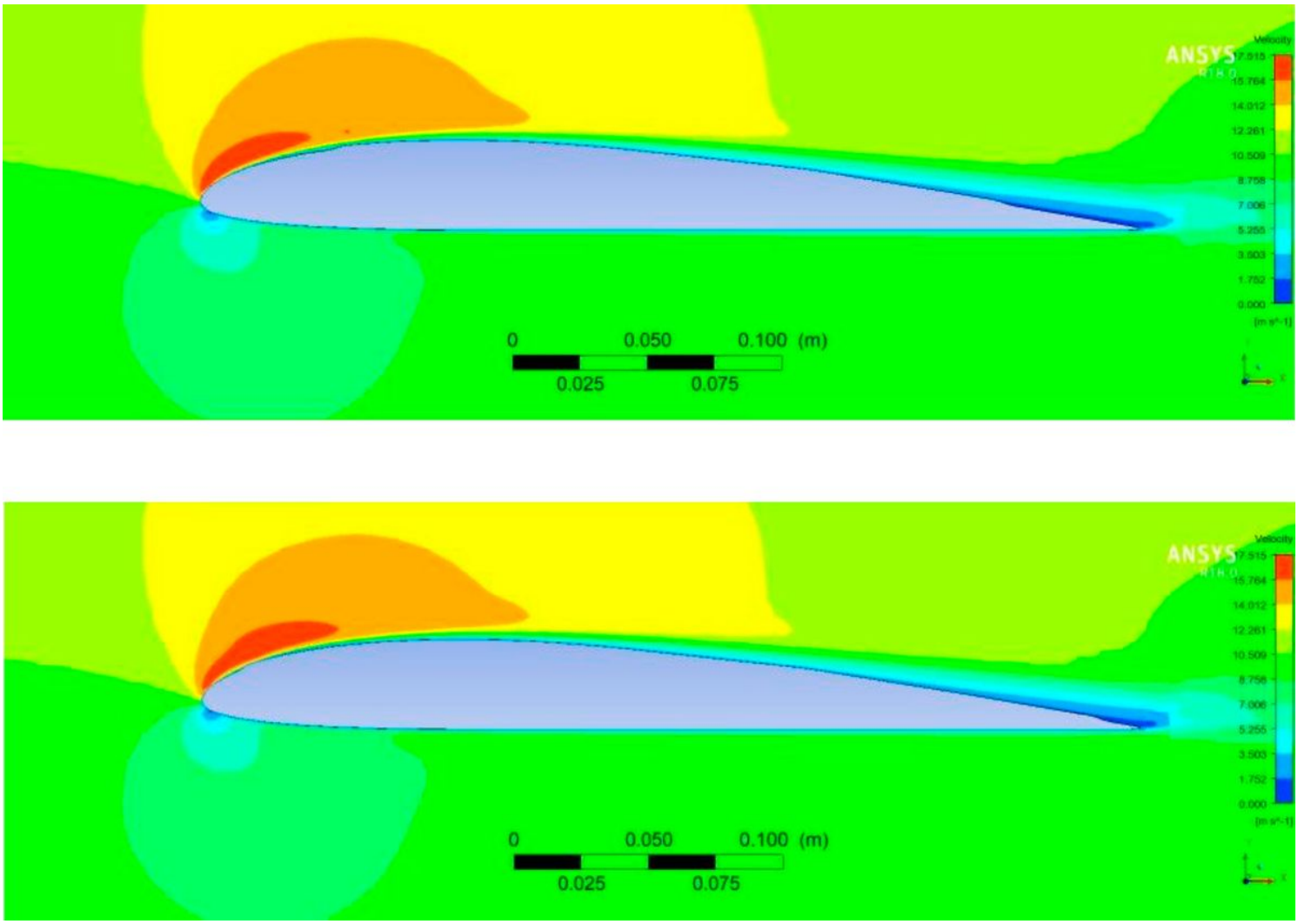

Figure 35

Velocity contour around airfoil AG34 at 6o angle of attack for the configurations a) cell covers 70%, and b) cell covers 90%

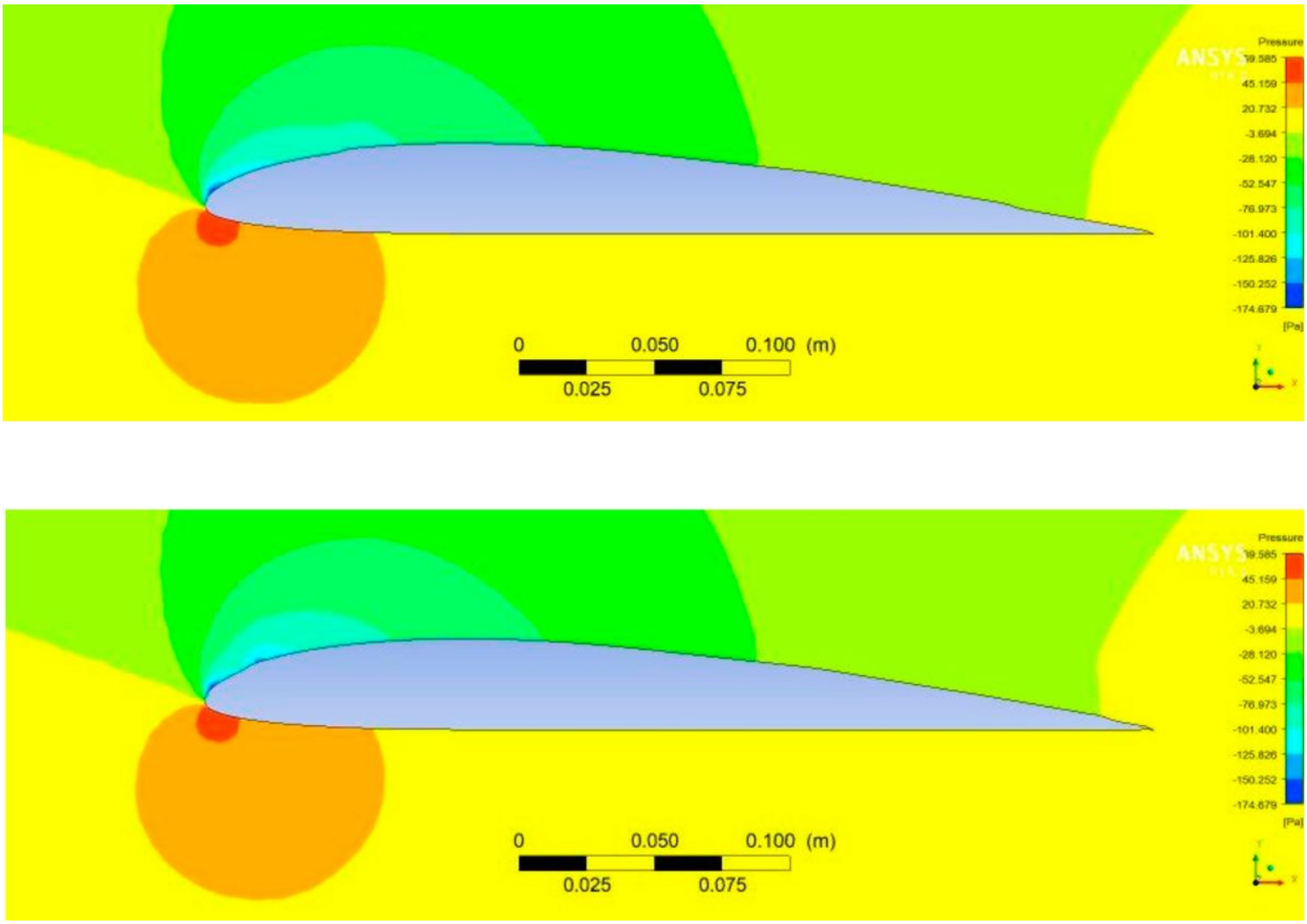

Figure 36

Pressure contour around airfoil AG34 at 6o angle of attack for the configurations a) cell covers 70%, and b) cell covers 90%

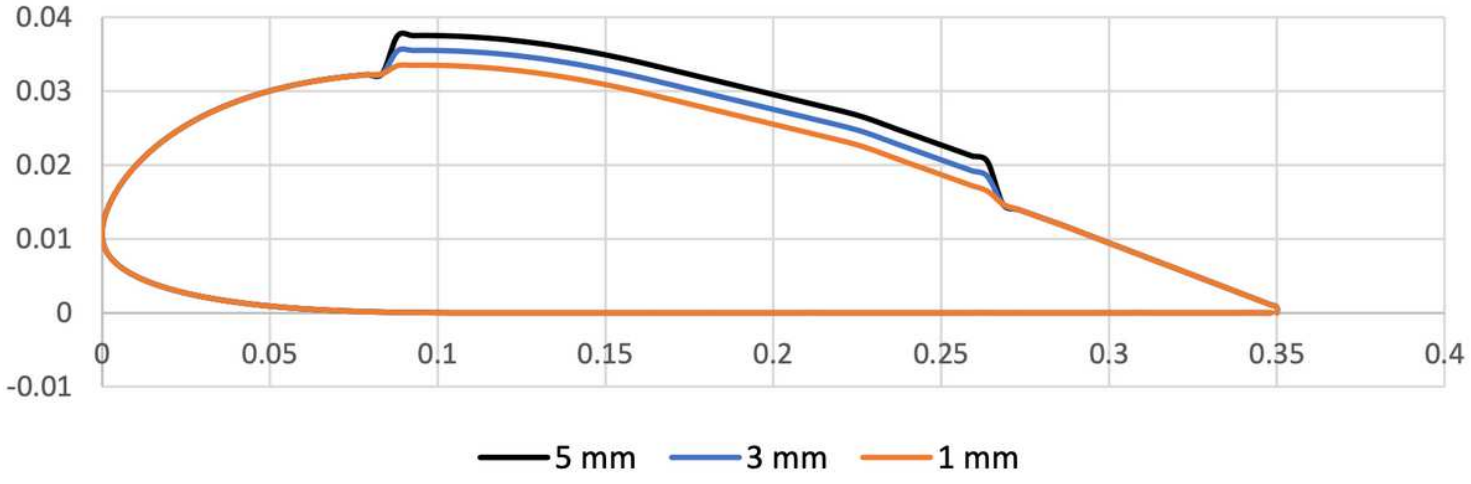

Figure 37

Studied Airfoil Configurations for different panel sessenhttht

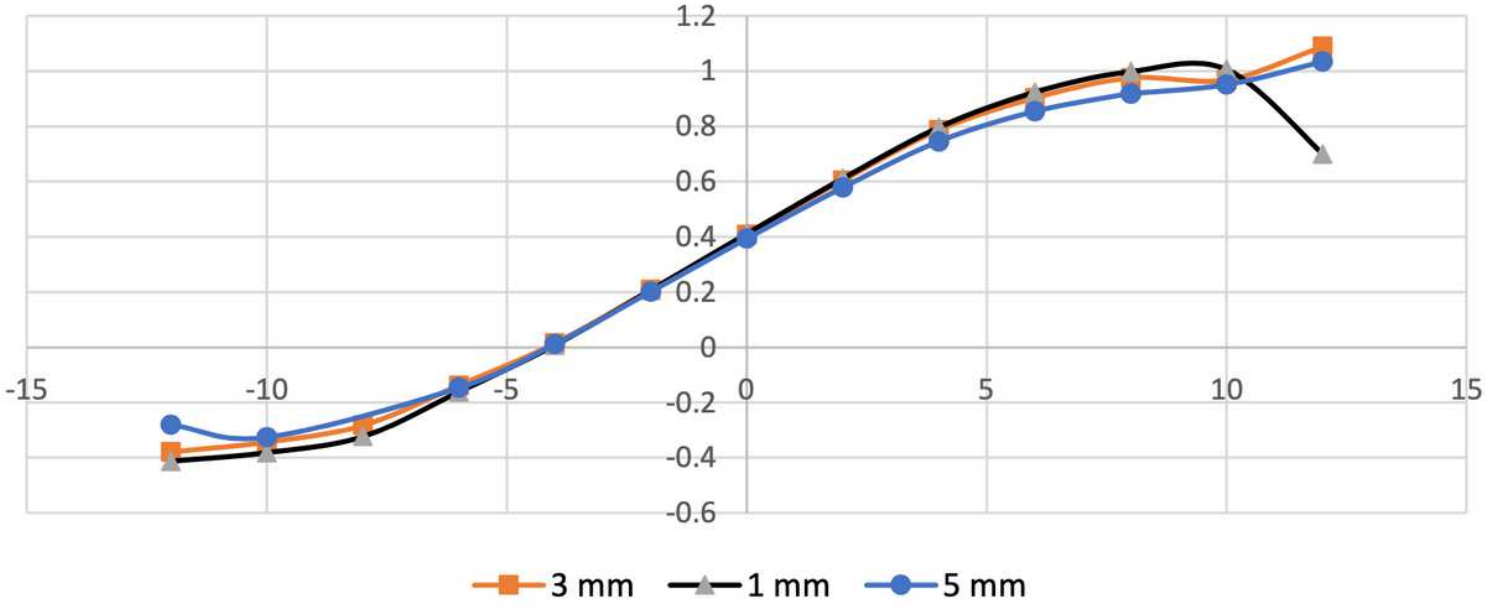

Figure 38

Lift coefficient VS. angle of attack for the different panel sessenhttht

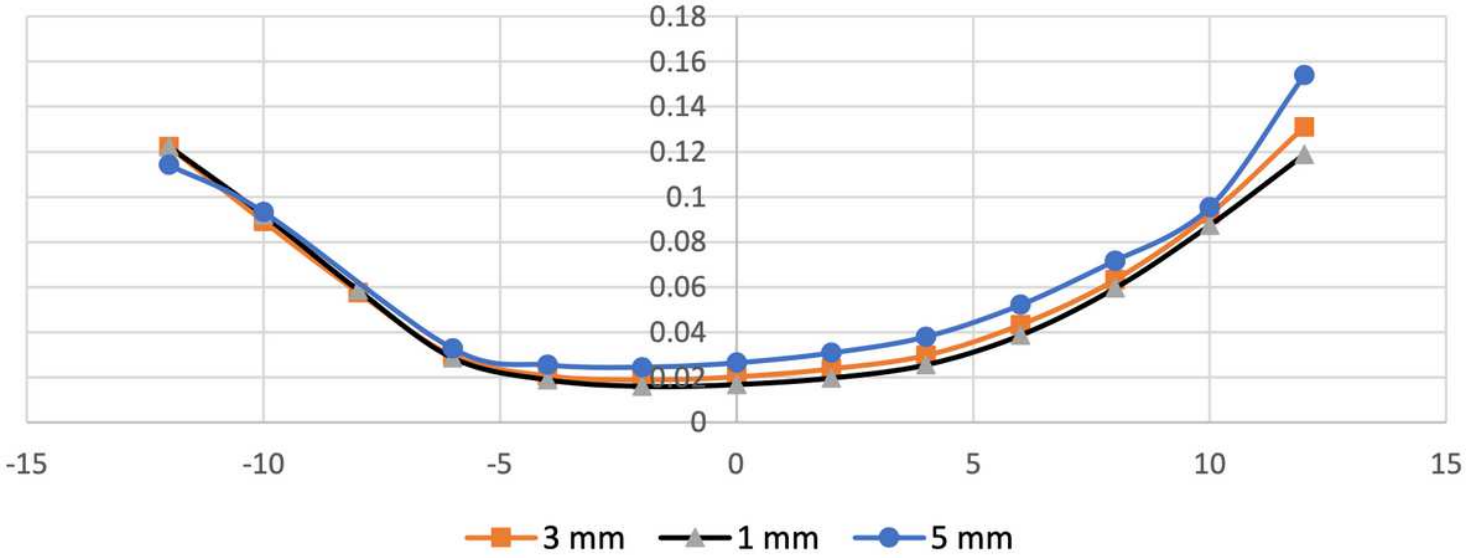

Figure 39

Drag coefficient VS. angle of attack for the different panel thicknesses

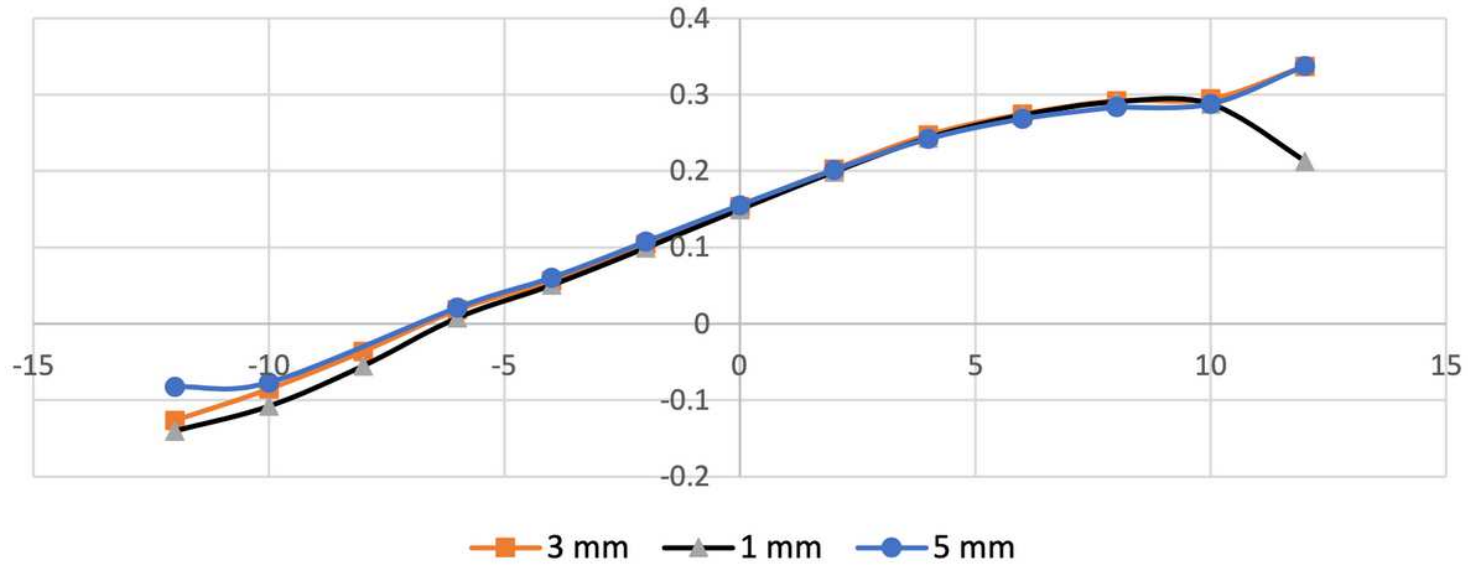

Figure 40

Moment coefficient VS. angle of attack for the different panel thicknesses

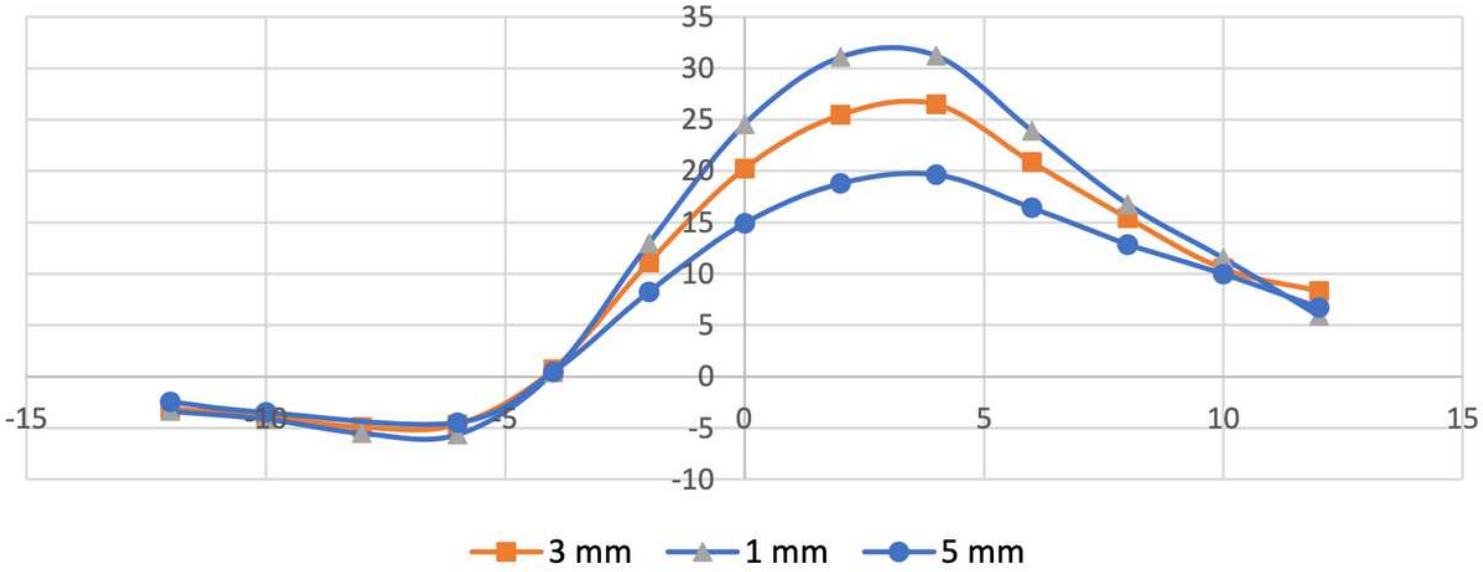

Figure 41

Lift-to-drag ratio VS. angle of attack for the different panel thicknesses

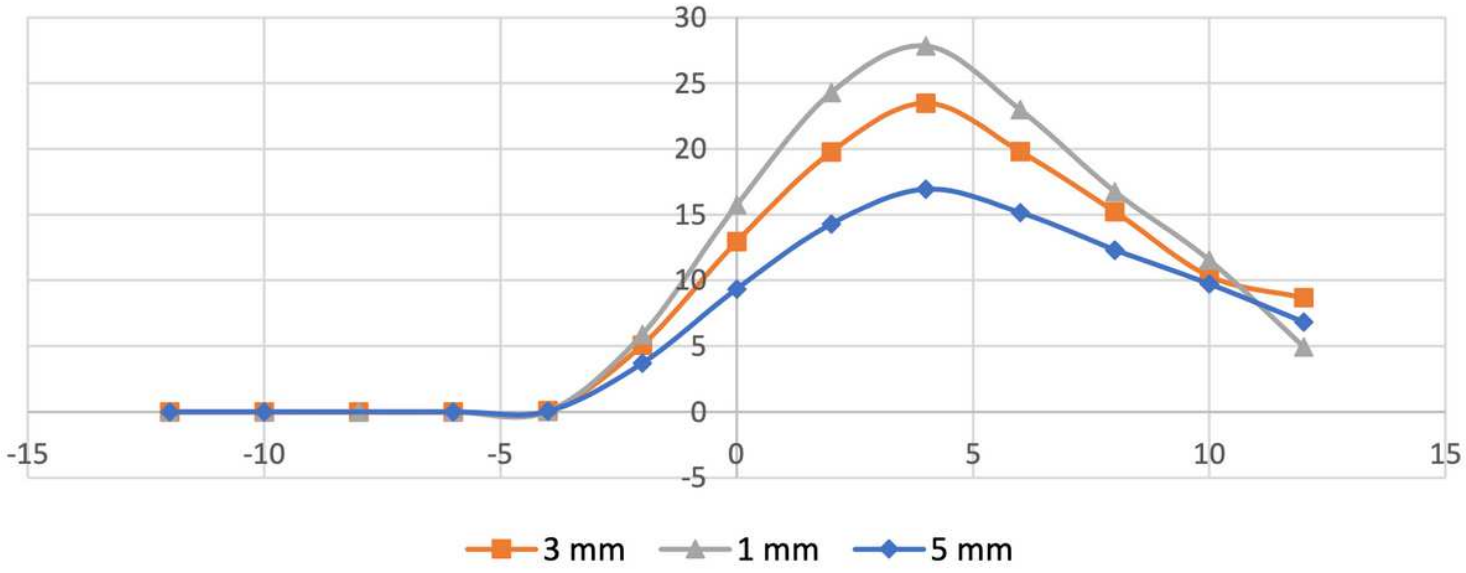

Figure 42

CL3/2/CD VS. angle of attack for the different panel thicknesses

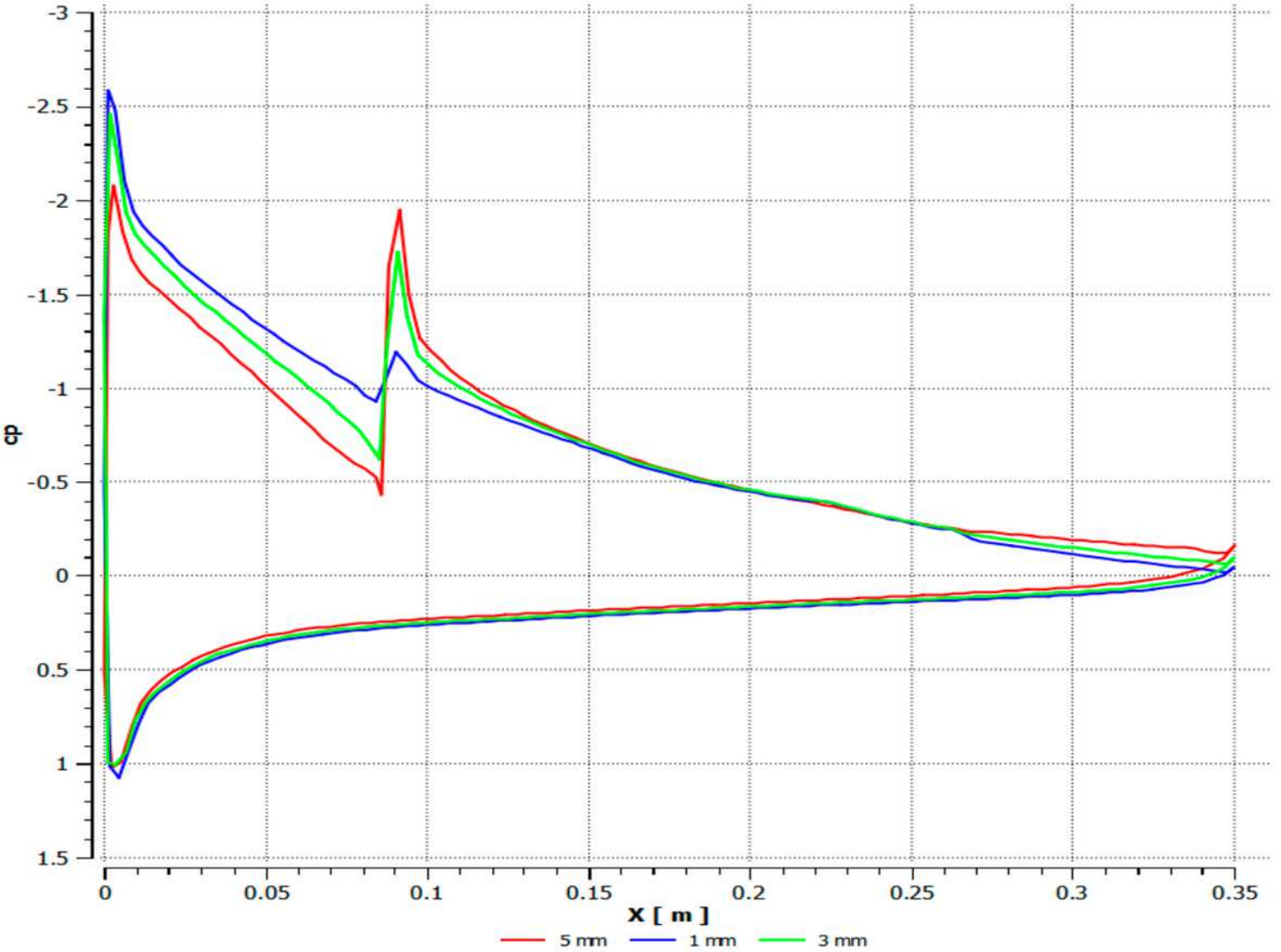

Figure 43

Pressure coefficient distribution over the configurations of different panel sessenhttht

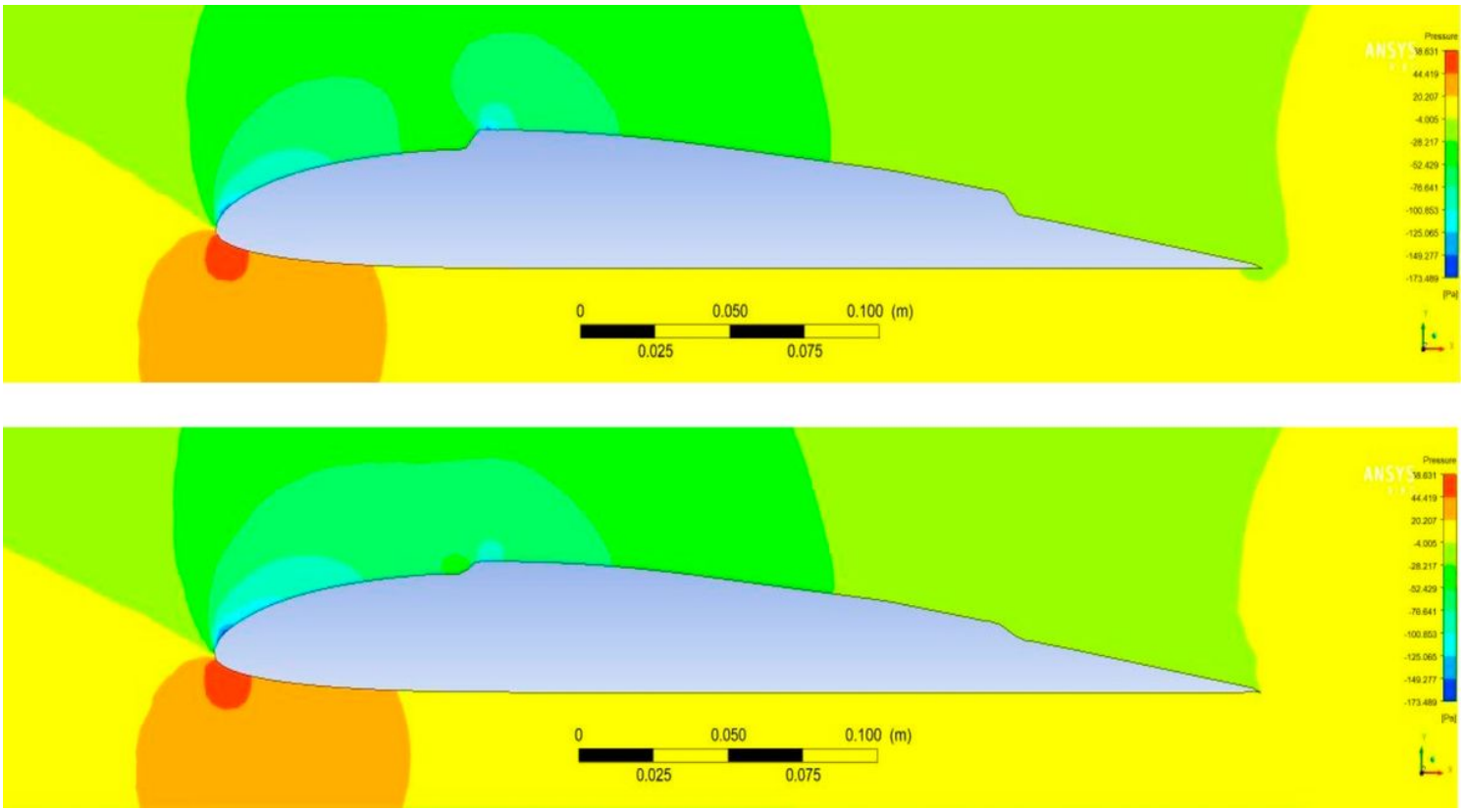

Figure 44

Pressure contour around airfoil AG34 at 6o angle of attack for the solar panel of thickness a) 3 mm, and b) 5 mm

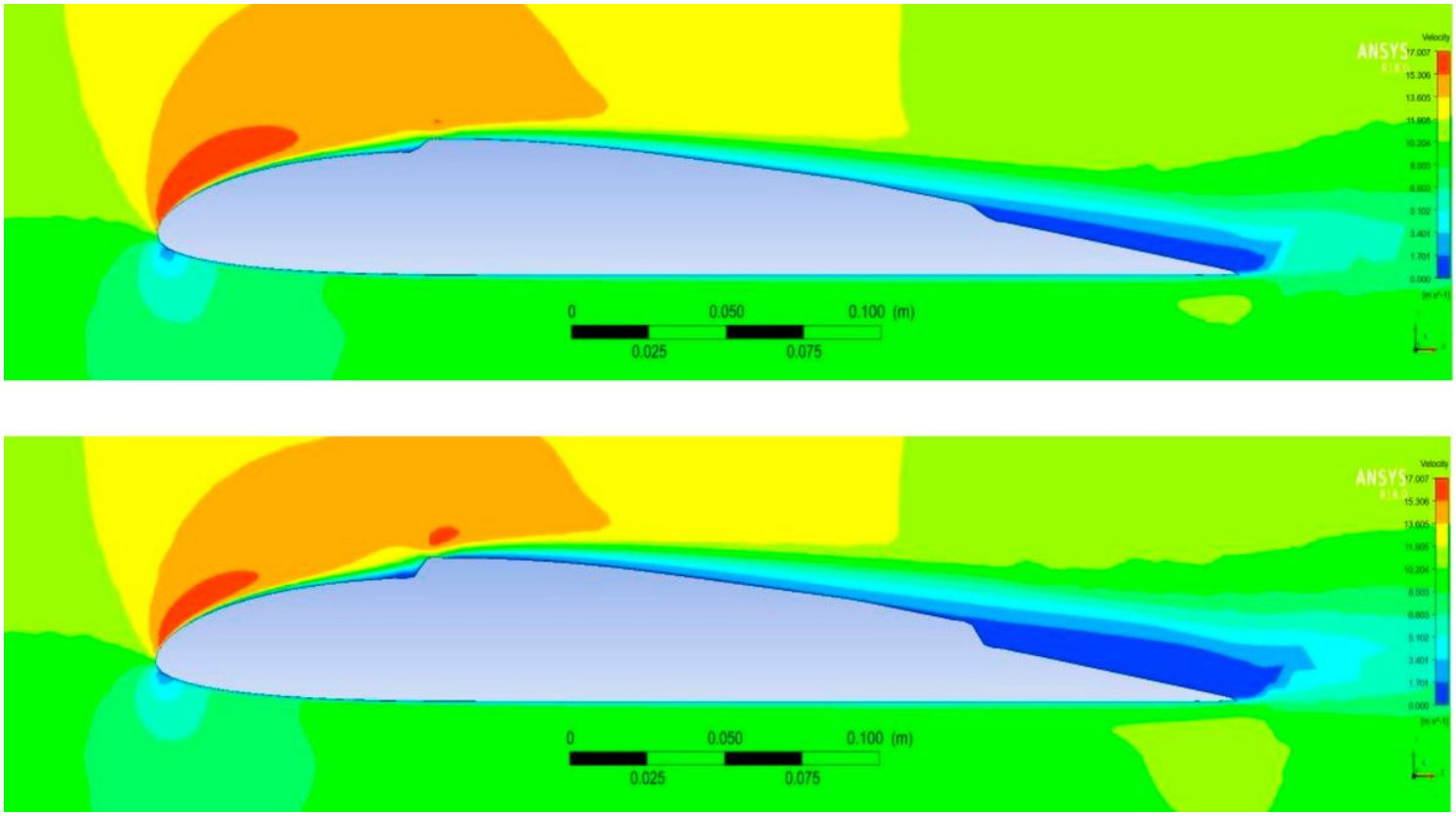

Figure 45

Velocity contour around airfoil AG34 at 6o angle of attack for the solar panel of thickness a) 3 mm, and b) 5 mm